

# **Charge Transport in Bulk Heterojunctions with Perylene Diimide based Acceptors**

Dissertation  
zur Erlangung des Grades

“Doktor der Naturwissenschaften“

im Promotionsfach Chemie  
am Fachbereich Chemie, Pharmazie und Geowissenschaften  
der Johannes Gutenberg-Universität  
in Mainz

**Selen Solak Sevinç**  
geb. in Kırklareli, Türkei

Max-Planck-Institut für Polymerforschung

Mainz, den 20.02.2016

Tag der mündlichen Prüfung: 08.02.2017



---

MAX-PLANCK-GESELLSCHAFT



JOHANNES GUTENBERG  
UNIVERSITÄT MAINZ



I hereby declare that I wrote this dissertation submitted without any unauthorized external assistance and used only sources acknowledged in the work. All textual passages which are appropriated verbatim or paraphrased from published and unpublished texts as well as all information obtained from oral sources are duly indicated and listed in accordance with bibliographical rules. In carrying out this research, I complied with the rules of standard scientific practice as formulated in the statutes of the Johannes Gutenberg-University Mainz to insure standard scientific practice.

Selen Solak Sevinç



## Summary

Organic solar cells have emerged as an alternative to first generation inorganic solar cells. The ability to print organic solar cells on large areas by roll-to-roll based production methods makes them very attractive for future technological applications. In bulk-heterojunction organic solar cells, consisting of a blend of a donor and acceptor, fullerene derivatives have been the work horse for acceptor materials; however their relatively high price and limited absorption stimulated the search for alternative n-type materials. In recent years new n-type materials have gained an increased attention in order to replace the well-known n-type fullerene derivatives in organic bulk heterojunction solar cells. Perylene diimide derivatives aroused as an attractive class of materials due to the possibility to tune their structural, optical, and electronic properties via their functional positions. In this way, materials with desired properties for opto-electronic applications can be developed, including a high absorption in the visible part of the spectrum. However, the performance of solar cells using perylene diimide derivatives remained mainly below those of the well-known fullerene derivatives.

In order to further improve the device performance of organic solar cells, understanding of their fundamental device physics and loss processes is required in order to develop new promising materials. An important loss process is the recombination of charge carriers. The nature of the recombination can be studied by measuring the dependence of the open-circuit voltage on light intensity. In this thesis the effect of non-ohmic contacts on the light intensity dependence of open circuit voltage of bulk heterojunction organic solar cells is studied. Furthermore, the charge transport in solar cells and single carrier devices based on perylene diimide acceptors is investigated. To this end, current-voltage characteristics of solar cells, electron-only and hole-only devices are performed and modeled with drift-diffusion simulations.

The effect of non-ohmic contacts on light intensity dependence of open circuit voltage are studied in conventional MEH-PPV:PCBM bulk heterojunction organic solar cells (Chapter 2). In these solar cells deliberately non-ohmic contacts are created either in the cathode or anode. It is known from literature that in the case of trap-free charge transport and ohmic contacts, a slope of  $kT/q$  is observed for the open-circuit voltage versus light-intensity dependence of organic solar cells. In our study, it is demonstrated that in the case of contact barriers a reduced light-intensity dependence is found when the open-circuit voltage surpasses the built-in voltage, leading to a slope of  $kT/2q$  for a device with one non-

ohmic contact and a slope of zero for a device with two non-ohmic contacts. For the case of one non-ohmic contact also an analytic expression was derived demonstrating a slope of  $kT/2q$ . We demonstrate that the reduced light-intensity dependence of the open-circuit voltage is not caused by entering a contact-recombination-limited regime, but by the absence of band bending in the vicinity of a non-ohmic contact.

The electron and hole transport of blends of regioregular poly(3-hexylthiophene) (rr-P3HT) donor and commercial planar perylene-3,4,9,10-perylene tetracarboxylic acid diimides (PDI-1) are investigated using electron-only and hole-only devices (Chapter 3). Trap-free space-charge-limited electron and hole currents are shown for electron and hole-only devices of as-cast P3HT:PDI-1 blends, respectively. The lower mobility of electrons and holes in the as-cast devices correlate with an increased energetic disorder in P3HT:PDI-1 blends as compared to the well-known P3HT:fullerene blends. Furthermore, it is shown that thermal annealing of P3HT:PDI-1 leads to injection-limited electron currents. Therefore, the effect of annealing on the electron mobility cannot be determined directly from the current-voltage characteristics. After studying the electron and hole transport solar cells of the same blend are studied (Chapter 4). Upon annealing of complete devices, the prominent loss in open-circuit voltage is accompanied by an increase in photocurrent. The decrease in open-circuit voltage is consistent with the formation of an electron injection barrier upon annealing in electron-only devices. The presence of an injection barrier is confirmed by the occurrence of a slope of  $kT/2q$  at high light intensities, which is a fingerprint of an injected-limited contact in organic solar cells. The mobility of electrons in the annealed case is estimated using drift-diffusion simulations of as-cast and annealed solar cells under light conditions. The simulations show that electron mobility in the order of  $10^{-9} \text{ m}^2/\text{Vs}$  is necessary to explain the increase in photocurrent upon annealing and the open-circuit voltage behavior

For comparison, *ortho*-substituted perylene diimide derivatives are studied in electron-only devices and solar cells (Chapter 5). As compared to the commercial planar PDI-1 derivative a slightly lower electron-mobility is observed together with a small increase of the energetic disorder. Furthermore, in the as-cast devices the solar cell performance is increased due to an increased photocurrent. The effect of annealing on electron transport and solar cell performance is also studied.

Lastly, the electron transport in the n-type Poly{[N,N0-bis(2-octyldodecyl)-naphthalene-1,4,5,8-bis(dicarboximide)-2,6-diy]-alt-5,50-(2,20-bithiophene)}[P(NDI2OD-T2)], known also as Activink N2200 polymers is investigated for various molecular



weights (Chapter 6). No systematic dependence of the electron transport on molecular weight is observed. Compared to the commercial N2200 all compounds exhibit a lower mobility and higher energetic disorder. A possible reason for the reduced electron transport can be the occurrence of electron traps remaining from the synthesis.



## Zusammenfassung

Organische Solarzellen haben sich zu einer Alternative zu Solarzellen der ersten Generation entwickelt. Sie sind besonders interessant für zukünftige Anwendungen, weil sie mit einem Rolle-zu-Rolle-Verfahren großflächig gedruckt werden können. In sogenannten bulk-heterojunction Solarzellen, die aus einer Mischung eines Donors und eines Akzeptor bestehen, werden üblicherweise Fullerene als Akzeptor-Material verwendet. Aufgrund des hohen Materialpreises und der geringen Lichtabsorption der Fullerene wurde in den letzten Jahren nach alternativen Akzeptor-Konzepten als Ersatz für die Fullerenderivate gesucht.

Dabei haben Perylenediimid-Derivate besonderes Interesse geweckt, da deren optische, strukturelle und elektronische Eigenschaften gezielt durch die funktionellen Gruppen eingestellt werden können. Dadurch lassen sich Materialien mit definierten Leistungs-vermögen, beispielsweise einer hohen Absorption im sichtbaren Spektrum erzielen. Die Kennwerte der Solarzellen waren allerdings stets schlechter als die Fulleren-basierten Referenzsolarzellen.

Für eine Optimierung der Solarzellen mit Perylenediimid-Derivaten als Akzeptor ist ein besseres Verständnis der Verlustprozesse und der Physik dieser Halbleiterbauelemente im Allgemeinen notwendig. Beispielsweise gibt die Abhängigkeit der Leerlaufspannung von der Lichtintensität wichtige Erkenntnisse über die Ladungsträgerrekombination, welche einen entscheidenden Verlustprozess darstellt. In dieser Arbeit wird unter anderem der Einfluss von Nicht-Ohmschen Kontakten auf die Relation zwischen Lichtintensität und Leerlaufspannung analysiert. Außerdem wird der Ladungstransport in Solarzellen und ladungsträgerspezifischen Dioden untersucht. Die gemessenen Strom-Spannungskennlinien werden mit Drift-Diffusions-Simulationen modelliert.

In Kapitel 2 wird zunächst die Abhängigkeit zwischen Lichtintensität und Leerlaufspannung für Solarzellen mit Fullerenen als Akzeptor untersucht. Dies dient als Referenz mit Nicht-Ohmschen Kontakten. Bei Ohmschen Kontakten, und wenn der Ladungstransport unabhängig von Fallenzuständen ist, dann ergibt sich gemäß Literatur für die Abhängigkeit zwischen Leerlaufspannung/Lichtintensität eine Gerade mit Steigung  $kT/q$ .

Wenn allerdings eine der beiden Kontakte eine signifikante Barriere aufweist, dann ergibt sich eine Steigung  $kT/2q$ . Ein analytischer Ausdruck für diesen Fall wurde erarbeitet,

der zeigt, dass die neue Abhängigkeit dadurch hervorgerufen wird, dass nahe am nicht-ohmschen Kontakt keine Bandverbiegung auftritt. Falls beide Kontakte nicht-ohmsch sind, dann verschwindet die Steigung ganz.

Der Ladungstransport in Blends bestehend aus regioregulärem Poly(3-hexylthiophene) (rr-P3HT) als Donor und kommerziell erhältlichem Perylene-3,4,9,10-perylentetra-carbonsäurediimid (PDI-1) als Akzeptor wurde in ladungsträgerspezifischen Dioden in Kapitel 3 untersucht.

Sowohl Elektronen als auch Löcher gehorchen physikalischen Space-charge-limited Transport-Modellen ohne Einfluss von Fallenzuständen. Die geringere Beweglichkeit von Elektronen und Löchern im Vergleich zu P3HT:Fulleren-basierten Dioden ist auf eine höhere energetische Unordnung zurückzuführen. Da thermische Nachbehandlung der P3HT-PDI-1 Diode zu Elektronentransport führt, der durch Injektion an der Elektrode begrenzt wird, kann der Einfluss der Wärmebehandlung auf den Elektronentransport nicht direkt aus den Strom-Spannungskennlinien abgeleitet werden.

Nachdem der selektiven Analyse von Elektronen- und Lochtransport wurde im nächsten Schritt die Solarzelle selbst untersucht (Kapitel 4). Wärmebehandlung der Solarzellen führte zu einem Anstieg des Photostroms bei einer gleichzeitigen Verringerung der Leerlaufspannung. Letztere ist im Einklang mit der bereits oben erwähnten Bildung der Injektionsbarriere am Kontakt. Die bei hohen Lichtintensitäten beobachtete Steigung von  $kT/q$  bestätigt diesen Befund, da sie charakteristisch für injektionslimitierten Transport in organischen Solarzellen steht.

Die Beweglichkeit von Elektronen vor und nach der Wärmebehandlung wurde mit einem Drift-Diffusion-Modell simuliert. Eine Elektronenbeweglichkeit in der Größenordnung von  $10^{-9} \text{ m}^2/\text{Vs}$  wird demnach benötigt, um den Anstieg des Photostroms und die Verringerung der Leerlaufspannung nach der Wärmebehandlung zu erklären.

In Kapitel 5 werden zum Vergleich *ortho*-substituierte Perylendiimide-Derivative elektronisch charakterisiert. Diese weisen eine leicht geringe Elektronenbeweglichkeit auf Grund einer leicht erhöhten energetischen Unordnung auf. Die Solarzellen zeigen höhere Effizienzen bedingt durch den höheren Photostrom. Auch für dieses Blend wurde der Einfluss der Wärmebehandlung untersucht.

Schließlich wurde in Kapitel 6 der Elektronentransport in dem Polymer Poly{[N,N0-bis(2-octylododecyl)-naphthalene-1,4,5,8-bis(dicarboximide)-2,6-diyl]-alt-5,50-(2,20-bithiophene)}[P(NDI2OD-T2)], besser bekannt als Activink N2200, für verschiedene

Molekulargewichte untersucht (Kapitel 6). Der Elektronentransport zeigt keine systematische Abhängigkeit vom Molekulargewicht. Verglichen mit dem kommerziellen N2200 zeigen alle Gemische geringere Mobilität und höhere energetisch Unordnung. Fallenzustände für die Elektronen resultierend aus der organischen Synthese könnten hierfür ursächlich sein.



## Contents

<b>1. Introduction</b>	<b>1</b>
1.1. Introduction.....	2
1.2. Conjugated polymers .....	3
1.3. Working principle of organic solar cells.....	4
1.4. Device performance of organic solar cells.....	6
1.4.1. Light intensity dependence of the open circuit voltage in organic solar cells .....	8
1.5. Device characteristics of single carrier devices .....	9
1.6. Current-voltage characteristics of organic solar cells .....	11
1.7. Charge carrier recombination in organic solar cells .....	14
1.8. Charge transport characteristics in organic semiconductors.....	16
1.9. Drift-diffusion modeling of organic semiconductors .....	19
1.10. Scope and outline of the thesis .....	19
1.11. References.....	21
<b>2. Effect of non-ohmic contacts on the light intensity dependence of the open-circuit voltage in organic solar cells</b>	<b>25</b>
2.1. Introduction.....	26
2.2. Ohmic and non-ohmic contacts in an organic diode and their effect on open circuit voltage.....	27
2.3. Effect of contact barriers on dependence of open circuit voltage on light intensity....	28
2.4. Role of contact- and bulk recombination on the open circuit voltage at high light intensities .....	29
2.5. Experimental verification of light-intensity dependence of open circuit voltage in organic solar cells .....	30
2.6. Conclusions.....	32
2.7. Experimental.....	33
2.8. References.....	35
<b>3. Charge transport in P3HT:perylene diimide blends</b>	<b>37</b>
3.1. Introduction.....	38

3.2.	Morphology of P3HT:PDI-1 blends .....	40
3.3.	Electron transport .....	42
3.4.	Hole transport .....	43
3.5.	The effect of annealing on electron and hole current .....	45
3.6.	Conclusions .....	46
3.7.	Experimental.....	47
3.8.	References .....	49
<b>4.</b>	<b>The effect of annealing on open circuit voltage of P3HT:PDI solar cells</b>	<b>51</b>
4.1.	Introduction .....	52
4.2.	Current-voltage characteristics of P3HT:PDI-1 solar cells .....	53
4.3.	Open circuit voltage-light intensity measurements in P3HT:PDI-1 solar cells.....	56
4.4.	Modelling of the photocurrent of P3HT:PDI-1 solar cells .....	58
4.5.	Modeling of open circuit voltage-light intensity measurements in P3HT:PDI-1 solar cells.....	61
4.6.	Analysis of P3HT:PDI-1 solar cells in 1:4 weight ratio .....	61
4.7.	Conclusions .....	70
4.8.	Experimental.....	71
4.9.	References .....	73
<b>5.</b>	<b>Charge transport in P3HT:perylene diimide derivatives</b>	<b>75</b>
5.1.	Introduction .....	76
5.2.	Electron and hole transport in PDI derivatives.....	77
5.3.	The effect of annealing on electron and hole current in PDI derivatives .....	79
5.4.	Solar Cells .....	80
5.5.	Conclusions .....	83
5.6.	Experimental.....	84
5.7.	References .....	86
<b>6.</b>	<b>Electron transport in P(NDI2OD-T2) polymer with varying molecular weights</b>	<b>87</b>
6.1.	Introduction .....	88
6.2.	Electron Transport in commercial N2200 from Polyera .....	89
6.3.	Electron Transport in N2200 with varying molecular weight .....	91
6.4.	Conclusions .....	94
6.5.	Experimental.....	94
6.6.	References .....	95



<b>List of Publications</b>	<b>97</b>
<b>Curriculum Vitae</b>	<b>99</b>
<b>Acknowledgments</b>	<b>101</b>



## **1. Introduction**

In this introduction chapter, the physics of organic electronic devices is discussed. The concept of single carrier devices (electron-only and hole-only devices) and solar cells are introduced, together with the overview of the fundamental concepts and theoretical basis for the charge transport, charge recombination and numerical device simulations. The fundamental differences between organic and inorganic solar cells are addressed. The scope and outline of the thesis is defined as a guide to the following chapters.

## **1.1. Introduction**

The lasting pollution of the environment in the last decades with fossil fuels as main energy sources causes increase in the earth's temperature and leads to a climate change [1]. In order to prevent a catastrophic end for our environment there is an urgent need to replace our fossil energy usage by renewable energy sources. Additionally, fossil fuels are finite [2], and together with the increasing need for energy, renewable energy sources such as solar and wind will play an important role in the future. Harvesting the energy from the sun is one of the most attractive renewable energy sources, because to cover the worldwide energy consumption of 500 ExaJoule/year only 0.01% of the energy of incoming sunlight on the earth surface needs to be harvested [3].

Solar cells that turn the light into electricity were invented at Bell Laboratories in 1954 [4]. The principle is based on the work done by Becquerel in 1839 and by Hertz in 1887 [5,6]. Since their invention solar cells have been further developed and the so-called first generation silicon based solar cells are being applied for roof-top applications, where they can provide 20 % efficiency with 5 to 20 years warranty.

Organic solar cells have emerged as an alternative to first generation inorganic solar cells. The electrical conductivity in organic materials was firstly discovery in anthracene [7]. In 1977 it was discovered that the conductivity in conjugated polymers can be strongly enhanced by doping, for which Shirakawa, MacDiarmid and Heeger were awarded the Nobel Prize in chemistry in 2000 [8]. These studies paved the way for the development of solar cells, light-emitting diodes and field effect transistors based on organic semiconductors. The research on organic solar cells was driven by their potential to lower the cost as compared to silicon based inorganic solar cells [9]. Moreover, conjugated polymers or organic small molecules can dissolve in common organic solvents, such that a thin layer of semiconducting material can be applied by means of printing technologies. The ability to print organic solar cells on large areas by roll-to-roll based production methods make them very attractive for future technological applications [10]. Furthermore, they have potential for wider applicability by means of their flexibility and (semi)transparency.

Currently, multi junction organic solar cells can provide 13.2 % power conversion efficiency [11]. Figure 1.1 shows the current status of solar technology based on various types of solar cells [12]. As can be seen from Figure 1.1, for organic solar cells improvement of the power conversion efficiency is required in order to compete with silicon or the recently introduced perovskite based solar cells. To understand their

limitations research on the fundamental device physics is needed, leading to the development of new organic semiconductors with improved opto-electronic properties.

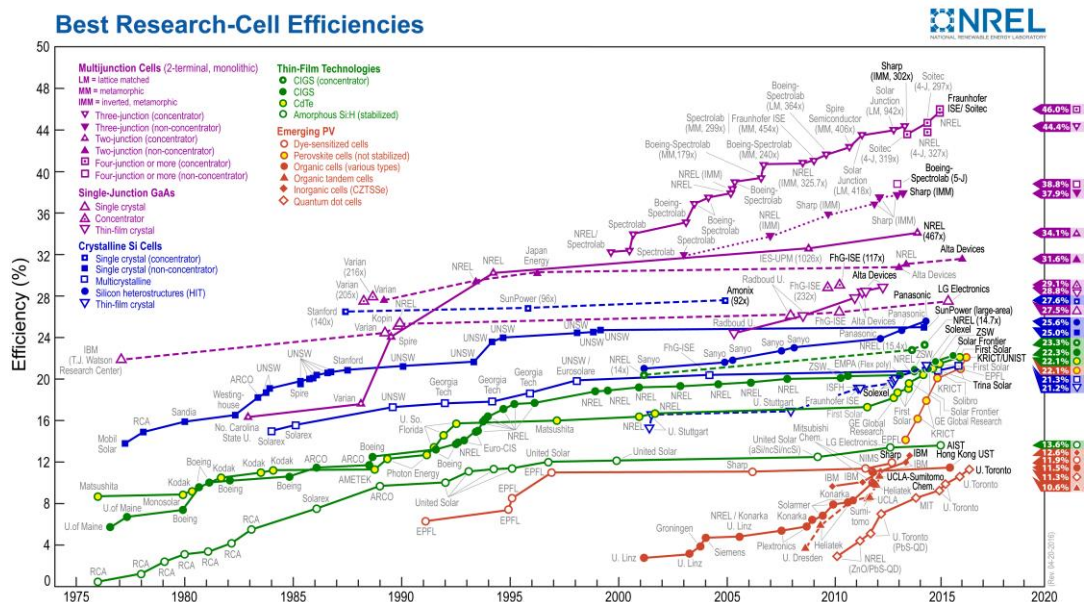


Figure 1.1. National Renewable Energy Laboratory (NREL) chart for best solar cell efficiency for various solar cell technologies [12].

## 1.2. Conjugated polymers

Conjugated polymers and small molecules are the building blocks of organic electronic devices, such as organic solar cells (OPVs), organic light emitting diodes (OLEDs) and organic field effect transistors (OFETs). Conjugation is shown in Figure 1.2 (a) for polyacetylene, which has alternating single and double bonds between its carbon atoms. Carbon (C) has a  $1s^2 2s^2 2p^2$  ground state electronic configuration with four covalent bonds. In the configuration of several carbon atoms, the orbitals can hybridize and form new hybrid orbitals. Thereby,  $\sigma$ -bonds are formed by overlapping the  $sp^2$ -orbitals of two carbon atoms and  $\pi$ -bonds are formed from overlapping  $p_z$ -orbitals that are perpendicular to the  $\sigma$ -bonds, as shown schematically in Figure 1.2 (b) for ethene [13]. The conjugated system is the alternating configuration of  $\sigma$ -bonds (single bonds) and  $\sigma$ -and  $\pi$ -bonds (double bonds).

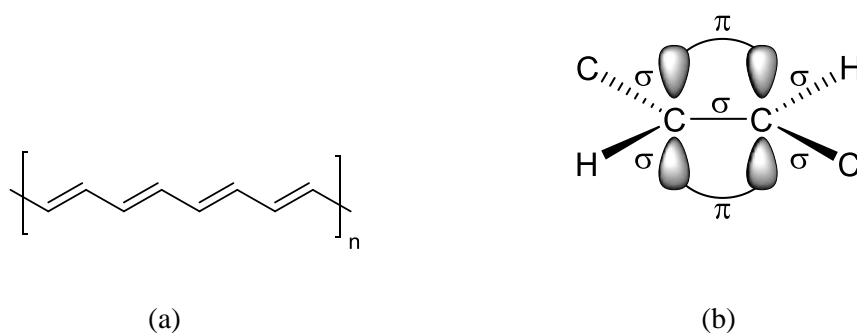


Figure 1.1 (a) Alternating single and double bonds in the simplest conjugated polymer polyacetylene and (b)  $\sigma$ -bonds from overlapping of two  $\text{sp}^2$ -orbitals and  $\pi$ -bonds from overlapping of two  $\text{p}_z$ -orbitals in ethane [13].

The electrical conductivity of conjugated polymers originates from their delocalized  $\pi$ -electrons; the electrons in the strongly localized  $\sigma$ -bonds do not contribute to the charge transport. Additionally,  $\text{p}_z$  orbitals occur in a bonding ( $\pi$ ) and antibonding ( $\pi^*$ ) configuration, the highest  $\pi$  orbital that is filled by electrons is called the highest occupied molecular orbital (HOMO) and lowest ( $\pi^*$ ) orbital that does not contain electrons is called the lowest unoccupied molecular orbital (LUMO), which are the equivalent of the valence and conduction bands in inorganic semiconductors, respectively [14]. These HOMO and LUMO are separated by an energetically forbidden area, stemming from a difference in the inter-atomic distance between single and double bonds, also called Peierls instability [15]. However, conjugated polymers are not perfect materials and the conjugation is interrupted by chain defects, kinks in the chains etc. [16,17]. As a result a polymer chain consists of conjugated segments with varying length. Due to quantum confinement every conjugated segment has slightly different HOMO and LUMO energies. This leads to a broadening of the HOMO- and LUMO levels, which is termed as energetic disorder. Due to the broken conjugation the charge transport happens by hopping between the conjugated segments [16]. Therefore, the band transport theory of inorganic solar cells cannot be applied to the organic semiconductors because of their spatial and energetic disorder [18].

### 1.3. Working principle of organic solar cells

Organic solar cells are devices which convert light into the electrical power. Starting from the absorption of light and ending by extraction of the free carriers in the external circuit,

several processes need to successfully happen. The main difference between organic- and inorganic solar cells is that the absorption of light does not directly create free carriers in organic materials due to the low dielectric constant of (2-4) [19], as compared to inorganic materials (13-16) [20]. Due to the low dielectric constant the photogenerated electron-hole pairs are strongly bound, which still need to be separated to obtain free carriers and the resulting photocurrent.

In the conventional design of organic solar cells, a thin layer of a donor/acceptor blend is sandwiched between the cathode and a transparent anode material. Ohmic contacts are created by matching the HOMO of the donor material and the LUMO of the acceptor material with the work functions of anode and cathode, respectively. In order to generate photocurrent, several processes need to happen sequentially inside the device. These processes are schematically shown in Figure 1.3, where solid lines correspond to LUMO and HOMO of a donor material and of an acceptor material. Upon solar radiation a photon is absorbed either by acceptor or donor or both (in Figure 1.3 the case for the donor is shown) and an exciton is created (Frenkel exciton) [13] with a typical binding energy of 0.5 eV [13] (Figure 1.3 no.1). Then, the exciton diffuses until it reaches the donor-acceptor interface. Here the exciton dissociates by means of an electron transfer from the donor to the acceptor and a bound electron hole pair is formed at the interface, with the hole in the donor phase and the electron in the acceptor phase. The energy offset between the LUMO levels of the donor and acceptor creates the driving force for exciton dissociation. Since the diffusion length in organic semiconductors is typically limited to the range of 5-10 nm the typical domain size of the donor should not exceed 20-30 nm [21]. In case of larger domains most of the excitons will not reach the donor-acceptor interface and therefore will not dissociate but recombine, leading to low solar cell efficiencies (Figure 1.3 no.2). As a result, the morphology of the blends plays an important role. In the conventional design of organic solar cells, donor materials are mostly a conjugated polymer and fullerene derivatives are used as acceptor. The spatially separated but still bound electron-hole pair this is formed after exciton dissociation still has to be separated in order to create free charge carriers. The separation of the bound electron-hole pair is expected to depend on the electric field and temperature [22]. In organic semiconductors free charge carriers are named as polarons, since the presence of electrons or holes leads to a local distortion of the atomic configuration around them [23]. As a next step the free charges have to be transported to the respective electrodes (Figure 1.2 no.4) where they are extracted into the electrical circuit (Figure 1.3 no.5). For this to happen the BHJ morphology has to be formed

in such a way that percolative pathways for both donor- and acceptor phase exist towards the electrodes.

Because of the existence of loss mechanisms in organic solar cells, not every absorbed photon can contribute to the photocurrent generation. As mentioned above if an exciton cannot reach to the donor-acceptor interface it will decay to the ground state either by photon emission (radiative decay) or it can decay non-radiatively [24]. The bound electron-hole pairs at the D-A interface can also recombine before the electron and hole are separated (geminate recombination). Finally, the free charge carriers that are transported to the electrodes can recombine with a carrier of opposite sign via bimolecular-non-geminate recombination [25-28]. Therefore, understanding the transport and recombination characteristics of the individual charge carriers is of great importance to investigate and improve solar cell performance.

#### **1.4. Device performance of organic solar cells**

After absorption of photons in a solar cell charge carriers are generated in the active layer and a photocurrent ( $J_{ph}$ ) is produced [29]. With regard to the current-voltage characteristics solar cells work in the so-called fourth quadrant, and the important parameters in order to define solar cell performance are shown in Figure 1.4. When the net current is zero, i.e. charge generation is compensated by recombination, the open circuit voltage ( $V_{oc}$ ) condition is reached. When the applied voltage is zero the short circuit current ( $J_{sc}$ ) condition is reached. The band diagrams at these conditions are simply illustrated in Figure 1.5. At applied voltages higher than  $V_{oc}$ , the charge extraction process is reversed and the carriers are injected. The difference between the work functions of the electrodes in the solar cell is the built in voltage ( $V_{bi}$ ) and it regulates the rectifying  $J$ - $V$  behavior of organic solar cells.



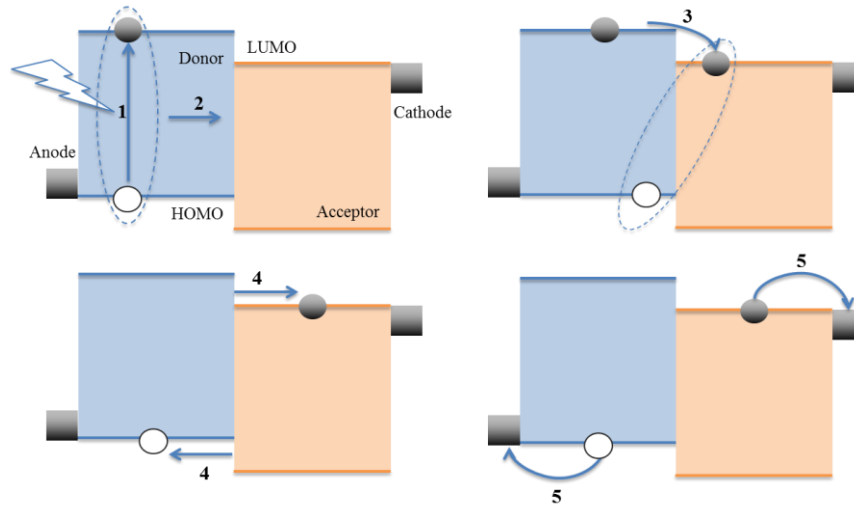


Figure 1.3. The sequential steps that have to be followed in organic solar cells in order to extract charges. When a photon is absorbed, an exciton is formed (no. 1), that diffuses towards the donor-acceptor interface (no. 2). Here, the electron is transferred from the donor to the acceptor material (no. 3), and a bound electron-hole pair is formed. After separation of the bound  $e-h$  pair the free charges are transported to the respective electrodes (no. 4) where they are extracted (no. 5).

The solar cell performance is evaluated by the maximum electrical power ( $M_{MPP}$ ) that a solar cell can give under illumination. Maximum power correlates to the point where the product of current ( $J_{MPP}$ ) and voltage ( $V_{MPP}$ ) is at the maximum. The device efficiency ( $\eta$ ) is then defined by dividing the generated electrical power by the illumination intensity ( $I_{light}$ ). In order to equally compare all devices, standard test conditions (STC) have been defined. Here, the light intensity is equal to 1 Sun ( $1000 \text{ W/m}^2$ ), the solar cell temperature is  $25^\circ\text{C}$  and AM. (air mass) 1.5 is considered for the spectral distribution of the light. As shown in Figure 1.4, the fill factor ( $FF$ ) is another important parameter as it defines the squareness of the current-voltage characteristics of the solar cell, being described by the ratio of  $V_{MPP} \times J_{MPP}$  and  $V_{oc} \times J_{sc}$ . The power conversion efficiency ( $\eta$ ) of a solar cell is then defined by the following relation,

$$\eta = \frac{V_{MPP} J_{MPP}}{I_{light}} = \frac{V_{oc} J_{sc} FF}{I_{light}} \quad 1.1$$

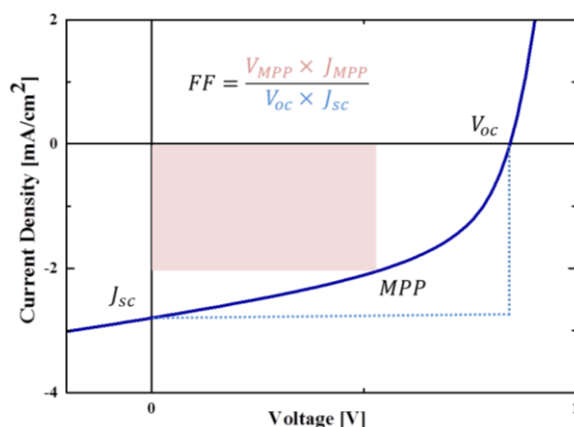


Figure 1.4. Current-voltage characteristics and important parameters of a solar cell under illumination.  $V_{oc}$ ,  $J_{sc}$  and maximum-power point is shown together with the fill factor (FF).

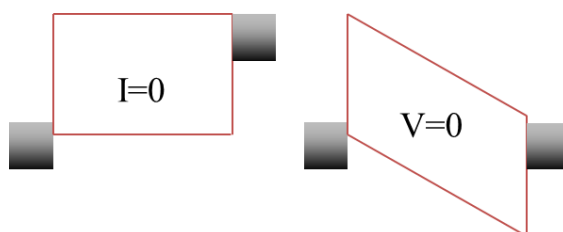


Figure 1.5. Band diagram of a solar cell under open-circuit ( $I=0$ ) and short-circuit ( $V=0$ ) conditions.

### 1.4.1. Light intensity dependence of the open circuit voltage in organic solar cells

In the conventional p-n junction model for ideal solar cells, as used for silicon based cells, it is assumed that the photogenerated current is independent of the applied voltage. For such an ideal solar cell the open-circuit voltage  $V_{oc}$  is expected to depend on light-intensity according to [30],

$$V_{oc} = n kT/q (J_{sc}/J_s + 1) \quad 1.2$$

where  $J_s$  is the saturation current density. However, for organic solar cells the photocurrent increases for higher voltages due to an increased dissociation of the bound electron-hole pairs [30]. For this case, Koster et al. derived an alternative expression for organic solar cells based on the metal-insulator-metal system with ohmic contacts and constant quasi Fermi levels. According to this model,  $V_{oc}$  is defined as [30],

$$V_{oc} = \frac{E_g^{DA}}{q} - \frac{kT}{q} \ln \left( \frac{(1-P)\gamma N_c^2}{PG} \right) \quad 1.3$$

with  $E_g = E_{HOMO} - E_{LUMO}$ ,  $P$  is the dissociation probability of a bound electron– hole pairs into free charge carriers and  $G$  is the generation rate and defined as  $G = \gamma np (1 - P)/P$ , where  $\gamma$  is the Langevin recombination constant,  $n$  and  $p$  are the electron and hole density, respectively. Since the generation rate ( $G$ ) is proportional to the light intensity,  $V_{oc}$  depends on the natural logarithm of the light intensity with a slope ( $S$ ) of  $kT/q$ . The  $kT/q$  dependence is different from the  $p$ - $n$  junction model where the slope is given by  $nkT/q$  [30]. It should be noted that in the derivation of Eq. 1.3 only bimolecular recombination is included as a loss process. The observed dependency of  $V_{oc}$ , where by definition there is no current extraction and all generated charge carriers recombine, on light intensity with  $S=kT/q$  for organic solar cells therefore implies that the dominant recombination process is of bimolecular nature.

In the literature it has also been shown that a deviation from the slope of, i.e.  $kT/q$  higher slopes than  $kT/q$ , can occur due to trap-assisted recombination [31]. For the situation where trap-assisted recombination is dominant, as is the case in diodes based on poly[2-methoxy-5-(2-ethylhexyloxy)-1,4-phenylenevinylene] (MEH-PPV) it has been shown that the slope of  $V_{oc}$ -light intensity approaches  $2kT/q$  [31,32].

## 1.5. Device characteristics of single carrier devices

In order to characterize the charge transport characteristics in bulk heterojunction solar cells, the hole transport in the donor phase of the blend and the electron transport in the acceptor phase have to be determined. This can be achieved by using selective contacts that only inject holes or electrons, the so-called single carrier devices. Therefore either electron-only (Figure 1.6 (a)) or hole-only (Figure 1.6 (b)) devices are made with Ohmic contacts for injection while preventing injection of the carrier of opposite sign with appropriate blocking contacts, respectively.

In single carrier devices of undoped organic materials the injection of charges leads to the build-up of space-charge. For applied voltages lower than the built-in voltage  $V_{bi}$ , which occurs when electrodes with different work functions are used, the electric field in the device is opposite to the current, and the current is dominated by diffusion [33]. For voltages larger than  $V_{bi}$  the current is dominated by drift of charge carriers in the electric field. In that case, the current is equal to the space-charge limited current (SCLC), which is

the maximum current that is electrostatically allowed and is described by the Mott-Gurney Law [34],

$$J = \frac{9}{8} \epsilon \mu \frac{(V - V_{bi})^2}{L^3} \quad 1.4$$

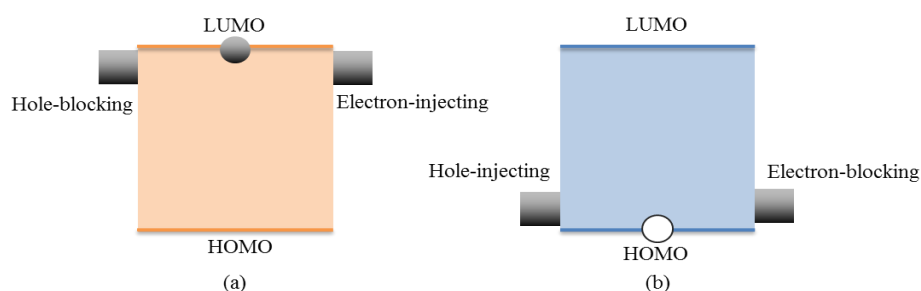


Figure 1.6. (a) electron-only device and (b) hole-only device with selective electrodes. Injecting- and blocking contacts are indicated.

$\mu$  is the mobility and  $\epsilon$  is the dielectric constant of the material.  $V$  is the applied voltage and  $L$  is the thickness of the active layer. The derivation of this equation includes the assumptions that the device is trap free, that the electric field at the is zero and that diffusion is negligible [34,35]. As can be seen from the equation the SCLC scales with the square of the applied voltage and with the third power of device thickness. From Eq. 1.4 the mobility of the corresponding charge carrier can be directly extracted from the  $J$ - $V$  characteristics when the active layer thickness is known. In the case of injection-limited contacts, the SCLC cannot be reached and devices have lower current than SCLC. In that case an injection barrier is formed between the semiconductor and electron or hole injecting contact. This injection barrier limits the amount of carriers in the sample such that space-charge effects become negligible and the current scales with the applied electric field ( $V/L$ ) [36]. It has been shown in the literature that for barriers smaller than 0.3 eV the contacts can still supply the SCLC current, for higher barriers device current becomes injection limited [37-39].

In order to fully explain the device characteristics, also at low voltages below  $V_{bi}$ , both diffusion and drift of the charge carriers need to be taken into account. As organic materials are undoped semiconductors, de Bruyn et al. developed an analytical model for the diffusion current, based on the Schottky diffusion theory [40,41]. They assumed a metal-insulator-metal (MIM) device with asymmetric contacts. It was demonstrated that the

analytical model describes the total current of a device for the whole voltage range by summing the contribution of diffusion current and space charge limited drift current [40]. The model also includes band bending at the Ohmic contact, which originates from the diffusion of charge carriers from the metal electrode into the semiconductor at zero bias, thereby creating an accumulation region at this contact. It is defined earlier that diffused charge carriers from an ohmic contact into the semiconductor create an accumulation region [42] and the diffusion of charge carriers cause band bending at this contact [40]. Using the model the transition from diffusion to drift current at  $V_{bi}$  enables then a direct determination of  $V_{bi}$  from the  $J$ - $V$  characteristics. Therefore,  $V_{bi}$  can be directly determined from the equation [40]. In the case of injection limited contacts, the band bending is absent due to the decreased amount of injected charges [40].

## 1.6. Current-voltage characteristics of organic solar cells

As described in Section 1.3 in organic solar cells, exciton dissociation at the D-A interface does not directly create free carriers, but instead bound electron-hole ( $e$ - $h$ ) pairs are formed. The bound electron-hole ( $e$ - $h$ ) pair still needs to be separated into free charge carriers in order to be collected and extracted at the respective electrodes. The total amount of free charge carriers, which contribute to the photocurrent, then depends on the competition between dissociation of bound  $e$ - $h$  pairs and recombination of free charge carriers.

Goodman and Rose studied the generation of current in a photoconductor with non-injecting contacts [43]. They demonstrated that the photocurrent has three main regimes, depending on the applied voltage. In their model the diffusion of charge carriers is neglected and the drift length of the charge carriers is defined as  $W_{e(h)} = \mu_{e(h)}\tau_{e(h)}$ , where  $\mu_{e(h)}$  is the electron (hole) mobility and  $\tau_{e(h)}$  is the life time of the electrons (holes), respectively [43]. At low voltages the drift length of both electrons and holes is smaller than the sample thickness, leading to a linear relation of the photocurrent with the applied voltage. It should be noted that alternatively a linear behavior can also originate from the competition between drift and diffusion at low voltages [44]. At intermediate voltages, in the case of unbalanced transport meaning that one carrier has a higher mobility than the carrier of opposite sign, the drift length of the fastest carrier is larger than the sample thickness, whereas the drift length of the slow carrier is still smaller than the sample thickness. This will lead to an accumulation of the slowest carrier in the device. In that case a  $V^{1/2}$  voltage dependence of the photocurrent is derived, given by [45],

$$J_{ph} = qG(\mu_{e(h)}\tau_{e(h)})^{1/2}V^{1/2} \quad 1.5$$

This photocurrent is also termed  $\mu\tau$ - or recombination-limited photocurrent. At high light intensities, when the transport is strongly unbalanced, the amount of slow carriers in the photoconductor can become so large that space-charge effects become important. For this specific case the maximum electrostatically allowed photocurrent or space-charge limited photocurrent is defined as [45],

$$J_{ph} = q \left( \frac{9\varepsilon_0\varepsilon_r\mu_{e(h)}}{8q} \right)^{1/4} G^{3/4}V^{1/2} \quad 1.6$$

where  $\varepsilon_0\varepsilon_r$  is the dielectric permittivity. The SCL photocurrent also has a  $V^{1/2}$  dependence on voltage but can be discriminated from the recombination-limited photocurrent (Eq. 1.4) by its dependence on  $G$ , which is proportional to the incident light intensity. Space charge limited photocurrents scale with  $G^{3/4}$ , whereas a recombination-limited current scales with  $G$  [45]. At high voltages, when the drift lengths of both slow and fast carriers are larger than the sample thickness, the saturated photocurrent given by  $J = eGL$  is observed. In that case there is no recombination and the photocurrent is equal to the amount of absorbed photons per unit of time, and is therefore independent of the applied voltage. However, for organic solar cells this saturated photocurrent is not really observed. It has been proposed [46] that with increased voltage and electric field the dissociation of the bound  $e-h$  pairs becomes more efficient. In that case the free carrier generation rate  $G$  is dependent on the electric field. The generation rate ( $G$ ) of free carriers is then defined by the probability ( $P$ ) of charge separation of all photogenerated bound  $e-h$  pairs  $G_{max}$  [28], given by

$$G(T, E) = G_{max} P(T, E) \quad 1.7$$

Onsager firstly described the dissociation of geminate bound pairs in the 1930s [47]. Later on, Braun refined the story of Onsager by adding that the bound ( $e-h$ ) pairs have a finite lifetime [48]. Braun proposed that the probability ( $P(T, E)$ ) of charge dissociation depends on the decay and dissociation rate ( $k_D$ ) into free carriers according to,

$$P(T, E) = k_D(T, E) / [k_D(T, E) + k_F(T)] \quad 1.8$$

where the dissociation rate is defined as;

$$k_D = k_R \frac{3}{4\pi a^3} e^{-E_B/kT} \left[ 1 + b + \frac{b^2}{3} + \frac{b^3}{18} + \frac{b^4}{180} \right] \quad 1.9$$

$k_R$  is the bimolecular recombination rate, representing the rate of separated free carriers that again form a bound pair, and it is defined by Langevin recombination. Furthermore,  $a$  is the initial separation distance of a bound ( $e-h$ ) pair. As can be seen from Eq. 1.8 a larger distance between the carriers of the bound pair gives rise to an enhanced dissociation.  $E_B$  is the binding energy of ( $e-h$ ) pair and  $b = q^3 E / 8\pi\epsilon_0\epsilon_r k^2 T^2$ , the effective field parameter. The illustration of dissociation, decay and recombination is schematically shown in Figure 1.7.

In 2005, Koster et al. developed a numerical device model for the current-voltage characteristics of bulk heterojunction solar cells with ohmic contacts [44]. The model solves the steady-state continuity equations for electrons and holes and takes into account the drift and diffusion of the carriers, as well as recombination and space charge effects [44]. In the model  $a$  and  $k_F$  are fitting parameters to the experimental data. The details of the numerical drift-diffusion simulation will be given in the device modeling section.

Last but not least, the morphology in the blend systems has a huge effect on the separation of charges. The effect of morphology, which is a random configuration, is not explicitly taken into account in the Onsager-Braun model. The 1D drift diffusion model assumes that the electric field is perpendicular to the donor-acceptor interface, which is not necessarily correct.

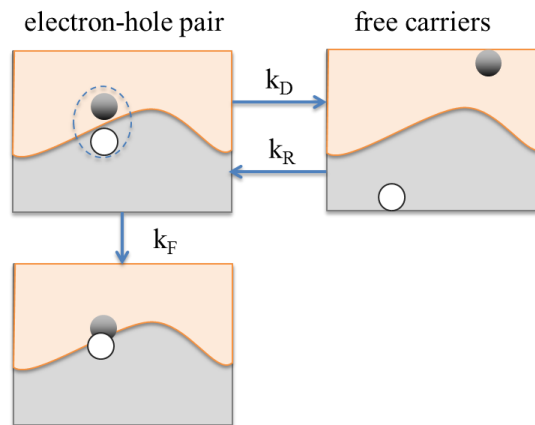


Figure 1.7. Donor and acceptor interface in an organic solar cell.  $k_D$  is the dissociation rate of the bound electron-hole pair at the D-A interface,  $k_R$  is the recombination rate of free carriers and  $k_F$  is the decay rate of the bound electron-hole pair.

### 1.7. Charge carrier recombination in organic solar cells

In order to generate a photocurrent in a solar cell, charge carriers need to be extracted at their respective electrodes. However, electrons and holes can recombine in the organic layer before their extraction at the contacts. Recombined carriers cannot contribute anymore to the photocurrent and therefore bimolecular recombination is a loss process in organic solar cells [28].

Bimolecular recombination in organic semiconductors is of the Langevin type; i.e., the rate-limiting step is the diffusion of electrons and holes toward each other in their mutual Coulomb field. Such a behavior is characteristic of materials, in which the mean free path of the charge carriers is smaller than the critical Coulombic capture distance. Another type of recombination that limits device performance is trap-assisted recombination, where a charge carrier that is trapped in a state in the forbidden gap recombines with a mobile charge carrier of the opposite sign. In many conjugated polymers, it is shown that the electron transport is limited by traps, while the hole transport is characterized by the trap-free space charge limited behavior [30, 49, 50]. Such a trap-limited electron current causes severe decrease in the device performance. The microscopic origin of the electron traps is still not clear, suggestion made in literature range from chemical defects, morphological defects, water-oxygen complexes etc. [51]. It was revealed by Nicolai et al. that for a number of organic semiconductors the electron traps are located at a certain energy level, typically  $\sim -3.6$  eV below the vacuum level, with a trap density of  $3 \times 10^{23} 1/m^3$  and with a trap distribution width of  $\sim 0.1$  eV [52]. As a result, for acceptor materials with the LUMO below  $\sim -3.6$  eV the electron trap is outside the band gap and the transport is trap-free.

In an organic solar cell, the bimolecular recombination is proportional to the product of free electron- and hole concentration given by [53];

$$R_B = k_R(np - n_i^2) \quad 1.10$$

where  $k_R$  is the coefficient for bimolecular recombination,  $n$  and  $p$  are the electron and hole concentrations, respectively and  $n_i^2$  is the intrinsic carrier concentration of electrons and holes and defined as  $n_i^2 = N_{CV} \exp[-E_{gap}/kT]$  [39]. As mentioned above in organic semiconductors, the bimolecular recombination is of the Langevin type [54], and the recombination coefficient is given by,



$$k_L = \frac{q(\mu_e + \mu_h)}{\varepsilon_0 \varepsilon_R} \quad 1.11$$

where  $q$  is the elementary charge,  $\varepsilon = \varepsilon_0 \varepsilon_R$  is the permittivity of the material and  $\mu_{e(h)}$  is the electron (hole) mobility. The recombination coefficient is thus defined by the sum of the carrier mobilities divided by the permittivity of material.

It is shown in the literature that for some organic solar cells a deviation from Langevin theory is present, meaning that the bimolecular recombination coefficient is lower than the Langevin value [55]. It was suggested by Koster et al. that in polymer/fullerene blends the recombination rate might be defined by the slowest carrier. Different than in a pristine semiconductor, in a blend system the recombination happens only at the interface, therefore the fastest carrier needs to wait for the slower carrier to reach the interface [55]. Numerical simulations assuming that the slowest carrier is dominant in the recombination strength showed a good agreement with experiment. Later on, it was proposed by Juška et al. that in systems as P3HT:PCBM where crystalline lamella are formed the Langevin recombination might be strongly reduced due to the 2-D character of such a structure [56].

For the case of trap-assisted recombination [57], specifically where a trapped electron that is immobile catches a free hole to recombine, the recombination rate is defined by the Shockley-Read-Hall (SRH) equation [58];

$$R_{SRH} = \frac{C_n C_p N_t}{[C_n(n+n_i) + C_p(p+p_i)]} \quad 1.12$$

$R_{SRH}$  defines the rate of trap-assisted recombination,  $C_n$  is the capture coefficients for electrons that can be captured by a neutral site and  $C_p$  is the hole capture coefficient for a trapped electron that can be captured by a hole. It has been demonstrated that the capture coefficient is given by  $C_{n(p)} = \frac{q}{\varepsilon} \mu_{n(p)}$  [57]. Furthermore,  $N_t$  equals the density of traps, and  $n$  and  $p$  are the density of free electrons and holes, respectively. In the absence of traps in single carrier organic devices the drift current is given by the space charge limited current. In the presence of traps the current is strongly reduced, and shows a stronger dependence on thickness and voltage [50]. In disordered semiconductors the trap states in the band gap are typically distributed in energy. The energy distribution of the trap states is often described as an exponential or Gaussian distribution [59]. Electron traps lie energetically below the LUMO energy of the material, and they are divided into shallow and deep traps,

depending whether the Fermi level lies below or above the center of trap distribution, respectively [59].

### 1.8. Charge transport characteristics in organic semiconductors

In inorganic semiconductors, the charge carriers in the valence and conduction bands are delocalized by means of the strong covalent coupling between atoms within the ordered lattice. Therefore, the charge carriers can move fast and typically at high temperatures transport is only interfered with lattice vibrations [23]. The main difference between charge transport in organic materials and inorganic systems is that in organic semiconductors the coupling between the molecules is of the weaker Van der Waals type. This weaker coupling is easily broken by spatial and energetic disorder, leading to the existence of localized states. For conjugated polymers it is expected that the charge transport between polymer chains is slow, (inter-chain transport), whereas the transport over a chain should be relatively fast (intra-chain transport). However, also the intra-chain transport can be hindered by imperfections in the chains like kinks, defects etc. [16]. The reason for the easily disturbed inter-chain transport is the weak Van der Waals forces between different chains; therefore the electronic coupling between adjacent chains is destroyed by an even small amount of disorder. Due to the existence of localized states the transport in organic materials occurs via hopping between these states, i.e. between the two adjacent filled  $\pi$ -orbitals or two adjacent empty  $\pi^*$ -orbitals by phonon assisted tunneling [23]. The hopping nature of the charge transport in organic semiconductors is the reason for the low charge carrier mobilities that are often observed [60].

A model for hopping transport in disordered organic semiconductor has been developed by Bässler et al [60]. In this model the energetic distribution of the transport sites, the density of states (DOS), is described by a Gaussian distribution according to,

$$\rho(E) = \frac{1}{\sqrt{2\pi\sigma^2}} \exp\left[-\frac{(\varepsilon-\varepsilon_c)^2}{2\sigma^2}\right] \quad 1.13$$

with  $\varepsilon_c$  the center of the DOS and  $\sigma$  the energy width of the Gaussian distribution. The Gaussian shape of the DOS is rationalized by the polarization energy difference around molecules. Furthermore, for polymers the conjugated chain segments might not all have the same size, leading to a spread in their energy levels due to the quantum confinement effect [61]. After injection, charge carriers will typically relax into the tail states of the Gaussian distribution. In order to move, carriers hop to available sites by emission or absorption of

phonon. The rate for such a hopping process is described by Miller and Abrahams [62] according to,

$$v_{ij} = v_0 \exp\left(-2\gamma a \frac{\Delta R_{ij}}{a}\right) \exp\left(-\frac{\varepsilon_j - \varepsilon_i}{k_B T}\right) \begin{cases} ; \varepsilon_j > \varepsilon_i \\ 1 & ; \varepsilon_j < \varepsilon_i \end{cases} \quad 1.14$$

The first exponential term includes the hopping distance  $\Delta R_{ij}$  and wave-function decay parameter  $\gamma$  that describes the wave-function overlap and tunneling probability, and  $a$  is the inter-site distance. The second term contains  $\varepsilon_j - \varepsilon_i$ , which is the energy difference between the initial and the final state. The hopping rate exponentially depends on this energy difference and temperature, as is typical for a Boltzmann factor. In case that the energy of the final state  $j$  is higher than the energy of the initial state  $i$ , the hopping transport is thermally assisted. In the reverse case, i.e. lower energy of the final states the exponential term goes to unity [62].

The mobility of the charge carriers, which is a measure of how fast carriers move in the semiconductor under an applied field, is of great importance for the device performance. In organic materials, charge carriers relax into the tail states of the Gaussian DOS and need be thermally activated towards sites higher in energy in order to contribute to the charge transport. Therefore, the mobility is temperature dependent and increases with increasing temperature [63]. The mobility of charge carriers is also enhanced by the electric field, which mainly decreases the energetic barrier for carrier jumps in the direction of the electric field [60]. In strongly disordered materials the charge carriers occupy states deep in the tail of the Gaussian distribution, and as a result the activation energy for charge transport is increased. Bässler et al. developed a model for hopping conduction in disordered materials; this is the so called Gaussian Disorder Model (GDM) predicts the temperature- and field dependence of the carrier mobility in disordered semiconductors. In the GDM model, the hopping rate among the sites that are energetically distributed in a Gaussian DOS is assumed to be of the Miller-Abrahams type. From Monte Carlo simulations Bässler obtained the field- $(E)$  and temperature  $(T)$  dependence of mobility in disordered materials as [60],

$$\mu(\sigma, \Sigma, T, E) = \mu_0 \exp\left[-\left(\frac{2\sigma}{3kT}\right)^2\right] \exp\left[C \left\{\left(\frac{\sigma}{kT}\right)^2 - \Sigma^2\right\} \sqrt{E}\right] \quad 1.15$$

with  $\sigma$  the width of the Gaussian DOS also termed the (energetic) diagonal disorder parameter, and  $\Sigma$  is the off-diagonal disorder parameter, representing spatial disorder.

Furthermore, the prefactor  $\mu_0$  represents the zero field mobility and  $C = 2.9 \times 10^{-4}(cm/V)^{1/2}$ , an empirical constant that depends on the hopping distance and governs the field- and temperature dependence of the mobility. The GDM predicts that the mobility depends on temperature as  $\ln(\mu) \propto 1/T^2$  and on the electric field as  $\exp(\sqrt{E})$ . A similar relation of the mobility on electric field was previously described by Poole-Frenkel [64], according to  $\mu \propto \sqrt{\gamma E}$ , where  $\gamma$  is a field enhancement parameter. In initial charge transport studies on conjugated polymers the steeper increase of the SCLCs at high voltages was attributed to the field dependence of the mobility. Later on also the effect of the charge carrier density on carrier mobility was considered [65]. In SCL diodes, an increase of the applied voltage simultaneously increases the applied field as well as the charge carrier density. Therefore, the effect of charge carrier density and electric field on charge carrier mobility is not explicit [66]. The so-called Extended Gaussian Disorder Model, described by Pasveer et al., includes also the dependency of the mobility on carrier density, together with temperature and electric field [65]. The numerical equations in the model are described as,

$$\mu_n(T, n, E) \approx \mu_n(T, n)f(T, E) \quad 1.16$$

$$\mu_n(T, n) = \mu_0(T) \exp\left[\frac{1}{2}(\hat{\sigma}^2 - \hat{\sigma})(2na^3)^\delta\right] \quad 1.17$$

$$\mu_0(T) = \mu_\infty \exp[-C\hat{\sigma}^2] \quad 1.18$$

$$\delta \equiv 2 \frac{\ln(\hat{\sigma}^2 - \hat{\sigma}) - \ln(\ln(4))}{\hat{\sigma}^2} \quad 1.19$$

$$f(T, E) = \exp\left\{0.44(\hat{\sigma}^{3/2} - 2.2) \left[\sqrt{1 + 0.8\left(\frac{Eqqa}{\sigma}\right)^2} - 1\right]\right\} \quad 1.20$$

where  $\mu_0(T)$  is the mobility at zero charge carrier density and electric field,  $a$  is the average intersite spacing,  $q$  is the elementary charge,  $n$  is the charge-carrier density,  $\hat{\sigma} \equiv \sigma/kT$  and  $c=0.42$ . In the model  $\mu_0(T)$ ,  $a$  and  $\sigma$  are the fitting parameters to describe the experimental  $J$ - $V$  characteristics. The authors conclude that the calculated mobilities should be considered as the average of the interchain and intrachain hopping [65]. It has been showed that at room temperature the mobility is affected more by the carrier density as compared to electric field [66].

## **1.9. Drift-diffusion modeling of organic semiconductors**

Numerical simulations of semiconductor devices (solar cells, organic light emitting diodes and single carrier devices) are of great importance in order to interpret and predict their performance. For this purpose a one dimensional drift-diffusion model to simulate the current-voltage characteristics of organic diodes has been developed [45]. In this model, drift and diffusion of charge carriers, the effect of space charge on the electric field, density-dependent mobility, Langevin-type recombination, universal trap distribution for the electrons, and a field- and temperature-dependent generation rate of free charge carriers are included. In the drift-diffusion simulations device parameters like charge carrier mobility, amount of disorder, and the average intersite spacing are used as fit parameters to describe the  $J$ - $V$  characteristics of single carrier devices. In the case of solar cells, the maximum generation rate, decay rate of the bound  $e$ - $h$  pair and their initial separation are used as fit parameters.

## **1.10. Scope and outline of the thesis**

In this thesis the effect of non-ohmic contacts on the open circuit-light intensity dependence and charge transport characteristics in n-type organic materials are studied. In recent years new n-type materials have gained an increased attention with as main aim the replacement of the well-known n-type fullerene derivatives in organic BHJ solar cells. Although fullerenes have been the work horse for acceptors in organic solar cells, their relatively high price and limited absorption have stimulated the search for alternative n-type materials.

In chapter 2, the effect of non-ohmic contacts on the open circuit-light intensity dependence is studied in MEH-PPV:PCBM solar cells, using intentionally created electron and hole injection barriers. Both from experiments and from drift-diffusion simulations it is shown that the dependence of the open circuit on light intensity is decreased in the case of non-ohmic contacts, and an analytical formula is derived for this particular case. This study shows that the decreased slope of open circuit-light intensity dependence is the result of the absence of band bending in the vicinity of non-ohmic contacts.

In chapter 3, electron- and hole charge transport is studied in blends of P3HT (donor) and a commercial perylene diimide derivative (PDI) (acceptor). As-cast hole-only and electron-only devices of the blend have been fabricated and analyzed. It is shown that upon annealing the electron transport becomes injection limited. Due to this injection limitation the electron current is not space-charge limited and the electron mobility cannot be

extracted directly from the  $J$ - $V$  characteristics. The hole transport is space-charge limited before and after annealing.

In chapter 4, the electrical behavior of solar cells based on P3HT:PDI blends are studied. For these solar cells a decrease in open circuit voltage is observed upon annealing. This open-circuit voltage decrease is correlated with the occurrence of an electron injection barrier upon annealing. In agreement with the observation in Chapter 2 this leads to a decreased dependence of the open circuit-light on light intensity dependence for the annealed P3HT:PDI solar cells. The electron mobility after annealing is estimated from drift-diffusion simulations of as-cast and annealed solar cells. The increase in photocurrent in the solar cells upon annealing is attributed to the increased electron mobility upon annealing.

In chapter 5, the charge transport and solar cell performance are studied in blends of P3HT and ortho-substituted perylene diimide derivatives. Drift-diffusion simulations are carried out for the hole-only and electron-only devices of these blends. As compared to the commercial PDI derivative (chapter 4) solar cells performances are slightly improved. The effects of injection barriers upon annealing both in electron-only devices and in solar cells are discussed.

In chapter 6, the effect of molecular weight on the electron transport of a conjugated polymer with naphthalene diimide core and bithiophene unit (N2200) is studied. N2200 is a promising n-type organic semiconductor. Compared to the commercial N2200 we find that in the series studied here with different molecular weights, the electron transport is reduced by an order of magnitude. This reduction is attributed to trapping sites, which most probably remained from the synthesis of the materials. It is shown that the electron mobility of N2200 is not strongly affected by the molecular weight with the change in the mobility.

## 1.11. References

- [1] F. Estrada, P. Perron, and B. Martínez-López, *Nat. Geosci.* **6**, 1050 (2013).
- [2] Environmental and Energy Study Institute, <http://www.eesi.org/topics/fossil-fuels/description>, Accessed 15.09.2016.
- [3] Four Peaks Technologies, [http://solarcellcentral.com/solar\\_page.html](http://solarcellcentral.com/solar_page.html), Accessed 15.09.2016.
- [4] D. M. Chapin, C. S. Fuller, and G. L. Pearson, *J. Appl. Phys.* **25**, 676 (1954).
- [5] A. E. Becquerel, *C. R. Acad. Sci.* **9**, 145 (1839).
- [6] H. Hertz, *Ann. Phys.* **267**, 983 (1887).
- [7] A. Pochettino and A. Sella, *Acad. Lincei Rendus* **15**, 355 (1906).
- [8] C. K. Chiang, C. R. Fincher, Jr., Y. W. Park, A. J. Heeger, H. Shirakawa, E. J. Louis, S. C. Gau, and Alan G. MacDiarmid, *Phys Rev Lett.* **39**, 1098 (1977).
- [9] S.R. Forrest, *Nature*, **428**, 911 (2004).
- [10] R. Søndergaard, M. Hösel, D. Angmo, T. T. Larsen-Olsen, and F. C. Krebs, *Mater. Today* **15**, 36 (2012).
- [11] Heliatek, <http://www.heliatek.com/en/press/press-releases/details/heliatek-sets-new-organic-photovoltaic-world-record-efficiency-of-13-2>, Accessed 15.09.2016.
- [12] NREL, National Center for Photovoltaics, <http://www.nrel.gov/ncpv/>, Accessed 15.09.2016.
- [13] UCDavisChemWiki, [http://chem.libretexts.org/Textbook\\_Maps/Organic\\_Chemistry\\_Textbook\\_Maps/Map%3A\\_Organic\\_Chemistry\\_\(Smith\)/Chapter\\_01%3A\\_Structure\\_and\\_Bonding/1.9%3A\\_Ethane,\\_Ethylene,\\_and\\_Acetylene](http://chem.libretexts.org/Textbook_Maps/Organic_Chemistry_Textbook_Maps/Map%3A_Organic_Chemistry_(Smith)/Chapter_01%3A_Structure_and_Bonding/1.9%3A_Ethane,_Ethylene,_and_Acetylene), Accessed 15.09.2016.
- [14] W. Brütting, *Physics of Organic Semiconductors* (Wiley-VCH, Weinheim, 2005).
- [15] W. C. H. Choy, *Organic Solar Cells: Materials and Device Physics* (Springer, London, 2013).
- [16] R. E. Peierls, *Quantum Theory of Solids* (Clarendon Press, Oxford, 1955).
- [17] W. Graupner, G. Leditzky, and G. Leising, *Phys. Rev. B.* **54**, 7610 (1996).
- [18] P. Yang, E. R. Batista, S. Tretiak, A. Saxena, R. L. Martin, D. L. Smith, *Phys. Rev. B* **76**, 241201 (2007).
- [19] S. M. Sze, *Physics of Semiconductor Devices* (Wiley, New York, 1981).

- [20] C. Brabec, U. Scherf, and V. Dyakonov, *Organic Photovoltaics: Materials, Device Physics, and Manufacturing Technologies* (Wiley-VCH, Weinheim, 2008)
- [21] S.M. Sze and K. K. Ng, *Physics of Semiconductor Devices* (Wiley-VCH, Weinheim, 2006)
- [22] O.V. Mikhnenko, P. W. M. Blom, T.-Q. Nguyen, *Energy Environ. Sci.* **8**, 1867 (2015).
- [23] C. Deibel and V. Dyakonov, *Rep. Prog. Phys.* **73**, 096401 (2010).
- [24] H. Bässler and A. Kohler, *Charge Transport in Organic Semiconductors*, *Top. Curr. Chem.*, **312**, 1 (2011).
- [25] R. H. Friend, D. D. C. Bradley, and P. D. Townsend, *J. Phys. D: Appl. Phys.* **20**, 1367 (1987).
- [26] L. J. A. Koster, V. D. Mihailetchi, and P. W. M. Blom, *Appl. Phys. Lett.* **88**, 093511 (2006).
- [27] D. Credgington, R. Hamilton, P. Atienzar, J. Nelson, and J. R. Durrant, *Adv. Funct. Mater.* **21**, 2744 (2011).
- [28] G. Lakhwani, A. Rao, and R. H. Friend, *Annu. Rev. Phys. Chem.* **65**, 557 (2014).
- [29] V. D. Mihailetchi, L. J. A. Koster, J. C. Hummelen, and P.W. M. Blom, *Phys. Rev. Lett.* **93**, 216601 (2004).
- [30] L. J. A. Koster, V. D. Mihailetchi, R. Ramaker, and P. W. M. Blom, *Appl. Phys. Lett.* **86**, 123509 (2005).
- [31] M. M. Mandoc, F. B. Kooistra, J. C. Hummelen, B. de Boer, and P. W. M. Blom, *Appl. Phys. Lett.* **91**, 263505 (2007).
- [32] M. Kuik, H. T. Nicolai, M. Lenes, G. A. H. Wetzelaer, M. Lu, and P. W. M. Blom, *Appl. Phys. Lett.* **98**, 093301 (2011).
- [33] M. Kuik, L. J. A. Koster, G. A. H. Wetzelaer, and P. W. M. Blom, *Phys. Rev. Lett.* **107**, 256805 (2011).
- [34] P. de Bruyn, A. H. P. van Rest, G. A. H. Wetzelaer, D. M. de Leeuw, and P.W. M. Blom, *Phys. Rev. Lett.* **111**, 186801 (2013).
- [35] N. F. Mott and R. W. Gurney, *Electronic Processes in Ionic Crystals* (Oxford University Press, London, 1940).
- [36] P. N. Murgatroyd, *J Phys D: Appl Phys.* **3**, 151 (1970).
- [37] J. C. Scott, and G. G. Malliaras, *Chem. Phys. Lett.* **299**, 115 (1999).
- [38] P. S. Davids, I. H. Campbell, and D. L. Smith, *J. Appl. Phys.* **82**, 6319 (1997).



- [39] A. K. Mahapatro and S. Ghosh, *Appl. Phys. Lett* **80**, 4840 (2002).
- [40] G. G. Malliaras and J. C. Scott, *J. Appl. Phys* **85**, 7426 (1999).
- [41] Charles L. Braun, *J. Chem. Phys.* **80**, 4157 (1984).
- [42] W. Schottky, *Naturwissenschaften* **26**, 843 (1938).
- [43] N. I. Craciun, J. J. Brondijk, and P. W. M. Blom, *Phys. Rev. B* **77**, 035206 (2008).
- [44] A. M. Goodman and A. Rose, *J. Appl. Phys* **42**, 2823 (1971).
- [45] L. J. A. Koster, E. C. P. Smits, V. D. Mihailetschi, and P. W. M. Blom, *Phys. Rev. B* **72**, 085205 (2005).
- [46] V. D. Mihailetschi, J. Wildeman, and P. W. M. Blom, *Phys. Rev. Lett.* **94**, 126602 (2005).
- [47] V. D. Mihailetschi, L. J. A. Koster, J. C. Hummelen, and P. W. M. Blom, *Phys. Rev. Lett.* **93**, 216601 (2004).
- [48] L. Onsager, *J. Chem. Phys* **2**, 599 (1934).
- [49] C. L. Braun, *J. Chem. Phys* **80**, 4157 (1984).
- [50] C. Tanase, E. J. Meijer, P. W. M. Blom, and D. M. de Leeuw, *Phys. Rev. Lett.* **91**, 216601-1 (2003).
- [51] P. W. M. Blom, M. J. M. de Jong, and J. J. M. Vlegaar, *Appl. Phys. Lett* **68**, 3308 (1996).
- [52] V. Kažukauskas. *Semicond. Sci. Technol.* **19**, 1373 (2004).
- [53] H. T. Nicolai, M. Kuik, G. A. H. Wetzelaer, B. de Boer, C. Campbell, C. Risko, J. L. Brédas, and P. W. M. Blom, *Nat. Mater.* **11**, 882 (2012).
- [54] P. Langevin, *Ann. Chim. Phys.* **28**, 433 (1903).
- [55] L. J. A. Koster, V. D. Mihailetschi, and P. W. M. Blom, *Appl. Phys. Lett* **88**, 052104 (2006).
- [56] G. Juška, K. Genevičius, N. Nekrašas, and G. Sliaužys, *Phys. Status Solidi C* **7**, 980. (2010).
- [57] M. Kuik, L. J. A. Koster, G. A. H. Wetzelaer, and P. W. M. Blom, *Phys. Rev. Lett.* **107**, 256805 (2011).
- [58] W. Shockley and W. T. Read, *Phys. Rev.* **87**, 835 (1952).
- [59] H. T. Nicolai, M. M. Mandoc, and P. W. M. Blom, *Phys. Rev. B* **83**, 195204 (2011).
- [60] H. Bässler, *Phys. Status Solidi B* **175**, 15 (1993).
- [61] A. L. Efros, *Sov. Phys. Semicond.* **16**, 772 (1982).

- [62] A. Miller and E. Abrahams, *Phys. Rev.* **120**, 745 (1960).
- [63] I. I. Fishchuk, A. K. Kadashchuk, J. Genoe, Mujeeb Ullah, H. Sitter, Th. B. Singh, N. S. Sariciftci, and H. Bäessler, *Phys. Rev. B* **81**, 045202 (2010).
- [64] J. Frenkel, *Phys. Rev.* **54**, 647 (1938).
- [65] W. F. Pasveer, J. Cottaar, C. Tanase, R. Coehoorn, P. A. Bobbert, P. W. M. Blom, D. M. de Leeuw, and M. A. J. Michels, *Phys. Rev. Lett.* **94**, 206601 (2005).
- [66] C. Tanase, P. W. M. Blom, and D. M. de Leeuw, *Phys. Rev. B* **70**, 193202 (2004).

## **2. Effect of non-ohmic contacts on the light intensity dependence of the open-circuit voltage in organic solar cells**

The effect of contact barriers on the light-intensity dependence of the open-circuit voltage of organic solar cells is investigated in experiment and simulation. Reduced light-intensity dependence is found when the open-circuit voltage surpasses the built-in voltage, leading to a slope of  $kT/2q$  for a device with one non-ohmic contact and a slope of zero for a device with two non-ohmic contacts. It has been shown that the reduced light-intensity dependence of the open-circuit voltage is not caused by entering a contact-recombination-limited regime, but by the absence of band bending in the vicinity of a non-ohmic contact.

## 2.1. Introduction

In the introduction of the thesis it has been explained that the photogenerated charge carriers are transported through the donor and acceptor phases of the bulk heterojunction (BHJ) blend, followed by charge extraction at the electrodes [1]. However, part of the photogenerated carriers is lost through nongeminate recombination processes. Nongeminate recombination in organic semiconductors is manifested as bimolecular recombination or trap-assisted recombination [2,3]. It has been shown that to address the nature of nongeminate recombination, the open-circuit voltage can be studied as a function of light intensity [4]. At the open-circuit voltage, the current is zero, implying that all carriers recombine.

In case of only bimolecular recombination the open-circuit voltage ( $V_{oc}$ ) can be described as [4]

$$V_{oc} = \frac{E_{gap}}{q} - \frac{kT}{q} \ln \left( \frac{\gamma N_c^2}{G} \right) \quad 2.1$$

where  $E_{gap}$  is the energy gap between the highest occupied molecular orbital (HOMO) of the donor and the lowest unoccupied molecular orbital (LUMO) of the acceptor, which is closely related to the charge-transfer state energy [5],  $q$  is the elementary charge,  $k$  is the Boltzmann constant,  $T$  is the temperature,  $\gamma$  is the bimolecular recombination strength,  $N_c$  is the density of states, and  $G$  is the generation rate of charge carriers. Note that for a system with Gaussian energetic disorder,  $E_{gap}$  is reduced by a term  $\sigma^2/kT$  [6,7]. Since the generation rate is proportional to the light intensity ( $I$ ), the open-circuit voltage increases with increasing light intensity, characterized by a slope ( $S$ ) of  $kT/q$  when  $V_{oc}$  is plotted against the natural logarithm of light intensity. However, when trap-assisted recombination is present, this slope increases [8]. As a result, the light-intensity dependence of  $V_{oc}$  can be used to determine the dominant recombination process in organic solar cells.

It has been shown in literature that the open-circuit voltage can be limited by contact recombination (minority carriers leaving the device through the contact), which would result in a reduction of the  $V_{oc}$ -light intensity slope [9,10]. Such process is on the other hand not likely to occur in a solar cell with ohmic contacts, since the (majority-carrier) charge density in the vicinity of the electrodes is so high that bimolecular recombination is favorable [11].

Here, we investigate the effect of non-ohmic contacts on the light-intensity dependence of the open-circuit voltage, noting that the Eq. 2.1 is valid only in the case of ohmic contacts. A reduced light-intensity dependence is found when the open-circuit

voltage surpasses the built-in voltage, leading to a slope of  $kT/2q$  for a device with one non-ohmic contact and a slope of zero for a device with two non-ohmic contacts. Interestingly, in these regimes, the device is dominated by bulk recombination, rather than contact recombination.

## **2.2. Ohmic and non-ohmic contacts in an organic diode and their effect on open circuit voltage**

In an undoped organic diode, such as an organic solar cell, the built-in voltage ( $V_{bi}$ ) is determined by the difference in work function of the electrodes. The built-in voltage is maximized in the case of an ohmic electron and hole contact. In case of an ohmic electron contact, the fermi level of the electrode is pinned to the LUMO of the acceptor. Diffusion of electrons into the semiconductor results in band bending, which reduces the built-in voltage [12]. The same holds for an ohmic hole contact, resulting in band bending of the HOMO of the donor.

Upon irradiation with light, a photogenerated current is established, which is driven by the built-in electric field. At the open-circuit voltage, the photogenerated current is compensated by the diffusion-driven current of charges injected by the electrodes. Increasing the light intensity results in an enhanced photogenerated current, this has to be compensated by an increased injection current at  $V_{oc}$ , requiring a higher applied voltage. As a result,  $V_{oc}$  increases with light intensity. In case of non-ohmic contacts, the built-in field is reduced, resulting in a lower open-circuit voltage [13].

At sufficiently high light intensities, the open-circuit voltage may become higher than the built-in voltage, which corresponds to the situation of essentially flat energy bands, apart from band bending effects at the contacts. In case of an ohmic contact, high light intensities will give rise to a decreased band bending at the contact under open-circuit conditions. This is the result of a high photogenerated carrier density throughout the bulk of the layer, reducing the net effect of the band bending due to diffused carriers from the contact. The reduced band bending gives rise to an increased open-circuit voltage, and results in a light-intensity dependent  $V_{oc}$  even when it surpasses the initial  $V_{bi}$ . In case of a non-ohmic contact, band bending at the contact is not present, limiting the open-circuit voltage when flat-band conditions are reached.

As depicted in Figure 2.1, these effects result in different light intensity dependencies for different contact configurations. For the device with two ohmic contacts

(Figure 2.1(a)), the difference in fermi levels of the contacts (defining  $V_{oc}$ ) continues to increase with increasing light intensity, even when the initial built-in voltage is surpassed. For the device with a non-ohmic electron contact (Figure 2.1(b)), the Fermi level of the electron contact no longer rises with increasing light intensity when flat-band conditions are reached (at the built-in voltage). The Fermi level of the hole contact, on the other hand, continues to lower as a result of band-bending reduction. This results in a reduced light-intensity dependence of  $V_{oc}$  when it surpasses the built-in voltage. For the device with two non-ohmic contacts the built-in voltage is determined by the difference in work function of the two electrodes (Figure 2.1(c)). In that case, band bending at the contacts is not present; giving rise to intensity independent  $V_{oc}$  once the built-in voltage is reached.

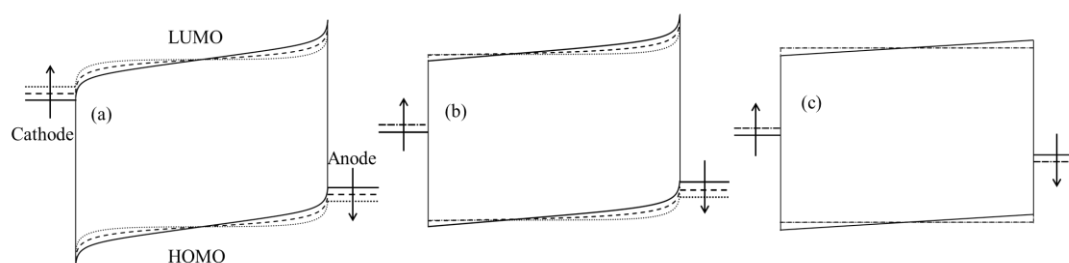


Figure 2.1. Energy band diagrams for solar cells in open circuit with two ohmic contacts (a), a barrier at the cathode and an ohmic anode (b), barriers at both electrodes (c). The diagrams are drawn going from solid, *via* dashed, to dotted lines with increasing light intensity. The arrows indicate the movement of the electrode Fermi levels with increasing light intensity, where the difference between the anode and cathode levels defines the open-circuit voltage. In case of a non-ohmic contact, the dotted line overlaps with the dashed line at the contact, indicating that a maximum has been reached (flat bands).

### 2.3. Effect of contact barriers on dependence of open circuit voltage on light intensity

In order to investigate the effect of contact barriers at either one or both contacts, drift diffusion simulations are pursued [14]. In Figure 2.2 simulations are shown for a device with different barriers at the contacts and bulk recombination is assumed to be bimolecular, while the contact recombination velocity is implicitly assumed to be infinite. As expected, when both contacts are ohmic, the slope of  $V_{oc}$  vs  $\ln(I)$  amounts to  $kT/q$  over the complete

light-intensity range. When the barrier at the electron contact is increased, a transition to a  $kT/2q$  intensity dependence is observed at high light intensities. It is observed that this transition takes place when  $V_{oc}$  equals to the built-in voltage, in agreement with the aforementioned reasoning. In the case that there is a barrier present at both electron- and hole contact, which are kept equal in the simulations, at sufficient light-intensity no slope is observed as mentioned in the previous section.

The open-circuit voltage in case of a non-ohmic electron contact can also be described analytically. Eq. (2.1) can be rewritten as

$$V_{oc} = \frac{E_{gap}}{q} - \frac{kT}{q} \ln\left(\frac{N_c^2}{np}\right) \quad 2.2$$

and the electron density at the cathode in terms of the contact barrier  $\phi_b$  reads

$$n = N_c \exp(-\phi_b/kT) \quad 2.3$$

The generation rate equals the recombination rate at  $V_{oc}$ , and can be written as  $G = \gamma np$ . Substitution of Eq. (2.3) into Eq. (2.2) and using the approximation  $n = p$  gives

$$V_{oc} = \frac{E_{gap}}{q} - \frac{\phi_b}{q} - \frac{kT}{2q} \ln\left(\frac{N_c^2}{p^2}\right) = \frac{E_{gap}}{q} - \frac{\phi_b}{q} - \frac{kT}{2q} \ln\left(\frac{\gamma N_c^2}{G}\right) \quad 2.4$$

Indeed, the analytical formula predicts a slope of  $kT/2q$  for  $V_{oc}$  vs  $\ln(I)$ . For a device with two non-Ohmic contacts, as discussed on the basis of the band diagrams in Figure 2.1, the simulations show an intensity-independent  $V_{oc}$  once the built-in voltage is reached (red line), which is given by exactly the difference in the Fermi levels of the contacts.

#### **2.4. Role of contact- and bulk recombination on the open circuit voltage at high light intensities**

The decreased slope at high intensities in an open-circuit voltage vs light intensity plot has been associated with a contact-recombination-limited regime in literature, whereas the higher slope in the low-intensity regime was associated with bulk recombination [9]. However, by examining the rates of charge carriers that are lost at the contacts in comparison to the bimolecular recombination rate, it is found that in the  $S=kT/2q$  regime bulk recombination is dominant, whereas contact recombination is dominant in the  $S = kT/q$  regime. This is displayed in Figure 2.3, where the electron and hole currents in the device at  $V_{oc}$  are compared to the bimolecular-recombination current density, calculated as  $J_{rec} =$

$q\gamma n p L$ , with  $L$  the layer thickness. The electron current towards the cathode is driven by the electric field and is compensated by an equal diffusion-driven hole current towards the cathode, ensuring that the total current equals zero (open circuit). At high light intensities where  $S=kT/2q$  (solid lines), the calculated recombination current is substantially higher than the currents at the cathode, while at low intensities (dashed lines), the relative amount of bimolecular recombination decreases. This result is expected when considering the band diagrams in Figure 2.1. The electric field at the cathode is reduced at increased light intensities, lowering the driving force for electrons to escape at the cathode and thus promoting bimolecular recombination.

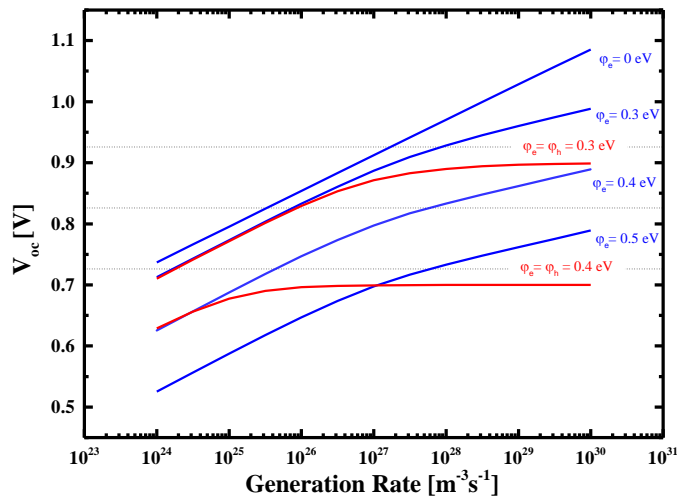


Figure 2.2. Simulated open-circuit voltage as a function of generation rate (proportional to light intensity) for devices with barriers at only the cathode (blue lines) and both cathode and anode (red lines). The dotted lines indicate the built-in voltages for devices with only one barrier, defined by  $qV_{bi} = E_{\text{gap}} - \varphi_e - b$ , where  $b = 0.27$  eV is the band-bending parameter at the anode for a layer thickness of 100 nm [12]. The simulations are performed with  $E_{\text{gap}} = 1.5$  eV, mobilities  $\mu_e = \mu_h = 1 \times 10^{-8} \text{ m}^{-2} \text{ V}^{-1} \text{ s}^{-1}$ , and Langevin recombination.

## 2.5. Experimental verification of light-intensity dependence of open circuit voltage in organic solar cells

In order to experimentally verify the effect of contact barriers on the slope of the open circuit voltage-light intensity dependence at high light intensities, solar cells with ohmic contacts and with intentionally created contact barriers are studied. As active layer a blend



of MEH-PPV:PCBM in 1:4 ratio is used. As ohmic contacts PEDOT:PSS (holes) and Ba/Al (electrons) are used, for non-ohmic contacts we use Al (electrons) and Au (holes). The sample preparation procedure is given in Section 2.7. Figure 2.4 shows the experimental open-circuit voltage as a function of incident light intensity for the fabricated solar cells. As expected, the open-circuit voltage decreases when contact barriers are introduced. Moreover, for the devices with contact barriers, a transition is observed to a weaker light-intensity dependence at higher illumination intensities. Indeed, for the device with only a barrier at the electron contact (Al), the slope of  $V_{oc}$  vs  $\ln(I)$  decreases from  $kT/q$  to  $kT/2q$  with increasing illumination intensity, while for the device with an ohmic electron contact (Ba/Al) the slope remains at  $kT/q$ . In the device with barriers at both the anode (Au) and cathode (Al), the open-circuit voltage is observed to saturate to a constant value at high light intensities, corresponding to the built-in voltage (0.32). The experimental results are in agreement with the corresponding simulations, which yield an electron barrier of 0.4 eV at the Al contact, and a hole barrier of 0.75 eV at the Au contact. In the simulations, the generation rate was obtained from the photogenerated current and was 15 % lower for the device with the semitransparent Au contact.

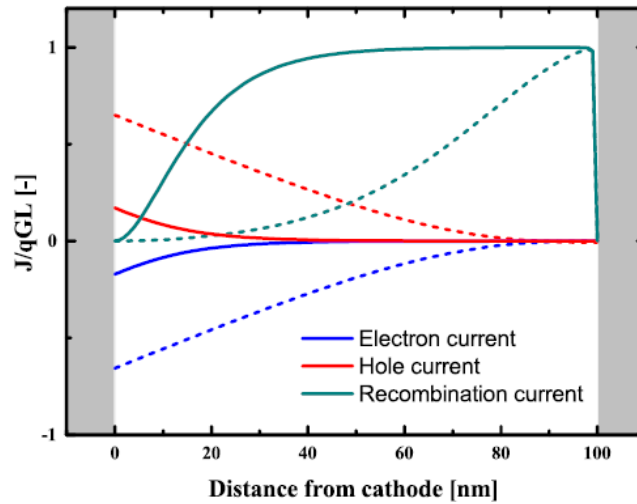


Figure 2.3. Electron, hole and recombination currents densities, normalized by the total photocurrent density  $qGL$ , across a device with a layer thickness of 100 nm for  $G = 1 \times 10^{28} \text{ m}^{-3} \text{ s}^{-1}$  (solid lines) and  $G = 1 \times 10^{25} \text{ m}^{-3} \text{ s}^{-1}$  (dashed lines), using the same simulation parameters as in Figure 2.2. The figure indicates an increasing contribution of bimolecular recombination with respect to contact recombination with increasing intensity.

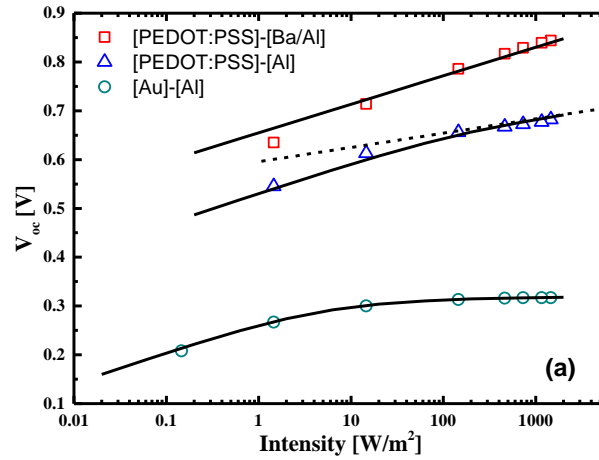


Figure 2.4. Experimental open-circuit voltage as a function of light intensity with different contact barriers (symbols) with corresponding simulations (solid lines) with  $E_{\text{gap}} = 1.42$  eV. The dotted line is calculated with Eq. (2.4).

Finally, to investigate if the transition to a slope of  $kT/2q$  indeed occurs at the built-in voltage for the device with one non-ohmic contact, the built-in voltage is determined from the dark current density-voltage characteristics, using an analytical drift-diffusion model [12], as displayed in Figure 2.5. The built-in voltage is the voltage at which a transition from a diffusion-governed current to a drift current occurs [12]. The model gives a built-in voltage of 0.64 V, corresponding well with the transition point in the  $V_{\text{oc}}$  vs  $\ln(I)$  characteristic (Figure 2.4). A built-in voltage of 0.30 V was determined for the device with two non-ohmic contacts, in good agreement with the saturated  $V_{\text{oc}}$  of 0.32 V. The built-in voltage of the device with ohmic contacts was determined to be 0.90 V, which is above  $V_{\text{oc}}$  for the complete intensity range.

## 2.6. Conclusions

In conclusion, the effect of contact barriers on the light-intensity dependence of the open-circuit voltage was investigated. Both in simulation and experiment, it was shown that a barrier at one contact causes a transition in the  $V_{\text{oc}}$  vs intensity behavior, resulting in a slope of  $kT/q$  at low intensities and a slope of  $kT/2q$  at high intensities. The transition takes place when  $V_{\text{oc}}$  reaches the built-in voltage. An analytical formula was derived, which confirms

the slope of  $kT/2q$ . In the case of barriers present at both contacts, the open-circuit voltage saturates at the built-in voltage and becomes intensity independent. Contrary to earlier reports, it was shown that a decreased light-intensity dependence of  $V_{oc}$  is not the result of contact-recombination effects becoming dominant, but is the result of the absence of band bending in the vicinity of non-ohmic contacts.

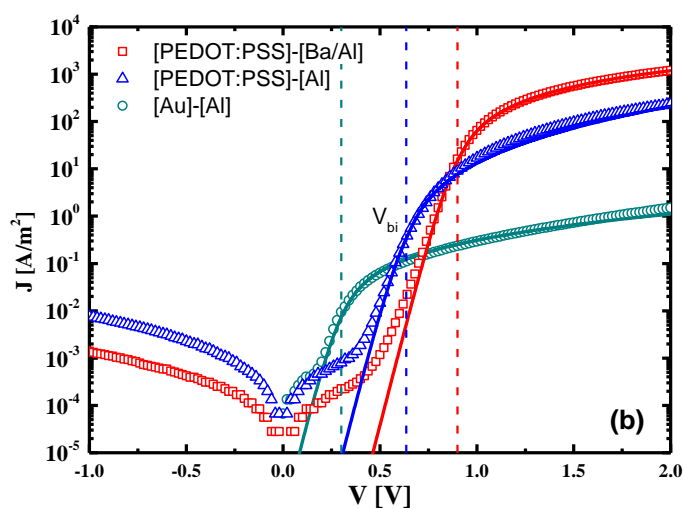


Figure 2.5. Experimental dark current vs voltage (symbols) indicating the shift in built-in voltage as a result of the barrier at the cathode. The solid lines are fits to the experiment using an analytical drift-diffusion model [12], to obtain the built-in voltages (dashed lines).

## 2.7. Experimental

Devices were fabricated on glass substrate with indium tin oxide (ITO). ITO substrates were cleaned with detergent agent and ultrasonicated in acetone and isopropanol, and cleaning finished with UV-ozone treatment. The solar cells consist of a poly(2-methoxy,5-(2-ethyl-hexyloxy)-1,4-phenylenevinylene) (MEH-PPV) donor and 6,6-phenyl C61-butyric acid methyl ester (PCBM) acceptor in a 1:4 ratio in the active layer. For devices with two ohmic contacts, the active layers were sandwiched between a bottom anode of ITO substrates coated with poly(3,4-ethylenedioxythiophene):poly(styrenesulfonate) (PEDOT:PSS) anode (2000 rpm, 55 nm) and Barium(Ba)(5 nm)/Aluminum(Al)(100 nm) cathode, which are ohmic hole and electron contacts, respectively. In order to introduce a barrier on the cathode side, the Ba interlayer was omitted in some devices. For devices with

*Chapter 2: Effect of non-ohmic contacts on the light intensity dependence of the open-circuit voltage in organic solar cells*

contact barriers on both sides, an additional barrier at the anode was introduced by using a semitransparent 10 nm gold (Au) layer on top of the ITO substrates. The fabricated solar cells were measured in a nitrogen atmosphere in dark and under illumination of a white halogen lamp with an irradiance of  $1460 \text{ W/m}^2$  with Keithley 2400 source meter. A set of neutral density filters is used to vary the illumination intensity.

## 2.8. References

- [1] G. Yu, J. Gao, J.C. Hummelen, F. Wudl, and A. J. Heeger, *Science* **270**, 1789 (1995).
- [2] P. Langevin, *Ann. Chim. Phys.* **28**, 433 (1903).
- [3] W. Shockley and W. T. Read, *Phys. Rev.* **87**, 835 (1952).
- [4] L. J. A. Koster, V. D. Mihailetschi, R. Ramaker, and P. W. M. Blom, *Appl. Phys. Lett.* **86**, 123509 (2005).
- [5] K. Tvingstedt, K. Vandewal, A. Gadisa, F. Zhang, J. Manca, and O. Ingana, *J. Am. Chem. Soc.* **131**, 11819 (2009).
- [6] J. C. Blakesley, and N. C. Greenham, *J. Appl. Phys.* **106**, 034507 (2009).
- [7] J. C. Blakesley, and D. Neher, *Phys. Rev. B* **84**, 075210 (2011).
- [8] M. M. Mandoc, F. B. Kooistra, J.C. Hummelen, B. De Boer, and P. W. M. Blom, *Appl. Phys. Lett.* **91**, 263505 (2007).
- [9] T. Kirchartz, W. Gong, S. A. Hawks, T. Agostinelli, R. C. I. MacKenzie, Y. Yang, and J. Nelson, *J. Phys. Chem. C* **116**, 7672 (2012).
- [10] S. Wheeler, F. Deledalle, N. Tokmoldin, T. Kirchartz, J. Nelson, and J. R. Durrant, *Phys. Rev. Applied* **4**, 024020 (2015).
- [11] J. Kniepert, I. Lange, N. J. van der Kaap, L. J. A. Koster, and D. Neher, *Adv. Energy Mater.* **4**, 1301401 (2014).
- [12] P. de Bruyn, A. H. P. van Rest, G. A. H. Wetzelaer, D. M. de Leeuw, and P.W. M. Blom, *Phys. Rev. Lett.* **111**, 186801 (2013).
- [13] V. D. Mihailetschi, P. W. M. Blom, J. C. Hummelen, and M. T. Rispens, *Appl. Phys. Lett.* **94**, 6849 (2003).
- [14] L. J. A. Koster, E. C. P. Smits, V. D. Mihailetschi, and P. W. M. Blom, *Phys. Rev. B* **72**, 085205 (2005).



### **3. Charge transport in P3HT:perylene diimide blends**

The electron and hole transport of blends of regioregular poly(3-hexylthiophene) (rr-P3HT) donor and commercial perylene-3,4,9,10-perylene tetracarboxylic acid diimides (PDI-1) is investigated using electron-only and hole-only devices. Trap-free space-charge-limited electron and hole currents are shown for electron and hole-only devices of as-cast P3HT:PDI-1 blends, respectively. The mobility of electrons and holes in the as-cast devices are lower as compared to the well-known P3HT:fullerene blends. Upon annealing the electron current in the P3HT:PDI-1 blend becomes injection-limited, and the electron mobility cannot be determined directly from the  $J$ - $V$  characteristics.

### 3.1. Introduction

Perylene-3,4,9,10-perylene tetracarboxylic acid diimides (PDIs) have aroused as new alternative materials for fullerene derivatives, the common acceptor material for organic electronic applications. PDIs have been applied in solar cells, single carrier devices and in field-effect transistors (FETs) [1-8].

The common fullerene acceptors have a unique three dimensional structure, but the possibility to tune their LUMO energy is limited [9]. Another drawback of fullerene acceptors is their relatively low optical absorption. In addition, the synthesis of fullerene derivatives is difficult and therefore fullerenes are relatively expensive [10]. These drawbacks turned the interest to materials with higher optical absorption and lower cost and higher stability [11,12]. At this point, PDIs became an attractive class of alternative acceptor materials. They compromise strong light absorption in the visible part of the spectrum [13]. Moreover, unlike fullerene derivatives, PDIs have several functional positions to make synthetic modifications, like the peri-, bay- and ortho- positions as schematically shown in Figure 3.1 [13]. This is a very important advantage of PDIs in order to design new materials for future organic electronic applications with desired properties. It has been shown in literature from FET measurements that PDI derivatives have an electron mobility of  $6 \times 10^{-7} \text{ m}^2/\text{Vs}$  in the crystalline phase [6,13]. Although PDIs exhibit a higher absorption than fullerene derivatives, the efficiency of solar cells with PDI acceptors remained significantly lower than solar cells with fullerene acceptors [2]. The low performance of solar cells with PDI acceptors has been attributed to self-trapping of excitons in their large aggregated domains [2]. In a study by Singh et al., the formation of PDI aggregates at different annealing temperatures was investigated and it was shown that PDI aggregates actually contribute to the photogeneration of charge carriers. However, their improper alignment is thought to be responsible for the decreased solar cell performance in annealed PDIs [8]. In order to add more insight to the device operation of PDI-based bulk heterojunction solar cells, it is crucial to investigate the charge transport characteristics. This can be carried out by studying temperature-dependent electron and hole currents in single-carrier devices of blends with PDI as the acceptor material.



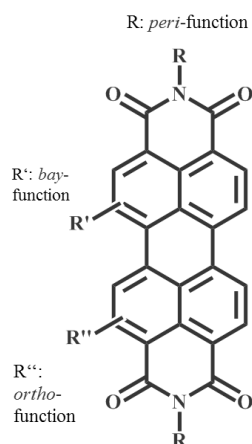


Figure 3.1. Molecular structure of perylene-3,4,9,10-perylene tetracarboxylic acid diimide structure with its functionalizing positions.

In organic semiconductors, electron transport is frequently limited by electron trapping, while hole transport shows trap-free charge transport characteristics [14]. It was demonstrated that a universal trap level located at  $\sim -3.6$  eV below vacuum level is responsible for the trapping of electrons. As a result, it is expected that organic semiconductors with a LUMO below 3.6 eV, meaning that the trap-level is outside the band gap, should exhibit trap-free electron transport. Next to trap-free electron transport such semiconductors would also be more stable against the presence of water and oxygen [15,16]. Typical PDI materials, also the commercial PDI derivative used in this chapter (see Figure 3.2b), fulfill this requirement with their deep LUMO  $\sim -3.8$  eV, the HOMO is located around  $\sim -5.8$  eV. In this chapter, the electron and hole transport in P3HT:PDI-1 blends are studied using electron-only and hole-only devices, respectively. The results demonstrate trap-free electron and hole transport in as-cast P3HT:PDI-1 blends. Additionally, the effect of annealing on the electron contact and electron and hole-currents in P3HT:PDI-1 blends are discussed.

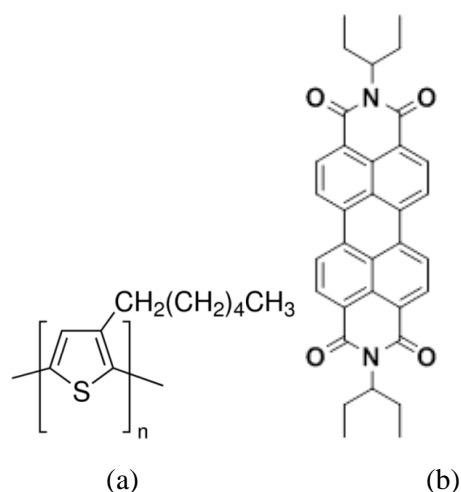


Figure 3.2. Molecular structure of regioregular poly(3-hexylthiophene) rr-P3HT donor and commercial perylene-3,4,9,10-perylene tetracarboxylic acid diimides (PDI-1).

### 3.2. Morphology of P3HT:PDI-1 blends

Planar PDI molecules show strong aggregation due to the strong  $\pi - \pi$  stacking of the material in the film. According to Singh et al. the size of the aggregates increases with increasing annealing temperature [8]. Our films of P3HT donor material blended with PDI-1 acceptor material show a highly crystalline morphology and the ribbon like crystals in the film are attributed to the PDI aggregates in the blends [8]. In the next chapter, it will be shown that as-cast solar cells of P3HT:PDI-1 show a very poor photocurrent, which prominently increases upon annealing of the devices. In literature, the morphology of PDI materials and, in particular, commercial PDI-1 and its blend with P3HT, is extensively studied [2,5,6]. It was shown by scanning electron microscopy that for a higher (1:3 ratio P3HT:PDI-1) ratio of PDI-1 in P3HT:PDI-1 blends, PDI-1 crystals are embedded in a P3HT matrix (Scanning electron microscopy) [6]. In the case of lower PDI-1 blend ratio (3:1 ratio P3HT:PDI-1) PDI-1 crystals have a tendency to stick out of the film, even up to a height of 500 nm [6]. Here a brief study is conducted with atomic force microscopy (AFM) on as-cast and annealed P3HT:PDI-1 films at 120<sup>0</sup>C, which are spin casted from either chloroform or chlorobenzene solutions.

Figure 3.3 shows the AFM height images of P3HT:PDI-1 films. Figure 3.3a shows the as-cast P3HT:PDI-1 films spin coated from chloroform and it is observed that in as-cast P3HT:PDI-1 films no large and separated PDI-1 domains are formed. Zooming in on the AFM images (Figure 3.3a1, 3.3a2 and 3.3a3) even reveal a nano-scale morphology.

However, upon annealing these films at 120<sup>0</sup>C for 10 min. separated PDI-1 domains close to a micron size (~600 to 1100 nm) are formed (Figure 3.3b). When P3HT:PDI-1 films are spin coated from higher boiling-point solvents like chlorobenzene, the crystalline structure appears even in the pristine films due to the slower evaporation of the solution (Figure 3.3c). In order to show if the presence of P3HT affects the formation of PDI-1 crystals, as a reference also the pristine PDI-1 material is spin coated from chloroform solution and the corresponding AFM image is shown in Figure 3.3d. We observe that the film of pristine PDI-1 shows a completely different morphology than its blends with P3HT. In the pristine PDI-1 film, the domains are around 2 times larger than in P3HT:PDI-1 films and are more like clusters. This shows that the presence of P3HT actually helps to prevent big and separated cluster like domains in the as-cast films of P3HT:PDI-1 blends. As a next step the transport of electrons and holes in P3HT:PDI-1 blends from chloroform solution, before and after annealing, will be evaluated.

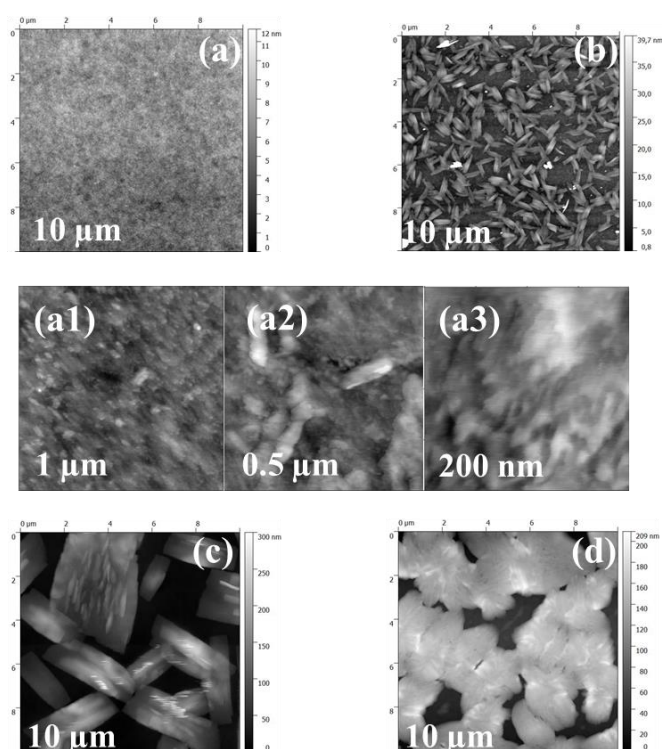


Figure 3.3. Atomic force microscopy (AFM) height images of (1:1) ratio P3HT:PDI-1 pristine film (a) in chloroform, (a1), (a2) and (a3) are the closer images of the same film at indicated different scales. (b) is the annealed image of P3HT:PDI-1 film at 120<sup>0</sup>C 10 min. spin casted from chloroform solution. (c) is the pristine film of P3HT:PDI-1 spin casted from chlorobenzene solution. (d) is the pristine PDI-1 film spin casted from chloroform solution.

### 3.3. Electron transport

In Figure 3.4a the measured electron currents of an as-cast device of a P3HT:PDI-1 blend in a 1:1 wt. ratio with a thickness of 120 nm are shown. The electron current shows an asymmetric behavior in forward and reverse bias. Surprisingly, the current in reverse bias, where electrons are injected from the Al bottom electrode, is higher than in forward bias, where electrons are injected from the Ba/Al top electrode and is supposed to be a better injecting contact. The lower current in forward bias demonstrates the existence of a small injection barrier at the top electrode. As a result the forward current is slightly injection limited, meaning that bulk charge transport properties cannot be directly obtained from the  $J$ - $V$  characteristics. Therefore, the higher current in the reverse bias is considered to examine the electron transport. The reverse-bias current shows a quadratic dependence on voltage at moderate electric fields, which is characteristic for a space-charge-limited current that is described by the Mott-Gurney law according to [17]

$$J = \frac{9}{8} \epsilon_0 \epsilon_r \mu \frac{V - V_{bi}^2}{L^3} \quad 3.1$$

To verify if the electron current is indeed space-charge limited we also investigated the thickness dependence of the electron current. Figure 3.4b shows the fits of the electron-current at two different layer thicknesses with the Mott-Gurney equation. The currents indeed show a  $L^{-3}$  dependence on thickness and are thus well-described by Eq. 3.1. The zero field electron mobility in the PDI-1 phase of the P3HT:PDI-1 (1:1) blend is found to be  $4.5 \times 10^{-11} \text{ m}^2/\text{Vs}$ . The electron mobility in PDI-1 is prominently lower than in as-cast P3HT:PCBM blends, for which the mobility for electrons through PCBM is around  $1 \times 10^{-8} \text{ m}^2/\text{Vs}$  [18]. It has been shown that in as-cast devices of P3HT:PCBM, the transport is strongly unbalanced and dominated by electrons. However, upon annealing of the devices above  $60^\circ\text{C}$  the hole mobility increases by three orders of magnitude (from  $10^{-11} \text{ m}^2/\text{Vs}$  to  $10^{-8} \text{ m}^2/\text{Vs}$ ), whereas the electron mobility increases to  $1 \times 10^{-7} \text{ m}^2/\text{Vs}$  [18].

In Figure 3.5 drift-diffusion simulations of the temperature-dependent current of the as-cast electron-only device are shown. From the simulations using the extended Gaussian disorder model [19], the average intersite spacing ( $a$ ) is 1.80 nm and the energetic disorder parameter  $\sigma$  amounts to 0.1476 eV. From the transport measurements on PCBM, a much lower disorder parameter of 0.073 eV has been found, consistent with the higher electron mobility in PCBM [20]. The strong energetic disorder in as-cast P3HT:PDI-1 electron-only devices leads to a very low electron mobility, which is expected to negatively impact the efficiencies of P3HT:PDI-1 solar cells, which will be discussed in the following chapter.

In literature, electron transport in P3HT:PDI-1 blends has been studied before, both in electron-only diodes [5] and in field effect transistors (FETs) [6]. In these studies, electron mobilities in P3HT:PDI-1 blends are found to be  $1.05 \times 10^{-11} \text{ m}^2/\text{Vs}$  for electron-only diodes and  $6 \times 10^{-7} \text{ m}^2/\text{Vs}$  for FETs. Furthermore, the effect of a chloronaphthalene (CN) additive on the electron mobility is also studied. It was found that the CN additive positively affects the electron mobility and it increased to  $3.45 \times 10^{-11} \text{ m}^2/\text{Vs}$  for 75 % CN [5]. In the latter case, the electron mobility is measured for a device annealed at  $120^\circ\text{C}$  for 20 min. The electron mobility reported from FET measurements is substantially higher. In an FET, in-plane electron transport at the dielectric-semiconductor interface is measured, whereas in solar cells vertical transport through the bulk is relevant. In addition the carrier density in a FET is typically 2-3 orders of magnitude higher than in a solar cell. Therefore, the FET mobility can be vastly different from the mobility extracted from electron-only diodes [21]. Commercial PDI-1 has also been studied by Sharenko et al. in a blend with a narrow band gap small molecule donor material and the electron mobility from SCLC measurements was calculated to be  $1 \times 10^{-8} \text{ m}^2/\text{Vs}$  [7]. This shows the high importance of an appropriate donor combination with PDI materials for better morphology and higher electron mobility.

### 3.4. Hole transport

The hole current of an as-cast P3HT:PDI-1 blend is measured using a hole-only device with a thickness of 200 nm, as shown in Figure 3.6a. The hole current shows a quadratic dependence on voltage, as is expected for space-charge limited currents (Eq. 3.1). Furthermore, also the thickness dependence is consistent with the Mott-Gurney Law, as shown in Figure 3.6b where the hole currents for two different layer thicknesses (140 nm and 200 nm) are described according to Eq. 3.1. The zero field hole mobility is calculated to be  $7.5 \times 10^{-10} \text{ m}^2/\text{Vs}$ . The temperature dependence of the current of the as-cast hole-only device is measured and simulated with a drift-diffusion model, as shown in Figure 3.7. From the simulations, the average intersite spacing ( $a$ ) is determined to be 1.6 nm and the disorder parameter  $\sigma$  is 0.131 eV. In as-cast P3HT:PCBM blends, the hole mobility only amounts to  $4 \times 10^{-12} \text{ m}^2/\text{Vs}$ , which is considerably lower than we find here in the P3HT-PDI-1 blends. However, upon annealing the hole mobility in P3HT:PCBM blends increases more than three orders of magnitude, reaches to  $10^{-8} \text{ m}^2/\text{Vs}$  [18]. In the literature, the P3HT mobility in as-cast P3HT:PDI-1 blends is found as  $6.31 \times 10^{-9} \text{ m}^2/\text{Vs}$  from SCLC

measurements and in the same study it is shown that CN additive decreases the hole mobility in P3HT:PDI-1 blends [5]. An important question is now whether also in P3HT:PDI-1 blends the hole mobility strongly increases upon annealing, as observed for P3HT:PCBM blends.

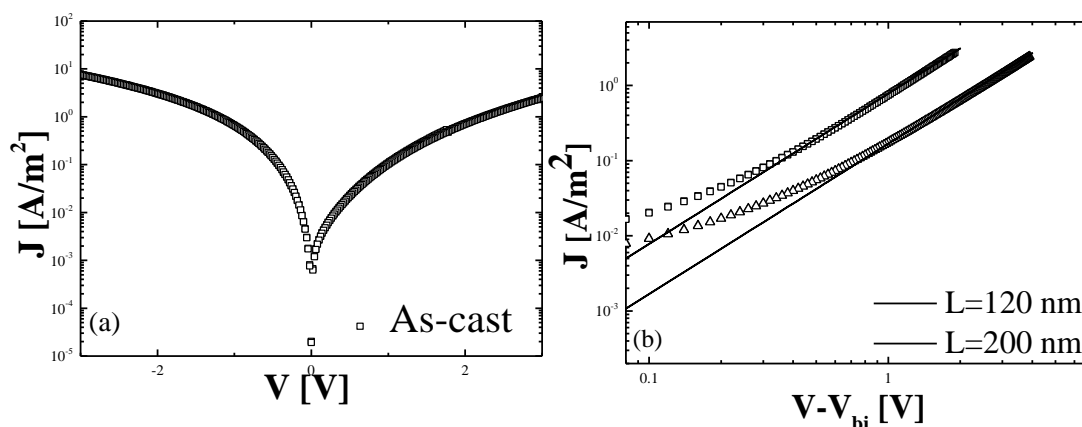


Figure 3.4. The current-voltage ( $J$ - $V$ ) characteristics of (1:1) ratio P3HT:PDI-1 as-cast electron-only devices; (a)  $J$ - $V$  characteristic for  $L=120\text{nm}$  (b) SCLC fit (Eq. 3.1, solid lines) of the reverse  $J$ - $V$  characteristics (symbols) at two different thicknesses.

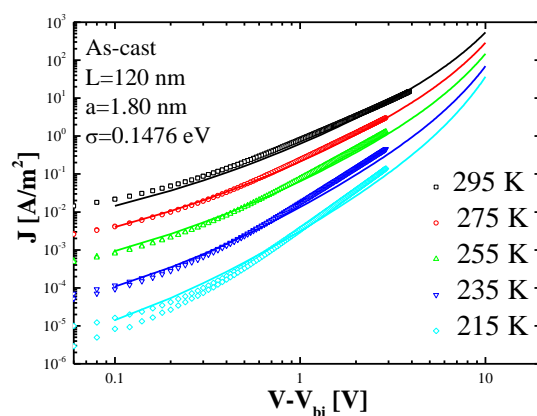


Figure 3.5. Drift-diffusion simulation of the  $J$ - $V$  characteristics of as-cast P3HT:PDI electron-only devices in (1:1) ratio. Symbols are the experimental  $J$ - $V$  characteristics at indicated temperatures and solid lines are fits to the experimental data. The simulation parameters  $a$  and  $\sigma$  are indicated in the graph.

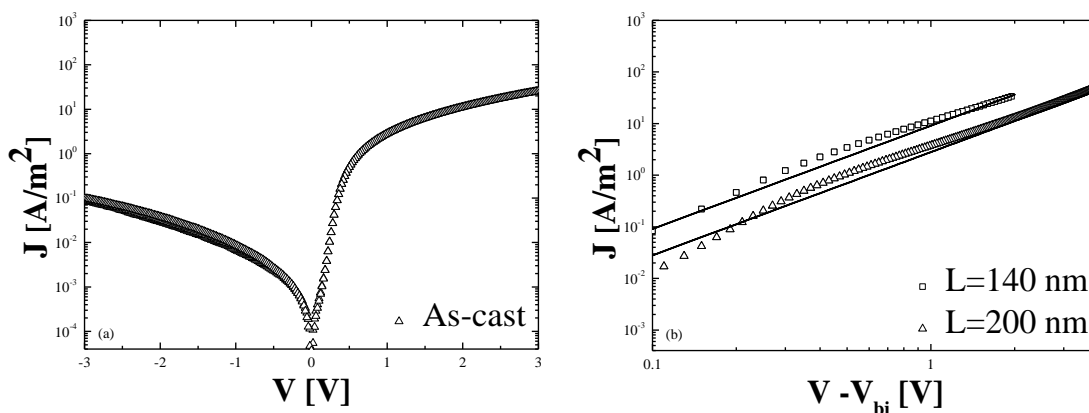


Figure 3.6. The current-voltage ( $J$ - $V$ ) characteristics of (1:1) ratio P3HT:PDI as-cast hole-only devices; (a)  $J$ - $V$  characteristic for  $L=200$  nm (b) SCLC fit (Eq. 3.1, solid lines) of the  $J$ - $V$  characteristics (symbols) at two different thicknesses of 140 nm and 200 nm.

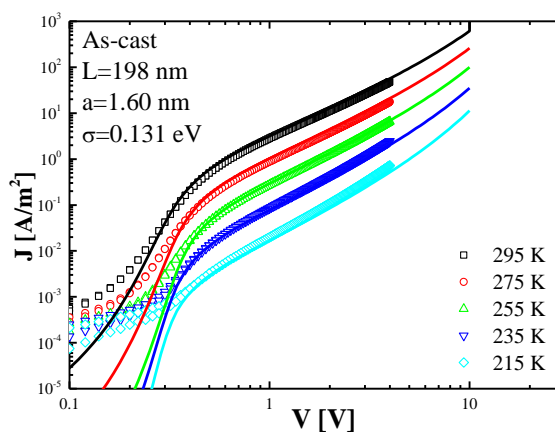


Figure 3.7. Drift-diffusion simulation of the  $J$ - $V$  characteristics of as-cast P3HT:PDI hole-only devices in (1:1) ratio. Symbols are the experimental  $J$ - $V$  characteristics at indicated temperatures and solid lines are fits to the experimental data. The simulation parameters  $a$  and  $\sigma$  are also indicated in the graph.

### 3.5. The effect of annealing on electron and hole current

In Figure 3.8a and 3.8b the  $J$ - $V$  characteristics of electron and hole-only devices as previously discussed in this chapter (Sections 3.3 and 3.4) after thermal annealing ( $120^{\circ}\text{C}$

for 10 min.) are shown. As can be seen from Figure 3.8a, the electron current continues to exhibit asymmetric behavior upon annealing. However, the current increases in forward bias and decreases in reverse bias. As shown in Section 3.3 the electron current before annealing was injection limited. An increase of the injection limited current indicates that either the contact barrier or the bulk charge transport of the PDI-1 has been improved. The decrease of the current in reverse bias, which was space-charge limited before annealing, shows that annealing has deteriorated the injection properties of the Al contact. To verify if the highest current (forward bias) is still space-charge limited we first observe that the forward  $J$ - $V$  characteristics after annealing are not quadratic with voltage. Furthermore, by analyzing two different thicknesses of annealed electron-currents we observe that the thickness scaling of  $L^{-3}$  according to SCLC is not fulfilled. This result shows that the electron current after annealing is clearly not space-charge limited, but rather injection limited and therefore the electron mobility cannot be extracted directly from  $J$ - $V$  characteristics of the annealed electron-only device. As a next step, in Figure 3.8b, the as-cast and annealed (120°C 10 min.) hole-only device is seen. The hole current in forward bias, that was space-charge limited before annealing, does not show a significant difference between as-cast and annealed device. As a result we can conclude that the hole mobility in P3HT:PDI-1 blend is not enhanced by annealing, in contrast to the observation for P3HT:PCBM blends. Apparently, the P3HT morphology in the blend is already fixed by the presence of PDI-1 directly after casting.

### 3.6. Conclusions

The charge transport in P3HT:PDI-1 blends is investigated with electron- and hole-only devices. From the electron- and hole-only devices, the calculated zero-field electron- and hole mobilities in the blend are  $4.5 \times 10^{-11} \text{ m}^2/\text{Vs}$  and  $7.5 \times 10^{-10} \text{ m}^2/\text{Vs}$ , respectively. These mobilities are prominently lower than the electron and hole mobilities measured in annealed P3HT:PCBM single-carrier devices. The electron transport appears to be subject to a high degree of energetic disorder. The measured mobilities show that for as-cast 1:1 P3HT-PDI-1 blends the transport is governed by holes. Annealing of the electron-only devices enhances the crystallinity of PDI-1 but does not increase the electron current due to the occurrence of a contact barrier. As a result the electron mobility cannot be determined from the  $J$ - $V$  characteristics since the currents are not space-charge limited but are limited by injection. The hole current does not show a prominent change upon annealing.



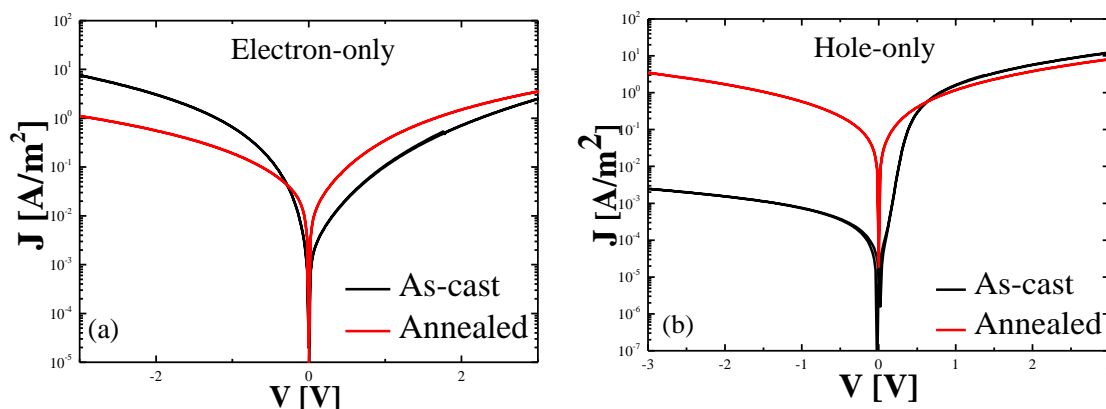


Figure 3.8. (a) The current-voltage characteristics of a (1:1) ratio P3HT:PDI-1 electron-only device before (black line) and after annealing (red line) at 120<sup>0</sup>C 10 min. The thickness of the device is L=120nm. (b) The current-voltage characteristics of a (1:1) ratio P3HT:PDI-1 hole-only device before (black line) and after annealing (red line) at 120<sup>0</sup>C 10 min. The device thickness is 200 nm.

### 3.7. Experimental

In this work, commercial PDI derivative (PDI-1) with shortly branched alkyl chains in the imide position has been used together with regioregular poly(3-hexylthiophene) rr-P3HT donor material. rr-P3HT donor and commercial perylene-3,4,9,10-perylene tetracarboxylic acid diimide (PDI) acceptor were blended in a 1:1 ratio and spin coated from chloroform solution at 1000 rpm. The concentration of the solutions is 6.6 mg/ml. Hole-only devices were fabricated on glass substrate with indium tin oxide (ITO). ITO substrates were cleaned with detergent agent and ultrasonicated in acetone and isopropanol, and cleaning finished with UV-ozone treatment. In electron-only devices glass substrates were used and cleaned in the same way of ITO substrates. The bottom contact is Al (30 nm) and the top contact is LiF (1nm)/Al (100nm) in electron-only devices. In hole-only devices, the blend is sandwiched between ITO/PEDOT:PSS (poly(3,4-ethylenedioxythiophene)/poly(styrenesulfonate) anode and 100 nm gold (Au) cathode. Devices are measured under a nitrogen atmosphere Keithley 2400 source meter. Devices are annealed at 120<sup>0</sup>C 10 min. in glovebox. The annealing temperature is chosen according

to the work done in the literature [2]. Nanoscope Dimension 3100 from Bruker is used for the atomic force microscopy (AFM) study.

### 3.8. References

- [1] J. J. Dittmer, E. A. Marseglia, R. H. Friend, *Adv. Mater.* **12**, 1270 (2000).
- [2] V. Kamm, G. Battaglin, I. A. Howard, W. Pisula, A. Mavrinskiy, C. Li, K. Müllen, and F. Laquai, *Adv. Mater.* **1**, 297 (2011).
- [3] P. E. Keivanidis, I. A. Howard, R. H. Friend, *Adv. Funct. Mater.* **18**, 3189 (2008).
- [4] P. E. Keivanidis, V. Kamm, W. Zhang, G. Floudas, F. Laquai, I. McCulloch, D. D. C. Bradley, and J. Nelson, *Adv. Funct. Mater.* **22**, 2318 (2012).
- [5] M. Li, L. Wang, J. Liu, K. Zhou, X. Yu, R. Xing, Y. Gengab, and Y. Han, *Phys. Chem. Chem. Phys.* **16**, 4528 (2014).
- [6] S. R. Puniredd, A. Kiersnowski, G. Battaglin, W. Zaja, W. Zajaczkowski, W.W. H. Wong, N. Kirby, K. Müllen, and W. Pisula, *J. Mater. Chem. C* **1**, 2433 (2013).
- [7] A. Sharenko, C. M. Proctor, T. S. van der Poll, Z. B. Henson, T.-Q. Nguyen, and G. C. Bazan, *Adv. Mater.* **25**, 4403 (2013).
- [8] R. Singh, E. Giussani, M. M. Mroz, F. Di Fonzo, D. Fazzi, J. Cabanillas-González, L. Oldridge, N. Vaenas, A. G. Kontos, P. Falaras, A. C. Grimsdale, J. Jacob, K. Müllen, P. E. Keivanidis, *Org. Electron.* **15**, 1347 (2014).
- [9] G. Sauvé and R. Fernando, *J. Phys. Chem. Lett.* **6**, 3770 (2015).
- [10] A. Anctil, C. W. Babbitt, R. P. Raffaele, and B. J. Landi, *Environ. Sci. Technol.* **45**, 2353 (2011).
- [11] D. Meng, D. Sun, C. Zhong, T. Liu, B. Fan, L. Huo, Y. Li, W. Jiang, H. Choi, T. Kim, J. Y. Kim, Y. Sun, Z. Wang, and A. J. Heeger, *J. Am. Chem. Soc.* **138**, 375 (2016).
- [12] R. S. A. S. Holliday, A. Wadsworth, D. Baran, S. A. Yousaf, C. B. Nielsen, C.H. Tan, S. D. Dimitrov, Z. Shang, N. Gasparini, M. Alamoudi, F. Laquai, C. J. Brabec, A. Salleo, J. R. Durrant, and I. McCulloch, *Nat. Commun.* **7**, 898 (2016).
- [13] C. Li and H. Wonneberger, *Adv. Mater.* **24**, 613 (2012).
- [14] P. W. M. Blom, M. J. M. de Jong, and J. J. M. Vlegaar, *Appl. Phys. Lett.* **68**, 3308 (1996).
- [15] H. T. Nicolai, G. A. H. Wetzelaer, B. de Boer, C. Campbell, C. Risko, J. L. Brédas, and P. W. M. Blom, *Nat. Mater.* **11**, 882 (2012).

- [16] D. M. De Leeuw, M. M. J. Simenon, A. R. Brown, and R. E. F. Einerhand, *Synth. Met.* **87**, 53 (1997).
- [17] N. F. Mott and R. W. Gurney, *Electronic Processes in Ionic Crystals* (Oxford University Press, London, 1940).
- [18] V. D. Mihailetschi, H. Xie, B. de Boer, L. J. A. Koster, and P. W. M. Blom, *Adv. Func. Mater.* **16**, 699 (2006).
- [19] W. F. Pasveer, J. Cottaar, C. Tanase, R. Coehoorn, P. A. Bobbert, P.W. M. Blom, D. M. de Leeuw, and M. A. J. Michels, *Phys. Rev. Lett.* **94**, 206601 (2005).
- [20] D. L. Cheung and A. Troisi, *J. Phys. Chem. C* **114**, 20479 (2010).
- [21] F. Laquai , R. Mauer, and P. W. M. Blom, *Macromol. Rapid Commun.* **36**, 1001 (2015).

#### **4. The effect of annealing on open circuit voltage of P3HT:PDI solar cells**

Solar cells based on blends of regioregular poly(3-hexylthiophene) (rr-P3HT) as donor and commercial perylene-3,4,9,10-perylene tetracarboxylic acid diimides (PDI-1) as acceptor are investigated. As-cast devices show very low photocurrent and the photocurrent increases upon annealing at 120<sup>0</sup>C for 10 min. However, upon annealing there is a prominent loss in open-circuit voltage. The decrease in open-circuit voltage is consistent with the formation of an electron injection barrier upon annealing. The presence of an contact barrier is confirmed by the dependence of the open circuit voltage on light intensity. The observed slope of  $kT/2q$  at high light intensities is a fingerprint for solar cells with an injected-limited contact.

#### **4.1. Introduction**

Conjugated polymers as donor and fullerene derivatives as acceptor are the main materials in the conventional design of the bulk heterojunction solar cells [1,2]. In recent years, research has been accelerated for the new acceptor materials in order to replace fullerene derivatives [3-7]. One of the main reasons is the low absorption of the fullerene derivatives in the visible part of the spectrum that limits the maximum achievable efficiency in solar cells. Perylene diimide derivatives (PDIs) offer a high absorption in the visible part of the spectrum and their chemical structure can be tuned at various functional positions. Therefore, varying the electronic, optical and physical properties in PDIs by functionalizing their chemical structure is considered as an important advantage [8].

PDIs have already a quite broad history for solar cells: the first organic solar cell that was utilized by Tang in 1986 had a perylene tetracarboxylic derivative as the acceptor, together with copper phthalocyanine as donor and the solar cell utilized 1 % efficiency [9]. The perylene derivative he used was not soluble in common organic solvents and was deposited by evaporation. Later on perylene derivatives with good solubility were developed and utilized in bilayer and bulk heterojunction devices [8]. In more recent work Howard et al. studied the charge generation and recombination in poly(9,9-dioctylfluorene-alt-benzothiadiazole) (F8BT):perylene solar cells spin coated from chloroform and toluene with femtosecond transient-absorption experiments [10]. They discussed two loss processes in solar cells with perylene acceptors; firstly, when perylene is finely dispersed in a conjugated polymer donor, fast bimolecular recombination limits the device performance [10]. When the morphology of the blend is coarser, excitons are relaxing into stabilized intermolecular states rather than contributing to the charge transfer [10]. Moreover, PDIs tend to create micron sized crystals, which then hinder solar cell performance by inefficient exciton quenching [8]. Therefore, in order to utilize PDIs in bulk-heterojunction solar cells it is crucial to decrease or control their aggregation [11]. As an example, Kamm et al. showed that ortho- substitution in PDIs actually decreases aggregation, leading to an enhancement of the device performance of perylene based organic solar cells [12].

In this chapter, bulk heterojunction (BHJ) solar cells of regioregular poly(3-hexylthiophene) rr-P3HT as donor material and commercial PDI-1 as acceptor are studied. The solutions consisted of a 1:1 donor/acceptor ratio and were spin casted from chloroform. Solar cells of P3HT:PDI-1 show very low photocurrent in as-cast devices and gain photocurrent upon annealing of the devices, which is however accompanied by a loss of open circuit voltage ( $V_{oc}$ ). Such a loss of  $V_{oc}$  is consistent with the occurrence of an electron

injection barrier upon annealing, as observed in Chapter 3. As shown in Chapter 2 the presence of an electron injection barrier also affects the dependence of  $V_{oc}$  on light intensity. Therefore, the  $V_{oc}$ -light intensity dependence is investigated before and after annealing of the same devices. The reduced dependence of  $V_{oc}$  upon annealing is correlated with the presence of an injection barrier.

#### **4.2. Current-voltage characteristics of P3HT:PDI-1 solar cells**

Figure 4.1 shows the current-voltage characteristics of a P3HT:PDI-1 solar cell under illumination and the solar cell parameters are listed in Table 4.1. It appears that as-cast P3HT:PDI-1 solar cells suffer from a very low fill factor and low device current, leading to low device efficiency. Compared to P3HT:fullerene solar cells (0.6 V) the as-cast P3HT:PDI-1 solar cells studied here have a slightly lower  $V_{oc}$  (0.56 V), although PDI-1 has a similar LUMO energy ( $\sim$ 3.8 eV) as compared to the fullerenes. The very low device current typically observed in as-cast P3HT:PDI-1 solar cells is attributed to fast bimolecular recombination [8]. Upon annealing the P3HT:PDI-1 solar cells (120<sup>0</sup>C 10 min.) the device current prominently increases. The increase of the photocurrent is accompanied by an increase of the external quantum efficiency (EQE), as shown in Figure 4.2. Before annealing the device shows a very low EQE while upon annealing EQE significantly increases. A possible reason for the increased EQE after annealing could also be an increase of the optical absorption. In Figure 4.3 the absorption spectrum of PDI-1, P3HT and P3HT:PDI-1 blends in (1:1) ratio, before and after annealing at 120<sup>0</sup>C 10 min. is shown. In as-cast P3HT:PDI-1 blend there are three peaks at 200 nm, 490nm and 530 nm. Compared to absorption spectrum of the pristine materials (either PDI-1 or P3HT) the peak at shorter wavelengths (<300 nm) in the blend is attributed to the PDI-1 material. Between 450 nm and 600 nm there is a strong overlap in absorption between P3HT and PDI-1. Comparing as-cast and annealed P3HT:PDI-1 blends, the main absorption peak is slightly broadened on the short wavelength side (400 nm - 500 nm). However, this slight change in absorption cannot be responsible for the strong increase in the photocurrent and EQE upon annealing. The increase of the photocurrent also leads to an increase of the power conversion efficiency upon annealing. However, the efficiency increase is strongly limited by a huge loss in  $V_{oc}$  of around 190 mV upon annealing.

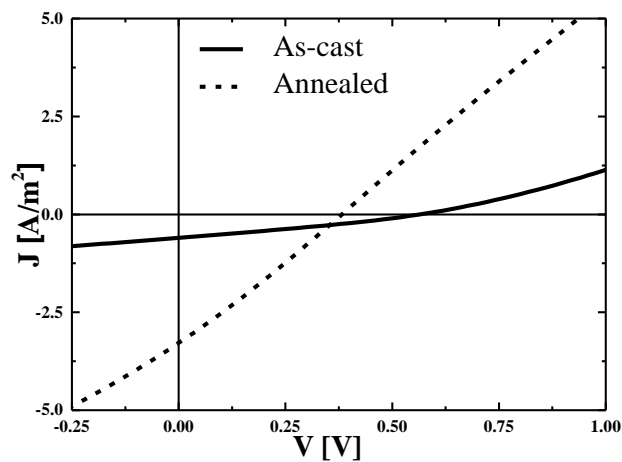


Figure 4.1. Measured  $J$ - $V$  characteristics under illumination of an as-cast and subsequently annealed ( $120^{\circ}\text{C}$  10 min.) P3HT:PDI-1 solar cell with a thickness of 198 nm.

Table 4.1. Solar cell parameters of current-voltage characteristics in Figure 4.1.

Device	$V_{oc}$ [V]	$J_{sc}$ [ $\text{A}/\text{m}^2$ ]	FF [%]	PCE [%]
(1:1)As-cast	0.56	0.6	29	0.016
(1:1)Annealed	0.38	3.3	24	0.050

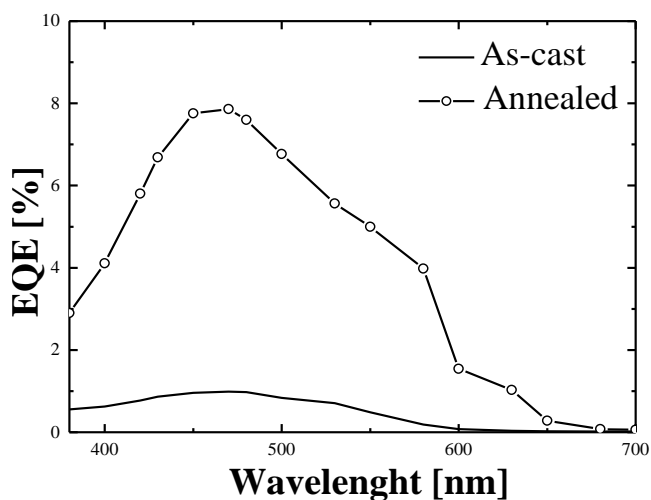


Figure 4.2. External quantum efficiency of (1:1) wt. ratio P3HT:PDI-1 solar cells before and after annealing at  $120^{\circ}\text{C}$  10 min.



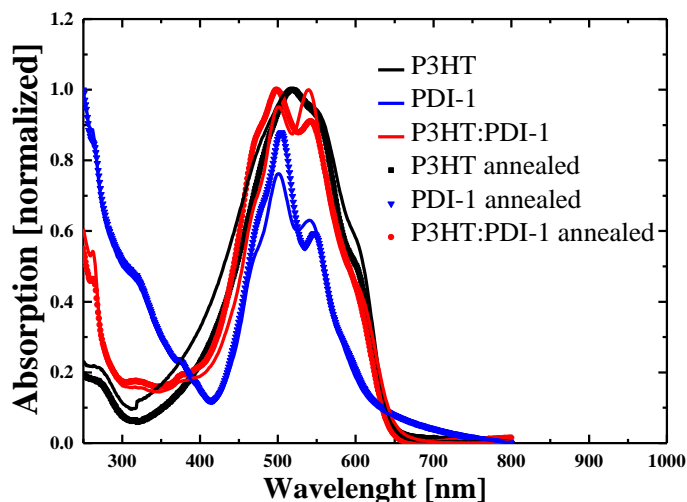


Figure 4.3. Normalized absorption spectrum of PDI-1, P3HT and P3HT:PDI-1 in (1:1) blend ratio, before and after annealing at 120°C 10 min. In all cases measurements are done on a glass substrate and corrected for the substrate absorption.

To study the  $V_{oc}$  loss as a first step we look at the dark currents (Figure 4.4.) of solar cells before and after annealing. At voltages lower than the built-in voltage ( $V_{bi}$ ) the electric field in the device is opposite to the current, which is driven by diffusion. This diffusion-limited current is characterized by an exponential dependence on voltage. For voltages larger than  $V_{bi}$  the current becomes dominated by drift, resulting in the quadratic space-charge limited current. The transition voltage from the exponential to the quadratic regime then corresponds to  $V_{bi}$  [13]. As can be seen from Figure 4.4, after annealing the dark current  $J$ - $V$  is shifted to the left (lower voltage) by 0.2 V, meaning that after annealing  $V_{bi}$  has decreased by 0.2 V. This is consistent with the decrease of 190 mV of the open-circuit voltage under illumination. Typically,  $V_{bi}$  has its maximum value in case of two ohmic contacts, but decreases when an injection barrier exists at one (or both) of the contacts. The simultaneous decrease of  $V_{bi}$  and  $V_{oc}$  can therefore be explained by the formation of an injection barrier during annealing. This injection barrier could in principle be either on the hole contact, electron contact or both. However, from the charge transport studies presented in Chapter 3 the occurrence of an electron injection barrier upon annealing was already established. To further verify the presence of an injection barrier the dependence of  $V_{oc}$ —on light intensity is investigated.

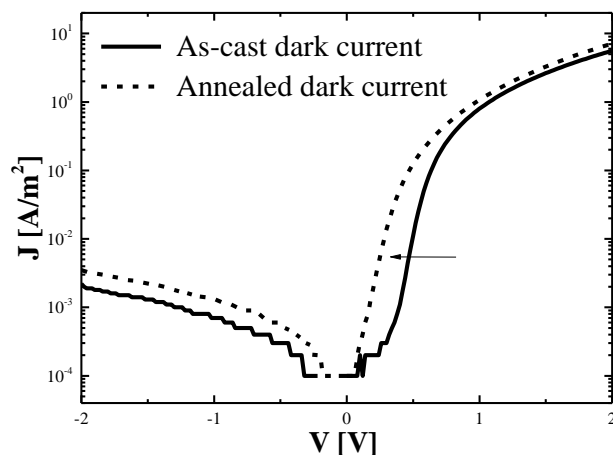


Figure 4.4. Experimental  $J$ - $V$  characteristics in the dark of as-cast and annealed ( $120^{\circ}\text{C}$  10 min.) P3HT:PDI-1 solar cell with a thickness of 198 nm.

### 4.3. Open circuit voltage-light intensity measurements in P3HT:PDI-1 solar cells

Figure 4.5 shows the  $V_{oc}$ -light intensity dependence of the as-cast and annealed devices that were shown in Figure 4.1. The as-cast device has the slope of  $1.07 kT/q$ . This results shows that both contacts are ohmic and that the dominant recombination mechanism is bimolecular recombination in P3HT:PDI-1 solar cells before annealing [14]. However, in the annealed device not only  $V_{oc}$  is reduced, but also the slope of the  $V_{oc}$ -light intensity dependence is decreased at high light intensities and approaches to  $kT/q$  [15]. This confirms that upon annealing in P3HT:PDI-1 devices a single injection barrier is formed that is responsible for the decrease in  $V_{oc}$ .

Figure 4.6 shows the  $V_{oc}$  of P3HT:PDI-1 solar cells with different annealing times (2 min., 10 min. and 20 min.) at  $120^{\circ}\text{C}$ . It is seen that the prominent decrease of the  $V_{oc}$  is already present at short annealing times (2 min.) with increasing annealing time  $V_{oc}$  continues to decrease slowly. At all indicated annealing times the slope of  $V_{oc}$  versus light intensity is equal to  $kT/2q$ , pointing out the presence of an injection barrier upon annealing.

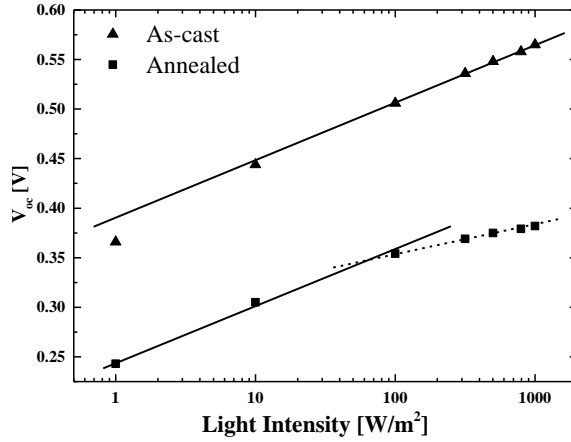


Figure 4.5.  $V_{oc}$  versus light intensity dependence for as-cast and annealed P3HT:PDI-1 solar cells. The filled triangles correspond to  $V_{oc}$  values of the as-cast device and filled squares correspond to the annealed device. Solid lines correspond to a slope of  $kT/q$  and the dotted line corresponds to slope of  $kT/2q$ .

As shown in Section 3.2 the annealing process strongly affects the morphology of the P3HT:PDI-1 films. Crystallization of PDI-1 will also lead to a lowering of the band gap (HOMO-LUMO separation) and as such the effective band gap of a P3HT:PDI-1 solar cell is decreased, leading to a reduction of  $V_{oc}$ . A similar effect was observed for polymer:fullerene solar cells upon annealing [16]. However, for P3HT-PDI-1 blends we do not observe a red-shift in EQE upon annealing. To investigate the effect of the effective band gap on  $V_{oc}$  and its light intensity dependence numerical simulations are carried out. In Figure 4.7 numerical simulations are shown for the case of solar cells with two different band gaps and ohmic contacts in a model system with 200 nm active layer thickness and equal electron-hole mobilities ( $\mu_e$  and  $\mu_h$ , respectively) in the order of  $10^{-11} \text{ m}^2/\text{Vs}$ . The generation (light intensity) is varied over four orders of magnitude ( $10^{28}$ - $10^{24} \text{ 1/m}^3\text{s}$ ) while all other parameters (mobility, thickness, temperature, dielectric constant) are kept the same. It is shown that in the case of a decrease in the band gap the  $V_{oc}$  indeed drops, but that the slope of  $V_{oc}$ -light intensity dependence is not affected. A slope of  $kT/q$  is observed over the full of generation range.

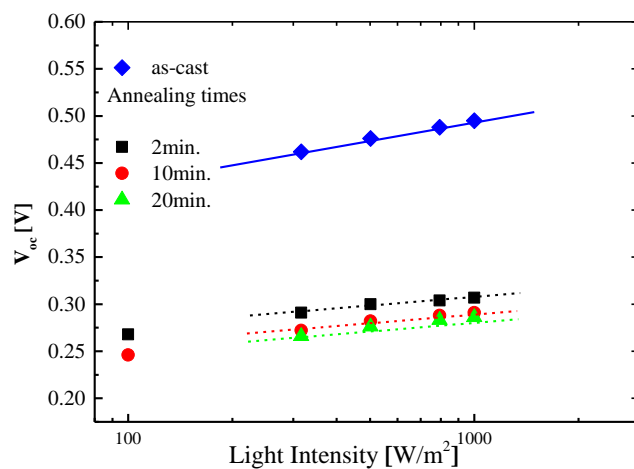


Figure 4.6. Effect of annealing times on the decrease of  $V_{oc}$  in (1:1) P3HT:PDI-1 solar cells. The solid line corresponds to a slope of  $kT/q$  and the dotted lines to a slope of  $kT/2q$ .

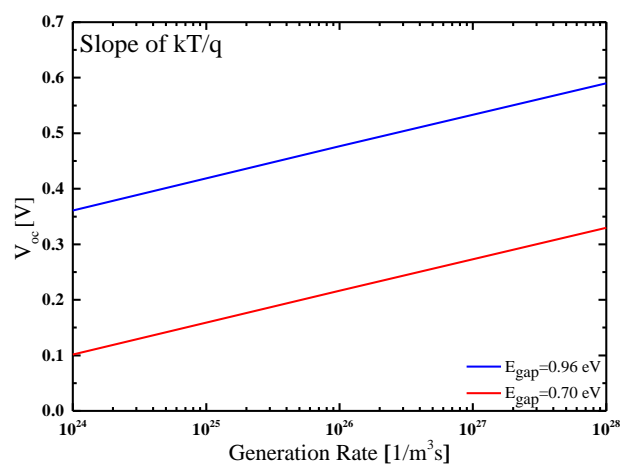


Figure 4.7. The slope of  $V_{oc}$ -light intensity dependence depicted, when  $E_{gap}=0.96$  eV and  $E_{gap}=0.70$ eV. Solid lines corresponds to slope of  $kT/q$ .

#### 4.4. Modelling of the photocurrent of P3HT:PDI-1 solar cells

The measured  $J$ - $V$  characteristic of an as-cast (1:1) ratio P3HT:PDI-1 solar cell under illumination is simulated and shown in Figure 4.7, together with the dark current of the same device. As input for the numerical simulations, the mobilities for electrons and holes

are experimentally determined from electron-only and hole-only devices (Chapter 3), respectively. The effective band gap ( $E_{gap}$ ) of the blend is estimated from the LUMO energy of the acceptor and the HOMO energy of the donor material. The relative dielectric constant ( $\epsilon_r$ ) is taken as 3. To calculate the dissociation probability  $P(T,E)$  of a bound electron-hole pair the Onsager-Braun model is used [17,18]. In this model the dissociation of the bound pair is characterized by two parameters, the initial separation distance  $a$  between the electron and hole and the decay rate (lifetime)  $k_f$  of the bound pair. From the numerical simulation of the  $J$ - $V$  characteristics of a P3HT:PDI-1 solar cell under illumination a charge separation distance ( $a$ ) of 0.87 nm is found, together with a decay rate ( $k_f$ ) of  $2 \times 10^4$  1/s. As a comparison, in P3HT:PCBM based solar cells the charge separation distance is reported as 1.8 nm, whereas  $k_f$  is also found to be  $2 \times 10^4$  1/s [19,20]. A smaller charge separation distance implies that the  $e$ - $h$  pair is tightly bound, and therefore the charge separation is difficult in P3HT:PDI-1 blends. A large decay rate (short lifetime) reduces the probability for dissociation. For the P3HT:PDI-1 the dissociation probability is calculated at  $V-V_0 = 0.1$  V as  $9.9 \times 10^{-2}$  from  $J_{ph}/(qG_{max}L)$ . This means that at  $V=0$ V (short-circuit) only 6.14 % of the photo-generated hole pairs are dissociated. This value is about 15 times lower as compared to P3HT:PCBM cells [21].

In Figure 4.8 it is also shown that the photocurrent has a strong dependence on (reverse) bias. With increasing electric field more and more of the strongly bound  $e$ - $h$  pairs are dissociated, leading to an increase of the current. As very high applied electric field all photogenerated  $e$ - $h$  pairs will be separated and the photocurrent will reach its maximum value  $qG_{max}L$ . From the simulation, a maximum generation rate in P3HT:PDI-1 blends of  $2 \times 10^{26}$  1/m<sup>3</sup>s is found. This low generation rate means that in spite of the higher absorption coefficient of PDI-1 as compared to PCBM less electron-hole pairs at the D-A interface are formed. The reason is most likely the formation of PDI-1 domains of which the size is much larger than the exciton diffusion length. Then, most of the excitons that are created in the PDI-1 will recombine before they reach the D-A interface where electron transfer occurs and a bound pair is formed. From the simulations on the as-cast P3HT:PDI-1 solar cell we can therefore conclude that the low photocurrent is the result of a low generation rate of bound pairs at the D-A interface, combined with a low dissociation probability of those pairs. Besides, low mobility leads to higher bimolecular recombination and decreased FF together with field dependent generation rate.

In order to simulate the P3HT-PDI-1 solar cell after annealing the decrease in  $V_{oc}$  gives us direct information on the magnitude of the electron injection barrier. However, a problem we encounter is that after annealing the electron currents in the electron-only devices are injection limited and not space-charge limited. As a result, we cannot determine the electron mobility after annealing. In order to estimate the electron mobility after annealing we have simulated the photocurrent of the annealed device, with the electron mobility as a fitting parameter, as shown in Figure 4.9. The injection barrier is estimated by comparing the  $V_{oc}$  in as-cast and annealed devices. The simulation of the as-cast device is taken as a starting point. In order to get the correct  $V_{oc}$  an injection barrier of 0.45 eV has to be added while all other parameters are kept same. However, it can be clearly seen that the observed increase in the photocurrent  $J_{ph}$  cannot be explained. We know from single-carrier measurements that the hole mobility does not change upon annealing. Therefore, the increase of the photocurrent cannot be explained by an increase of the hole mobility. As shown in Figure 4.9 it appears that a higher electron mobility leads to a higher photocurrent ( $J_{ph}$ ). In order to reach the level of the experimental photocurrent the electron mobility need to be increased to the order of  $1.5 \times 10^{-9} \text{ m}^2/\text{Vs}$ .

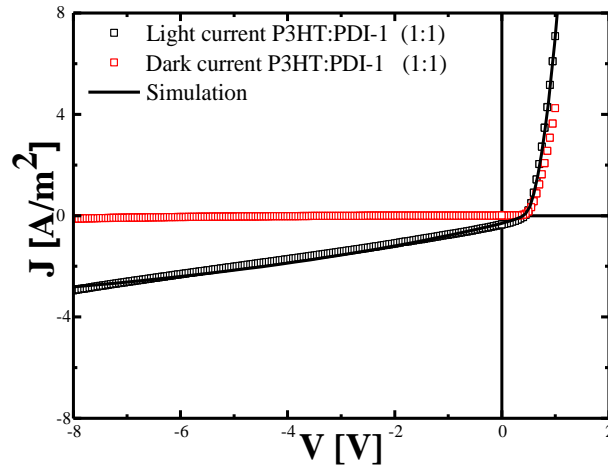


Figure 4.8. Numerical simulation of the (1:1) ratio of an as-cast P3HT:PDI-1 solar cell under illumination. The black symbols represent the experimental photocurrent, red symbols are the dark current and blue symbols are the annealed (120<sup>0</sup>C 10 min.) device. The black solid line is a fit to the experimental photocurrent, using the fit parameters  $a$  and  $k_F$  of 0.87 nm and  $2 \times 10^4 \text{ 1/s}$ , respectively.  $G_{max} = 2 \times 10^{26} \text{ 1/m}^3\text{s}$  from the simulation and the device thickness is 180 nm.

#### **4.5. Modeling of open circuit voltage-light intensity measurements in P3HT:PDI-1 solar cells**

As a final step numerical simulations are carried out to model the  $V_{oc}$ -light intensity measurements in P3HT:PDI-1 solar cells. The mobilities for electron and holes for the as-cast case are taken from single carrier devices, which have been discussed in Chapter 3. The  $V_{oc}$ -light intensity measurements in the annealed case can be used to calculate the injection barrier and the electron mobility of the annealed device. The hole mobility for the annealed case is again taken from the space-charge limited single carrier devices. In both cases (as-cast and annealed) the generation rates set to real device values, which are shown in Figure 4.1. The simulations are shown in Figure 4.10. The as-cast  $V_{oc}$ -light intensity measurements is simulated with no barriers and with mobilities as obtained from as-cast single carrier devices. In the annealed case, a contact barrier of 0.45 eV and an electron mobility of  $1.5 \times 10^{-9} m^2/Vs$  is used in order to simulate the  $V_{oc}$ -light intensity measurements. Similar to the simulation of the photocurrent of the annealed P3HT-PDI-1 solar cells (Section 4.4) and electron mobility of  $\sim 10^{-9} m^2/Vs$  is required to correctly describe the light-intensity dependence of the  $V_{oc}$ . With this enhanced electron mobility all the device characteristics of the annealed device are consistently explained.

#### **4.6. Analysis of P3HT:PDI-1 solar cells in 1:4 weight ratio**

In Chapter 3 electron and hole-only devices of P3HT:PDI-1 blends are studied before and after annealing. Before annealing, the electron and hole transport are strongly unbalanced. The electron mobility amounts to  $4.5 \times 10^{-11} m^2/Vs$ , whereas the hole mobility is equal to be  $7.5 \times 10^{-10} m^2/Vs$ . This strong imbalance in the transport leads to the build-up of space charges and is detrimental for solar cell performance. After annealing the electron mobility increases, but solar performance is hindered by a loss in  $V_{oc}$ . Another option to obtain a more balanced transport without the necessity to anneal the devices is to increase the amount of PDI-1 in the blend. For this purpose, we also investigate the device properties of P3HT-PDI-1 blend solar cells in a (1:4) wt. ratio. P3HT:PDI-1 solar cells and single carrier devices in (1:4) ratio are studied and compared to the results of the (1:1) ratio. In Figure 4.11a and 4.11b the electron and hole currents of as-cast devices are shown. Both the electron and hole currents exhibit a quadratic dependence on voltage, indicating that the current is space-charge limited, and can be described by the Mott-Gurney Eq. 3.1. The zero field mobilities are found as  $9 \times 10^{-10} m^2/Vs$  for electrons and  $1 \times 10^{-9} m^2/Vs$  for

holes. The electron mobility is prominently higher as compared to the (1:1) ratio, while the hole mobility in the P3HT phase is nearly equal to the (1:1) ratio and thus only weakly depends on the PDI-1 ratio. As a result the electron and hole transport is highly balanced in as-cast (1:4) ratio P3HT:PDI-1 blends.

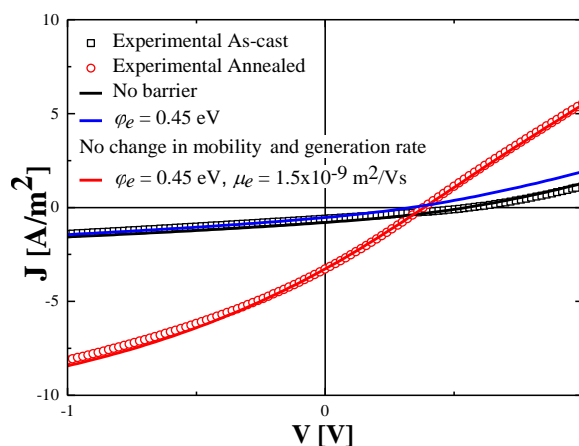


Figure 4.9. Black symbols are for the experimental as-cast current and red symbols are for the experimental annealed current (120<sup>0</sup>C 10 min.) of P3HT:PDI-1 solar cell. Solid lines are the numerical simulations. Black line is the numerical simulation of as-cast device with no barrier, the calculated zero-field electron- and hole mobilities from single carrier devices are  $4.5 \times 10^{-11} \text{ m}^2/\text{Vs}$  and  $7.5 \times 10^{-10} \text{ m}^2/\text{Vs}$  and  $G_{max} = 1 \times 10^{26} \text{ 1/m}^3\text{s}$ . Blue line shows that in order to compensate the decrease in  $V_{oc}$  in the annealed case 0.45 eV electron barrier ( $\phi_e$ ) is needed. However, numerical simulation of annealed case (red line) shows that the increase in photocurrent can be compensated with an increase of electron mobility to  $1.5 \times 10^{-9} \text{ m}^2/\text{Vs}$  (red solid line) and  $G_{max} = 4 \times 10^{26} \text{ 1/m}^3\text{s}$ .



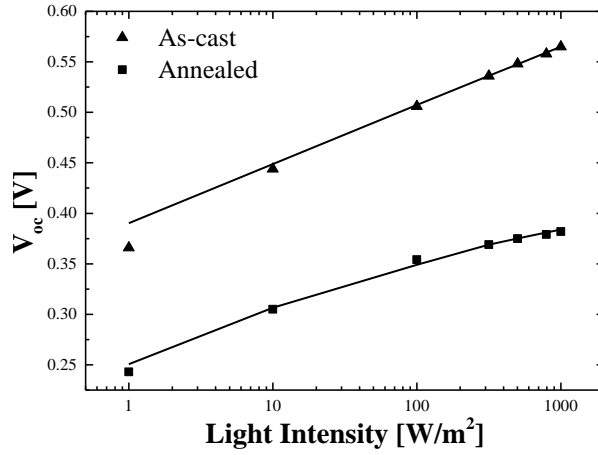


Figure 4.10.  $V_{oc}$ -versus light intensity dependence of as-cast and annealed P3HT:PDI-1 solar cells. The as-cast devices are simulated with two ohmic contacts whereas the annealed devices are simulated with a 0.45 eV electron contact barrier. The device thickness amounts to 198 nm.

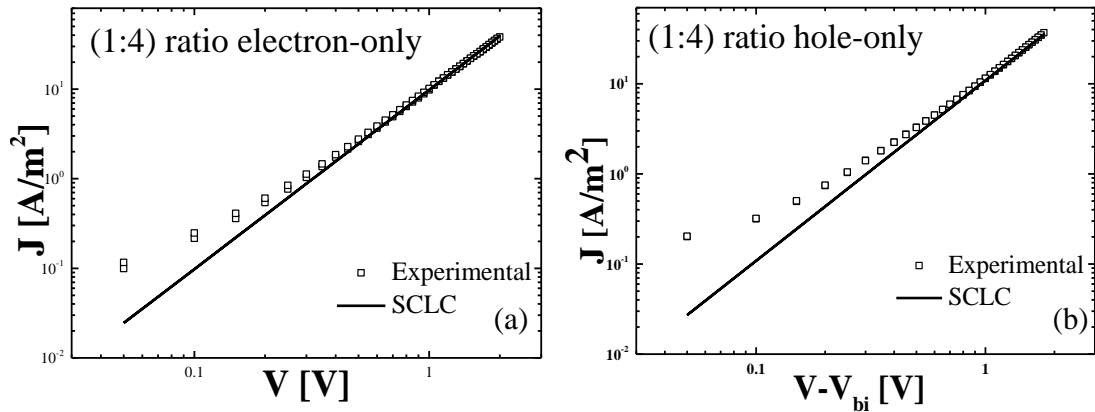


Figure 4.11. (a) Experimental electron current (symbols) and SCLC fit (line), (b) experimental hole current (symbols) and SCLC fit (line). Both devices have a thickness of 140 nm.

In Figure 4.12 as-cast and post-annealed (1:1) and (1:4) ratio solar cells are shown under illumination. The corresponding device parameters are shown in Table 4.2. In the as-cast devices, we observe that the  $V_{oc}$  is slightly higher (0.06 V difference) in the (1:4) ratio as compared to (1:1) ratio solar cell. Furthermore there is a 12 times increase in the  $J_{sc}$  in

(1:4) ratio as compared to (1:1) ratio, which can be correlated with the strongly increased electron mobility in the (1:4) ratio. Also for the (1:4) ratio a decrease of  $V_{oc}$  is observed. However, the decrease of 70 mV is far less as compared to decrease observed in the (1:1) ratio (190 mV). Similar to the (1:1) case also the photocurrent increases upon annealing, it nearly doubles, but with regard to the solar cell performance the current increase is neutralized by the decrease of open-circuit voltage. To further investigate the open-circuit voltage decrease we also annealed the devices before evaporation of the LiF/Al cathode. It appears that annealing leads to a similar decrease in  $V_{oc}$  both in the pre- and post-annealed case. With regard to the photocurrent increase in current is more prominent in the post-annealed devices. This result shows that post-annealing is the preferred treatment of the P3HT-PDI-1 solar cells in order to gain photocurrent.

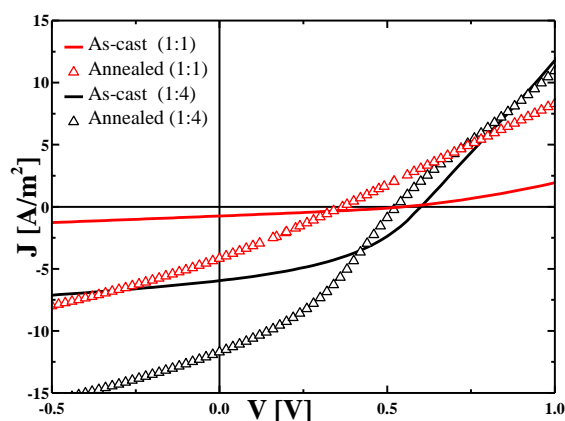


Figure 4.12. Experimental  $J$ - $V$  characteristics of (1:1) and (1:4) ratio P3HT:PDI-1 solar cells. Lines are for as-cast devices, symbols represent the same devices upon annealing at 120°C 10 min. Red line and symbols show the photocurrents of the (1:1) ratio blends, black line and symbols are for the (1:4) ratio blends. The device thicknesses are around 200 nm.

Table 4.2.  $V_{oc}$ ,  $J_{sc}$ , FF and PCE of (1:1) and (1:4) ratio P3HT:PDI-1 solar cells.

Device	$V_{oc}$ [V]	$J_{sc}$ [ $A/m^2$ ]	FF [%]	PCE [%]
(1:1)As-cast	0.54	0.5	36	0.016
(1:1)Annealed	0.35	3.3	26	0.050
(1:4)As-cast	0.60	6.0	40	0.24
(1:4)Annealed	0.53	11.7	34	0.35

As a next step we have studied P3HT:PDI-1 (1:4) ratio solar cells with different cathode materials, both in conventional structure and in the inverted structure. Furthermore, also the annealing temperature was varied. Inverted solar cells have the structure of ITO/ZnO/P3HT:PDI-1/MoO<sub>3</sub>/Al, so the cathode (ZnO) is here the bottom electrode and the MoO<sub>3</sub> anode the top electrode. The *J-V* characteristics of the various solar cells are given in Figure 4.13. and the device performances are summarized in Table 4.3. For the as-cast devices the solar cell with a (Ba\Al) top contact has the best performance, with a slightly higher  $V_{oc}$  and also a higher photocurrent. Upon post-annealing at 80<sup>0</sup>C, the  $V_{oc}$  of the solar cell with Ba/Al cathode decreases around 80 mV, while for the LiF\Al top contact and the inverted structure  $V_{oc}$  doesn't change.

Annealing at 100<sup>0</sup>C significantly lowers the  $V_{oc}$  for the LiF/Al top contact and inverted solar cells. Annealing at 120<sup>0</sup>C even further decreases the  $V_{oc}$  of both the solar cell with LiF/Al top contact and the inverted cell. The solar cell with Ba/Al cathode does not further loose  $V_{oc}$  and remains on the value reached after annealing at 80<sup>0</sup>C. Between as-cast devices and solar cells annealed at 120<sup>0</sup>C the decrease in  $V_{oc}$  is lowest for the Ba\Al (70 mV) cathode, than the LiF\Al cathode (120 mV) and is largest for the inverted (210 mV). As a result, the conventional solar cell device structure with a Ba\Al top contact annealed at 120<sup>0</sup>C shows the best performance. External quantum efficiency (EQE) measurements for (1:4) P3HT:PDI-1 blend solar cells with Ba/Al cathode before and after annealing are shown in Figure 4.14. Compared to (1:1) ratio blends discussed in Chapter 4 (Figure 4.2), the EQE shows a prominent increase, both for the as-cast and annealed devices. For the annealed solar cells with (1:4) P3HT:PDI-1 ratio the EQE reaches to about 20 % at 480 nm. The simulated photocurrents of as-cast and annealed (120<sup>0</sup>C and 10 min.) (1:4) ratio P3HT:PDI-1 devices are shown in Figure 4.15. In order to simulate the decrease in  $V_{oc}$  and increase in photocurrent, electron injection barrier of 0.35 eV and electron mobility of  $7 \times 10^{-9} m^2/Vs$  is used. While the as-cast device simulated with the electron and hole mobilities of single carrier devices (Figure 4.11). It is seen that the small contact barrier is formed upon annealing and the electron mobility is increased around 7 times compared to as-cast device.

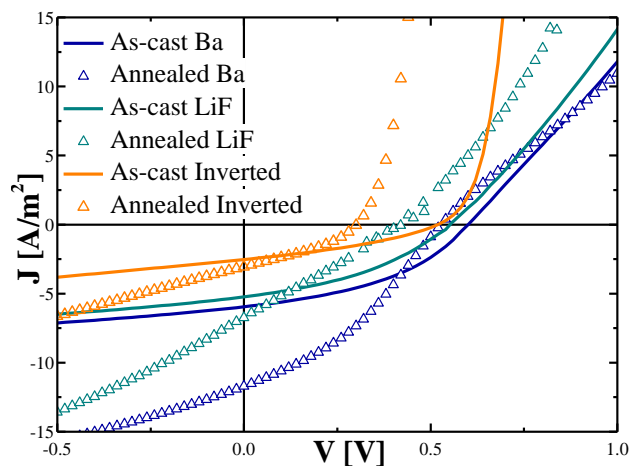


Figure 4.13. Measured  $J$ - $V$  characteristics of (1:4) ratio P3HT:PDI-1 solar cells with Ba/Al, LiF/Al cathode in conventional structure and in inverted structure. Lines are as-cast devices and symbols are the same devices upon post-annealing at 120<sup>0</sup>C 10 min. The device thicknesses are around 200 nm.

Table 4.3. (1:4) ratio P3HT:PDI-1 solar cells with Ba/Al, LiF/Al cathode and inverted structure. The annealing temperatures are 80<sup>0</sup>C, 100<sup>0</sup>C and 120<sup>0</sup>C.

Devices	As-cast	80 <sup>0</sup> C	100 <sup>0</sup> C	120 <sup>0</sup> C
Ba/Al cathode	$V_{oc}$ =0.60 V $J_{sc}$ =6 A/m <sup>2</sup> FF=40 % PCE=0.24 %	$V_{oc}$ =0.52 V $J_{sc}$ =7 A/m <sup>2</sup> FF=30 % PCE=0.18 %	$V_{oc}$ =0.47 V $J_{sc}$ =6 A/m <sup>2</sup> FF=40 % PCE=0.18 %	$V_{oc}$ =0.53 V $J_{sc}$ =11.7 A/m <sup>2</sup> FF=34 % PCE=0.35 %
LiF/Al cathode	$V_{oc}$ =0.55 V $J_{sc}$ =5.4 A/m <sup>2</sup> FF=40 % PCE=0.19 %	$V_{oc}$ =0.53 V $J_{sc}$ =5.4 A/m <sup>2</sup> FF=21 % PCE=0.10 %	$V_{oc}$ =0.46 V $J_{sc}$ =6.6 A/m <sup>2</sup> FF=26 % PCE=0.13 %	$V_{oc}$ =0.43 V $J_{sc}$ =6.7 A/m <sup>2</sup> FF=25 % PCE=0.12 %
Inverted structure	$V_{oc}$ =0.52 V $J_{sc}$ =2.5 A/m <sup>2</sup> FF=30 % PCE=0.065 %	$V_{oc}$ =0.52 V $J_{sc}$ =4.5 A/m <sup>2</sup> FF=33 % PCE=0.13 %	$V_{oc}$ =0.38 V $J_{sc}$ =4.4 A/m <sup>2</sup> FF=35 % PCE=0.1 %	$V_{oc}$ =0.31 V $J_{sc}$ =3.1 A/m <sup>2</sup> FF=33 % PCE=0.053 %

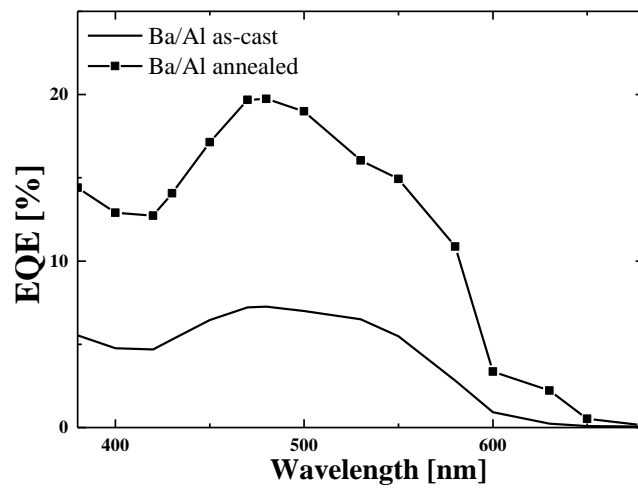


Figure 4.14. External quantum efficiency of (1:4) ratio P3HT:PDI-1 solar cells with Ba/Al top contact before and after annealing at 120°C 10 min.

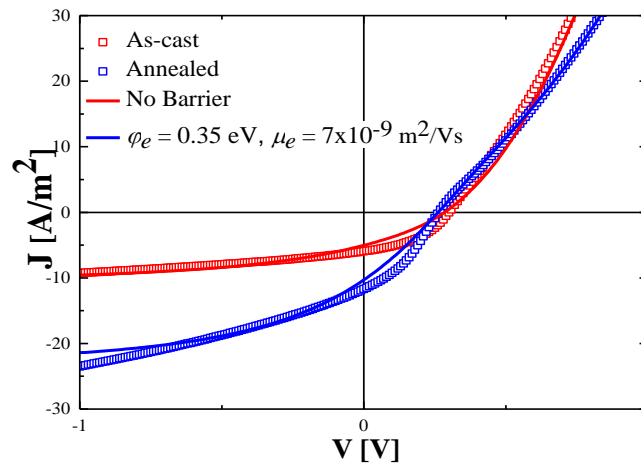


Figure 4.15. Numerical simulation of an as-cast (1:4) ratio P3HT:PDI-1 solar cell under illumination (red line) and numerical simulation of the photocurrent where decrease in  $V_{oc}$  is compensated with an electron barrier ( $\phi_e$ ) of 0.35 eV and mobility of  $7 \times 10^{-9} \text{ m}^2/\text{Vs}$  (blue line). Red symbols are for the experimental as-cast current and blue symbols are for the experimental annealed current.

For comparison also the  $V_{oc}$ -light intensity dependence of as-cast and annealed (120<sup>0</sup>C 10 min.) (1:4) ratio P3HT:PDI-1 solar cells with Ba/Al and LiF/Al cathodes are compared, as shown in Figure 4.16a and 4.16b, respectively. For Ba/Al devices, although the  $V_{oc}$  shows a decrease of 70 mV, the slope of the  $V_{oc}$ -light intensity dependence in as-cast and annealed devices is not affected and amounts to  $kT/q$ . In contrast, for the case of the LiF/Al contact the decrease in  $V_{oc}$  is higher, around 120 mV, and at high light intensities the slope is decreasing to  $kT/2q$  for the annealed devices. Apparently, the slope of  $V_{oc}$ -light intensity dependence is only affected when the electron injection barrier is sufficiently high.

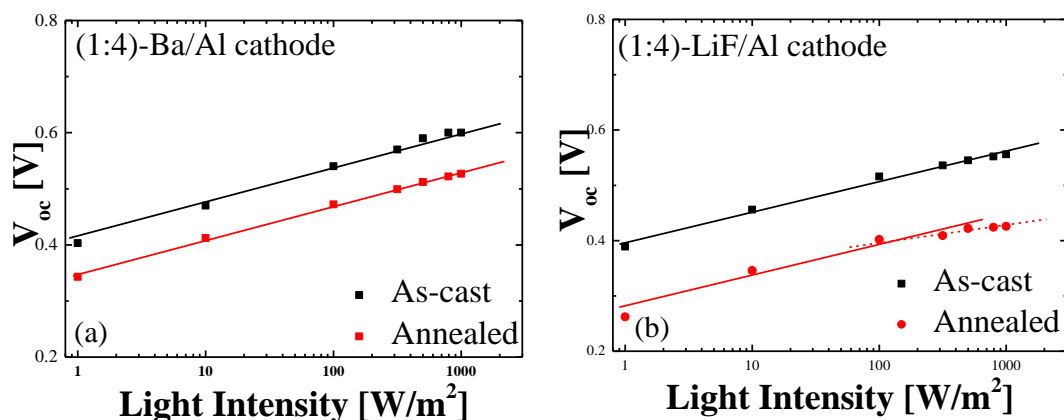


Figure 4.16.  $V_{oc}$ -light intensity dependence of as-cast and annealed (120<sup>0</sup>C 10 min.) (1:4) ratio P3HT:PDI-1 solar cells with Ba/Al (a) and LiF/Al (b) cathode. Solid lines are the slope of  $kT/q$ , while the dotted line is slope of  $kT/2q$ .

As so far has been discussed, in P3HT:PDI-1 solar cells annealing of solar cells show an important decrease in  $V_{oc}$ . It was demonstrated from electron transport measurements and solar cell dark currents and light-intensity dependence of the  $V_{oc}$  decreases. This decrease originates from the occurrence of an electron injection barrier. The amount of  $V_{oc}$  decrease is dependent on the kind of top contact, on the annealing conditions and on the P3HT:PDI-1 blend ratio. In order to investigate whether the decrease of the  $V_{oc}$  upon annealing is specific for P3HT:PDI-1 blends or also occurs for other donor materials we also studied BHJ solar cells with 5-Poly[(4,8-bis-(2-ethylhexyloxy)-benzo(1,2-b:4,5-

b')dithiophene)-2,6-diyl-alt-(4-(2-ethylhexyl)-3-fluorothieno[3,4-b]thiophene)-2-carboxylate-2,6-diyl)] (PTB7) as donor. PTB7 has its LUMO of -3.31 eV and the HOMO around 5.15 eV (Figure 4.17). For the solar cells, PTB7 and PDI-1 are blended in (1:1) ratio and spin casted from chloroform solution. Typical thickness of the active layer amounts to 135 nm. Similar to the P3HT:PDI-1 case the PTB7:PDI-1 solar cells are measured before (as-cast) and after annealing (post-annealing, 120<sup>0</sup>C 10 min). Figure 4.18 shows the current voltage characteristics of an as-cast and annealed solar cell of PTB7:PDI-1 (1:1). The device parameters are shown in Table 4.4. For PTB7:PDI-1 solar cells the device performance is significantly higher as compared to P3HT:PDI-1 as-cast devices. The main increase in device performance stems from a 25 times higher  $J_{sc}$  as compared to P3HT:PDI-1 solar cells. Furthermore, also the  $V_{oc}$  for PTB7:PDI-1 cells is around 151 mV higher for as-cast devices, which originates from the deeper HOMO level of PTB7. In contrast to P3HT-PDI-1 devices in PTB7:PDI-1 solar cells annealing does not affect  $V_{oc}$ . Annealing even slightly decreases the device performance due to a reduction of the photocurrent. This results show that the observed decrease of  $V_{oc}$  upon annealing, i.e. creation of an contact barrier, is dependent on the donor material in the blend with PDI-1 and seems to be specific for the P3HT:PDI-1 system. The microscopic origin of the  $V_{oc}$  decrease in P3HT:PDI-1 blends and comparison of this origin with PTB7:PDI-1 blends are subject of further study

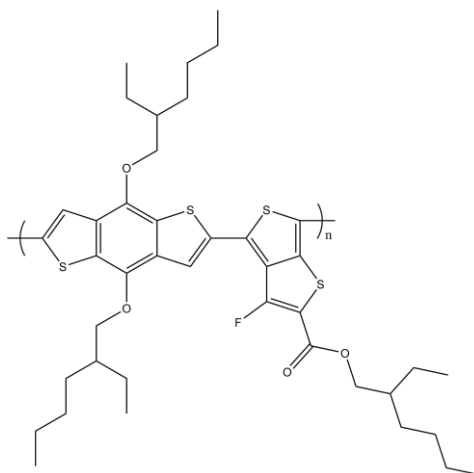


Figure 4.17. 5.Poly[(4,8-bis-(2-ethylhexyloxy)-benzo(1,2-b:4,5-b')dithiophene)-2,6-diyl-alt-(4-(2-ethylhexyl)-3-fluorothieno[3,4-b]thiophene)-2-carboxylate-2,6-diyl)] (PTB7) molecular structure.

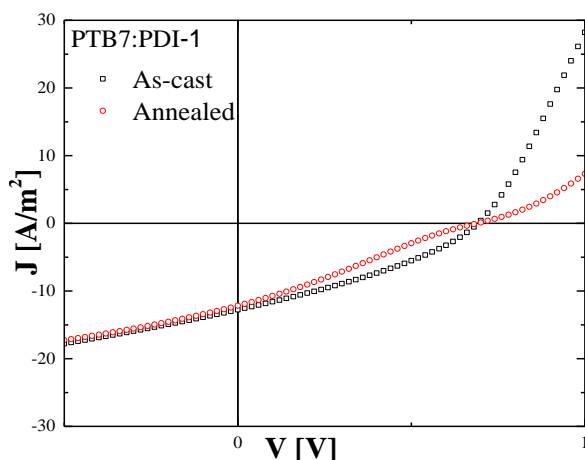


Figure 4.18. Current-voltage characteristics of (1:1) ratio PTB7:PDI-1 solar cells before and after annealing at 120<sup>0</sup>C 10 min. The device thickness amounts to 135 nm.

Table 4.4.  $V_{oc}$ ,  $J_{sc}$ , FF and PCE of (1:1) ratio PTB7:PDI-1 solar cells.

Device	$V_{oc}$ [V]	$J_{sc}$ [A/m <sup>2</sup> ]	FF [%]	PCE [%]
PTB7:PDI-1 As-cast	0.691	12.7	33	0.32
PTB7:PDI-1 Annealed	0.689	12.1	26	0.26

#### 4.7. Conclusions

In this chapter the device characteristics of (1:1) ratio P3HT:PDI-1 solar cells are investigated. As-cast devices show a very low photocurrent, which is attributed to low generation rate of bound  $e-h$  pairs, combined with a low dissociation rate. Besides low mobility of charge carriers increases bimolecular recombination losses. Both the low mobility and field dependent generation rate decreases the FF. Subsequently, the solar cells are annealed at 120<sup>0</sup>C for 10 minutes. Upon annealing, the solar cells show an increased



photocurrent, but also a reduced open-circuit voltage. Measurements of the dark current and open circuit voltage as a function of light intensity all indicate towards the presence of a contact barrier, which is consistent with the observation of injection-limited currents in electron-only devices upon annealing (Chapter 3).  $V_{oc}$ -light intensity measurements reveal in the as-cast devices a slope of  $kT/q$ , whereas in the annealed solar cells the slope decreases to  $kT/2q$  at high light intensities, which is the fingerprint of a contact barrier. Annealing is a crucial step in order to gain photocurrent in P3HT:PDI-1 solar cells due to an increased electron transport, but it simultaneously deteriorates the electron contact leading to a loss in  $V_{oc}$ , such that the efficiency is only moderately enhanced. In order to further investigate the P3HT:PDI-1 blends, solar cells and single carrier devices are investigated in (1:4) ratio. In (1:4) ratio the transport is more balanced and the electron mobility is prominently higher as compared to the (1:1) ratio, while the hole mobility in the P3HT phase doesn't show a prominent change compared to (1:1) ratio. As result of a better charge transport, (1:4) ratio solar cells exhibited better solar cell performances both in the as-cast and annealed devices.

#### **4.8. Experimental**

Regioregular poly(3-hexylthiophene) rr-P3HT donor and commercial perylene-3,4,9,10-perylene tetracarboxylic acid diimide (PDI) acceptor are blended in a (1:1) ratio and spin casted at 1000 rpm from a chloroform solution. Devices were fabricated on a glass substrate that is covered with patterned indium tin oxide (ITO). Glass/ITO substrates were cleaned with a detergent agent and ultrasonicated in acetone and isopropanol, and the cleaning was finished with a UV-ozone treatment. Blends are sandwiched between poly(3,4-ethylenedioxythiophene)/poly(styrenesulfonate) (PEDOT:PSS) as hole-conducting bottom electrode and for the top contact either barium (Ba) (5 nm) /Aluminum (Al) (100 nm) or lithium fluoride (LiF) (1 nm)/ Al (100 nm) was used. Inverted solar cells have the structure of ITO/zinc oxide (ZnO) (~20 nm)/P3HT:PDI-1/ Molybdenum trioxide ( $\text{MoO}_3$ ) (10 nm)/Al, so the cathode (ZnO) is here the bottom electrode and the  $\text{MoO}_3$  anode the top electrode, where ZnO has prepared from 20 mg/ml zinc acetylacetonate hydrate/ethanol solution. Both the ITO/glass substrate and the ZnO solution are heated to  $\sim 63^\circ\text{C}$  and solution is coated at 1000 rpm and annealed directly at  $120^\circ\text{C}$  5 min. Then the blend (P3HT:PDI-1) and cathode ( $\text{MoO}_3/\text{Al}$ ) is coated. In all cases, the complete devices are annealed at  $120^\circ\text{C}$  10 min. in nitrogen atmosphere. Devices are measured under a nitrogen

atmosphere with a Keithley 2400 source meter. For the solar cell measurements, a white halogen lamp with a set of seven neutral density filters is used for the measurements of  $V_{oc}$  on incident light power. Solar cell efficiencies are corrected according to light intensity of  $600 \text{ W/m}^2$  for P3HT:PDI-1 solar cells and  $860 \text{ W/m}^2$  for PTB7:PDI-1 solar cells.

## 4.9. References

- [1] G. Yu, J.Gao, J.C. Hummelen, F. Wudl, and A. J. Heeger, *Science* **270**, 1789 (1995).
- [2] C. J. Brabec, S.G., J. J. M. Halls, D. Laird, S. Jia, and S. P. Williams, *Adv. Mater.* **22**, 3839 (2010).
- [3] C. Zhan, X.Z., and J. Yao, *RSC Adv.* **5**, 93002 (2015).
- [4] C. B. Nielsen, S. Holliday, H.-Y. Chen, S. J. Cryer, and I. McCulloch, *Acc. Chem. Res.* **48**, 2803 (2015).
- [5] S. Holliday, R.S. Ashraf, C. B. Nielsen, M. Kirkus, J. A. Röhr, C.-H. Tan, E. Collado-Fregoso, A.-C. Knall, J. R. Durrant, J. Nelson, and Iain McCulloch, *J. Am. Chem. Soc.* **137**, 898 (2015).
- [6] G. Sauvé and R.Fernando, *J. Phys. Chem. Lett.* **6**, 3770 (2015).
- [7] S. Holliday, R.S. Ashraf, A. Wadsworth, D. Baran, S. A. Yousaf, C. B. Nielsen, C.-H. Tan, S. D. Dimitrov, Z. Shang, N. Gasparini, M. Alamoudi, F. Laquai, C. J. Brabec, A. Salleo, J. R. Durrant, and I. McCulloch, *Nat. Commun.*, **7**, **11585** (2016).
- [8] C. Li and H. Wonneberger, *Adv. Mater.* **24**, 613 (2012).
- [9] C. W. Tang *Appl. Phys. Lett.* **48**, 183 (1986).
- [10] Ian A. Howard, F.Laquai, P. E. Keivanidis, R. H. Friend, and N. C. Greenham, *J. Phys. Chem. C* **113**, 21225 (2009).
- [11] S. Rajaram, P. B. Armstrong, B. J. Kim, and J. M. J. Fréchet, *J Phys Chem Lett.* **21** 2405 (2012).
- [12] V. Kamm, G. Battagliarin, I. A. Howard, W. Pisula, A. Mavrinskiy, C. Li, K. Müllen, and F. Laquai, *Adv. Energy Mater.* **1**, 297 (2011).
- [13] V. D. Mihailetschi, P.W.M. Blom, J. C. Hummelen, and M. T. Rispens, *J. Appl. Phys.* **94**, 6849 (2003).
- [14] L. J. A. Koster, V. D. Mihailetschi, R. Ramaker, P. W. M. Blom, *Appl. Phys. Lett.* **86** 123509 (2005).
- [15] S. Solak, P. W. M. Blom, and G. A. H. Wetzelaer, *Appl. Phys. Lett.* **109**, 053302 (2016).

- [16] D.E. Motaung, G.F.M., S. S. Nkosi, G. H. Mhlongo, B. W. Mwakikunga, T. Malwela, C. J. Arendse, T. F. G. Muller, F. R. Cummings, *J. Mater. Sci.* **48**, 1763 (2013).
- [17] L. Onsager, *J. Chem. Phys.* **2**, 599 (1934).
- [18] C. L. Braun, *J. Chem. Phys.* **80**, 4157 (1984).
- [19] L. J. A. Koster, E. C. P. Smits, V. D. Mihailetschi, and P. W. M. Blom, *Phys. Rev. B.* **72** 085205 (2005).
- [20] V. D. Mihailetschi, H. Xie, B. de Boer, L. J. A. Koster, and P. W. M. Blom, *Adv. Funct. Mater.* **16**, 699 (2006).
- [21] F. Laquai, D. Andrienko, R. Mauer, and P. W. M. Blom, *Macromol. Rapid Commun.* **36**, 1001 (2015).

## **5. Charge transport in P3HT:perylene diimide derivatives**

The electron transport in a blend of regioregular poly(3-hexylthiophene) (rr-P3HT) as donor and two different perylene diimide derivatives with ortho- substitution as acceptor is studied. Drift-diffusion simulations are performed to model the electron transport. As compared to the commercial PDI-1 derivative a slightly lower electron-mobility is observed in the as-cast devices. The role of the electron injecting contact is discussed and correlated to the decrease in open-circuit voltage in annealed solar cells.

## 5.1. Introduction

As discussed in Chapters 3 and 4, perylene diimides (PDI) have been considered as new alternative acceptor materials to replace fullerene derivatives for organic electronic applications. An attractive feature of PDIs is the availability of their functional *peri*-, *bay*- and *ortho*- positions (see Chapter 3 Figure 3.1). This opens the opportunity to modify its electrical and optical properties to achieve the desired charge transport properties and morphologies for organic electronic applications [1]. The first generation PDIs [1] exhibited strong  $\pi$ - $\pi$  stacking of the molecules and largely phase separated aggregates are created. These aggregates are then claimed to hinder device performance of organic solar cells [2-4]. Therefore, for organic solar cell applications the design of new PDI derivatives aims at decreasing and controlling the aggregation properties of PDI molecules.

In a review article by Li et al., the history of PDIs both in terms of material synthesis and device application are extensively described [1]. It has been discussed that the core substitution in PDI highly affects the absorption and electronic properties of the molecule. It was also shown that the substitution in the *bay*- position of PDIs causes twisting of the molecules (both in the core and between PDI molecules) and may have negative effect on the molecular packing properties for a good morphology [1]. Via *ortho*- substitution the aim is to disrupt high packing of molecules without causing twisting in the core of the PDI molecule. Therefore, *ortho*- substitution is promising in order to prevent high level of packing which leads to fast bimolecular recombination and intermolecular state formation [1].

In this chapter electron-only devices and solar cells of two newly synthesized PDI derivatives are studied and they are named as PDI-2 and PDI-3, as shown in Figure 5.1. Both materials have core substitutions in the positions 2-, 5-, 8-, and 11- (see Chapter 3 Figure 3.1). Additionally, PDI-2 has a short alkyl chain in the N-position, similar to commercial PDI-1, while PDI-3 has a longer alkyl chain in the N-position. It has been previously shown that core substitution prevents close interactions of the molecules in the solid state of material. This prevents strong aggregation of the material [2,5,6] and positively affects the solar cell performance.

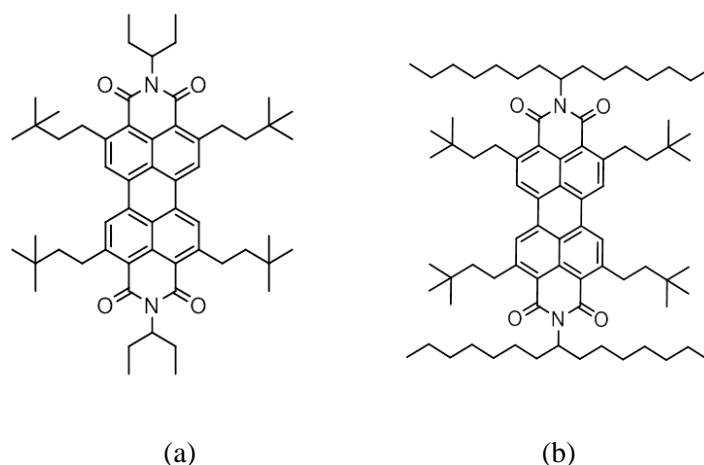


Figure 5.1. Structural formulas of (a) PDI-2 and (b) PDI-3 small molecule PDI derivatives.

## 5.2. Electron and hole transport in PDI derivatives

Electron-only devices of (1:1) ratio P3HT:PDI-2 and P3HT:PDI-3 blends are investigated and current-voltage ( $J$ - $V$ ) characteristics are shown in Figure 5.2. For as-cast devices the P3HT:PDI-2 electron-only device shows a nearly symmetric  $J$ - $V$  curve, indicating that in forward bias (electron injection from LiF/Al) and reverse bias (injection from Al), good electron injection is achieved. In the case of P3HT:PDI-3 electron only devices, the highest current is seen in reverse bias, similar to the case of P3HT:PDI-1 electron-only devices in Chapter 3. Therefore, the electron-current injected from the LiF/Al top contact in forward bias is clearly injection limited. The representative currents in both P3HT:PDI-2 (forward bias) and P3HT:PDI-3 (reverse bias) are nearly equal in magnitude and both show a quadratic dependence on voltage. As a result these electron currents exhibit space-charge-limited behavior and are described by the Mott-Gurney law [8]. In Figure 5.3a and 5.3b drift-diffusion simulations of the temperature dependence of the electron current in P3HT:PDI-2 and P3HT:PDI-3 blends are shown, respectively. For both blends the disorder parameter ( $\sigma$ ) is  $\sim 0.15$  eV, which is similar to what was found for P3HT:PDI-1 blends (0.1476 eV) (see Chapter 3). As a result it is expected that the charge transport in these blends will be relatively equal to the results found for P3HT:PDI-1 blends. The zero-field mobility for electrons are found to be  $2 \times 10^{-11} \text{ m}^2/\text{Vs}$  and  $1 \times 10^{-11} \text{ m}^2/\text{Vs}$  for P3HT:PDI-2 and P3HT:PDI-3 from as-cast electron-only devices, respectively. These electron mobilities are 2.25 and 4.5 times lower as compared to the electron mobility in as-cast P3HT:PDI-1 blends. The zero field mobility for holes are found to be  $3.5 \times$

$10^{-10} \text{ m}^2/\text{Vs}$  and  $1.3 \times 10^{-9} \text{ m}^2/\text{Vs}$  for P3HT:PDI-2 and P3HT:PDI-3 from as-cast hole-only devices, respectively (Figure 5.5). The hole mobility in as-cast P3HT:PDI-2 is 2 times lower as compared to as-cast P3HT:PDI-1 blends, whereas for P3HT:PDI-3 blends the hole mobility is 2 times higher. So in all cases the measured electron- and hole mobilities are relatively close.

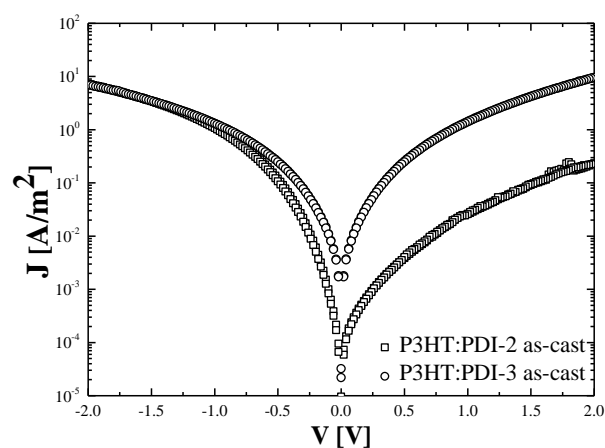


Figure 5.2. The current-voltage characteristics of as-cast P3HT:PDI-2 and P3HT:PDI-3 electron-only devices. Device thicknesses are 65 nm and 60 nm, respectively.

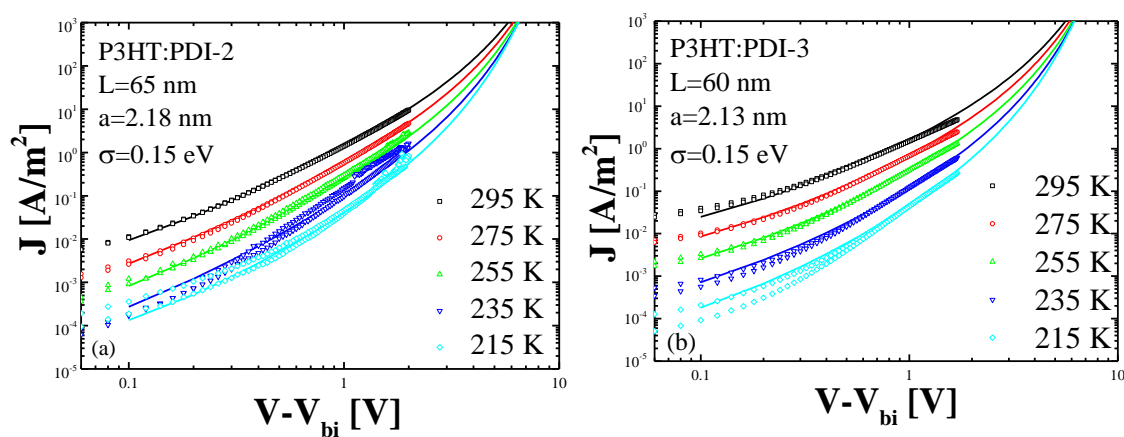


Figure 5.3. Drift-diffusion simulation of measured as-cast electron-only currents of (1:1) ratio P3HT:PDI-2 and P3HT:PDI-3 blends. Symbols are the experimental  $J$ - $V$  characteristics at indicated temperatures and solid lines are fits to the experimental data. The simulation parameters are indicated as an inset.



### 5.3. The effect of annealing on electron and hole current in PDI derivatives

In Figure 5.4a and 5.4b the  $J$ - $V$  characteristics of as-cast and annealed P3HT:PDI-2 and P3HT:PDI-3 based electron-only devices are shown, respectively. In P3HT:PDI-2 devices, the electron current decreases around 2 orders of magnitude in forward bias, while in reverse bias there is only a slight change in the current. As a result, upon annealing the quality of the top contact is strongly affected and the current in forward bias becomes injection limited. In P3HT:PDI-3 devices, where the current from the top contact was already injection limited in as-cast devices, annealing decreases the electron current around 1.5 order of magnitude both in reverse and forward bias. Since both bulk-limited (reverse bias) and injection limited current (forward bias) of the as-cast devices decrease simultaneously upon annealing it is not clear whether this is the result of a degradation of both contacts or a reduction of the bulk mobility. In Figure 5.5 the  $J$ - $V$  characteristics of as-cast and annealed hole-only devices are seen. In P3HT:PDI-2 devices the hole current increases by one order of magnitude upon annealing, whereas for P3HT:PDI-3 blends the hole-currents only shows a slight change. After annealing the zero-field hole mobility increases from  $3.5 \times 10^{-10} \text{ m}^2/Vs$  to  $2.2 \times 10^{-9} \text{ m}^2/Vs$  for the P3HT:PDI-2 blends.

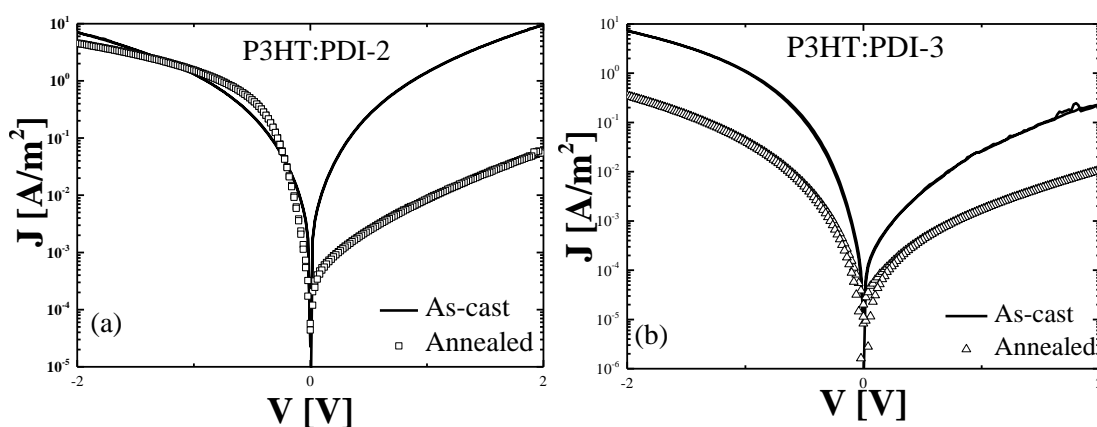


Figure 5.4. The current-voltage characteristics of P3HT:PDI-2 (a) and P3HT:PDI-3 (b) electron-only devices before (solid lines) and after annealing (symbols) at  $120^{\circ}\text{C}$  10 min. Device thicknesses are 65 nm and 50 nm, respectively.

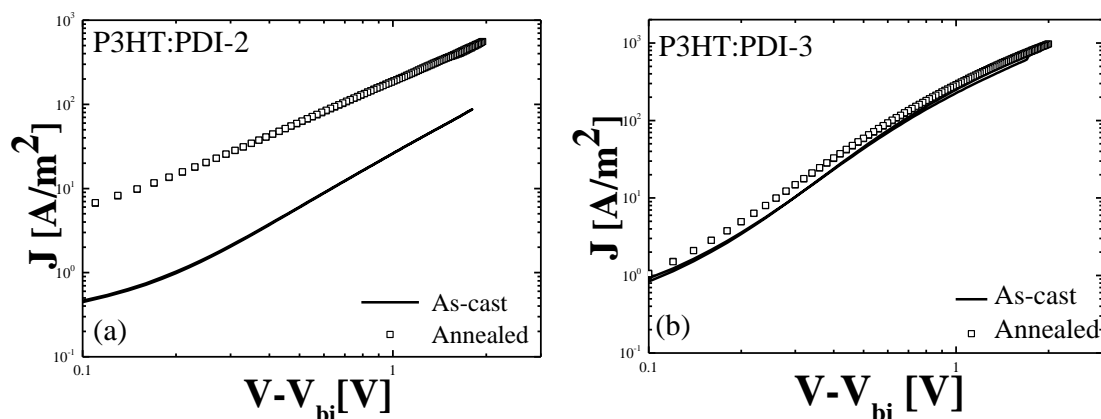


Figure 5.5. Current-voltage characteristics of P3HT:PDI-2 (a) and P3HT:PDI-3 (b) hole-only devices before (solid lines) and after annealing (symbols) at 120<sup>0</sup>C 10 min. Device thicknesses are 65 nm and 50 nm, respectively

As a summary, for the P3HT:PDI-2 blends the electron transport is not affected by annealing, whereas the hole transport is increased. In contrast, for the P3HT:PDI-3 blends the electron current is strongly reduced, whereas the hole current remains unaffected.

#### 5.4. Solar Cells

As a next step, the performance of P3HT:PDI-2 and P3HT:PDI-3 blends are investigated in (1:1) ratio in solar cells. Solar cells are fabricated by sandwiching the blends between a PEDOT:PSS anode and LiF/Al cathode. The current under illumination and the relevant device parameters ( $V_{oc}$ ,  $J_{sc}$ , FF and PCE) are shown in Figure 5.6 and Table 5.1 for as-cast and annealed devices (120<sup>0</sup>C 10 min), respectively. As-cast solar cells of P3HT:PDI-2 and P3HT:PDI-3 clearly show a higher  $V_{oc}$  and  $J_{sc}$  than P3HT:PDI-1 solar cells (see Chapter 4). The highest  $V_{oc}$  (0.66 V) is measured for as-cast P3HT:PDI-2, which upon annealing decreases with 120 mV to 0.54 V. On the other hand, the  $V_{oc}$  of P3HT:PDI-3 blends slightly increases from 0.55 V to 0.57 V upon annealing. It has been shown in Chapter 4 that the annealing process highly affects the  $V_{oc}$  in P3HT:PDI-1 blends, the decrease in  $V_{oc}$  upon annealing amounts to 190 mV. In order to correlate the observed  $V_{oc}$  with the electron transport properties it should be noted that since solar cells have an evaporated LiF/Al top electrode the forward electron-only currents of Figure 5.4 have to be considered. For the P3HT:PDI-2 blend a strong decrease of the forward bias was observed, whereas the reverse

bias remained unchanged. This shows that the electron transport itself is not affected by annealing, but that the injection quality of the LiF/Al top contact is deteriorated due to the presence of an electron injection barrier. This observation is consistent with the decrease of  $V_{oc}$  in P3HT:PDI-2 solar cells, similar to the case of P3HT:PDI-1 solar cells (Chapter 4). For the P3HT:PDI-3 blend the electron current in forward bias was already injection limited in the as-cast devices. As a result the as-cast solar cells are expected to exhibit a lower  $V_{oc}$  as compared to the P3HT:PDI-2 case, as is also observed, see Table 5.1. Upon annealing the forward electron current in the P3HT:PDI-3 blend decreases, but the  $V_{oc}$  does not really change. The even lower electron current upon annealing can therefore not be explained by a further increase of the electron injection barrier, which would also result in a lowering of  $V_{oc}$ . A lowering of the electron mobility could also explain the simultaneous decrease of the forward (bulk) and reverse (injection-limited) bias.

However, this explanation seems to contradict with the gain in  $J_{sc}$  as observed for both P3HT:PDI-2 and P3HT:PDI-3 blends upon annealing (Table 5.1). It should be noted that an increased photocurrent not necessarily means that the electron mobility in the P3HT:PDI-3 blends has to be increased after annealing. An eventual decrease of the electron mobility can be compensated by an increase of the generation rate  $G_{max}$  due to an improved morphology for generation of bound electron-hole pairs. The increase in photocurrent after annealing leads to a higher device efficiency for the annealed P3HT:PDI-2 and P3HT:PDI-3 solar cells. So far, the annealed P3HT:PDI-2 blend gives the best performance, but the difference with the annealed P3HT:PDI-3 solar cells is small. For as cast-devices the differences between the two material systems are more prominent. Looking at the solar cell efficiency the core substitution in PDI positively affects the solar cell performance, as compared to the commercial PDI-1.

In Figure 5.7 the  $V_{oc}$ -light intensity dependence of as-cast P3HT:PDI-2 and P3HT:PDI-3 solar cells are shown, together with P3HT:PDI-1 solar cells for comparison. The slopes of  $kT/q$  and  $kT/2q$  are indicated in the graph. It appears from Figure 5.7 that the  $V_{oc}$ -light intensity dependence of the P3HT:PDI-3 blends deviates from the slope of  $kT/q$  at high light intensities and approaches to  $kT/2q$ . This behavior is characteristic for solar cells with an injection-limited contact and is consistent with the observations of the reduced electron current in forward bias (Figure 5.2) and reduced  $V_{oc}$  (Figure 5.6). In the case of P3HT:PDI-1 and P3HT:PDI-2, where the as-cast devices have an ohmic electron top contact, the whole intensity range is described by a slope of  $kT/q$ .

External quantum efficiencies (EQE) of as-cast and annealed P3HT:PDI-2 and P3HT:PDI-3 blends are shown in Figure 5.8. As-cast P3HT:PDI-2 devices show a very low EQE (4 % at peak at 530 nm), while P3HT:PDI-3 solar cells show a higher EQE around 13 % at 530 nm. Upon annealing the EQEs of both blends increase for all wavelengths and show a similar behavior, which is consistent with the nearly equal solar cell performances, as shown in table 5.1. Previously, P3HT:PDI-2 blends were investigated in solar cells by Kamm et al. in solar cells [5] and by Puniredd et al. in field effect transistors [9]. Besides, from XRD measurement it has been shown that the packing behavior is slightly affected in P3HT:PDI-2 films upon annealing [5].

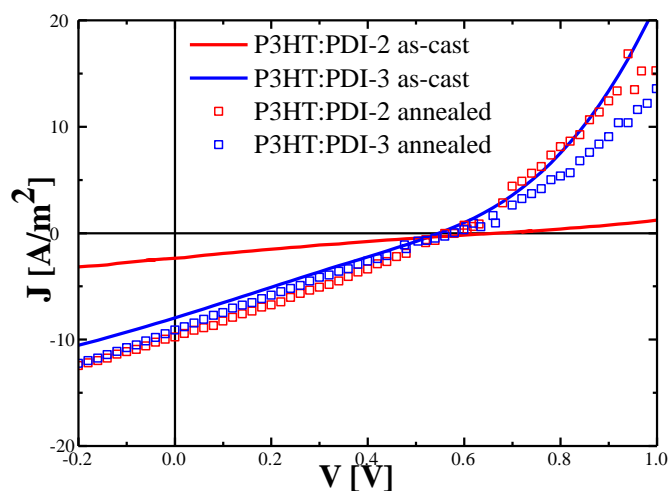


Figure 5.6. Current-voltage characteristics of P3HT:PDI-2 and P3HT:PDI-3 solar cells before (solid lines) and after annealing (symbols) at 120<sup>o</sup>C 10 min. Device thicknesses are 60 nm and 50 nm, respectively.

Table 5.1. Solar cell parameters of current-voltage characteristics of figure 5.6.

Device	$V_{oc}$	$J_{sc}$ [A/m <sup>2</sup> ]	FF [%]	PCE [%]
(1:1) As-cast P3HT:PDI-2	0.66	2.3	19	0.05
(1:1) Annealed P3HT:PDI-2	0.54	9.7	26	0.22
(1:1) As-cast P3HT:PDI-3	0.55	7.9	25	0.18
(1:1) Annealed P3HT:PDI-3	0.57	9.1	25	0.22

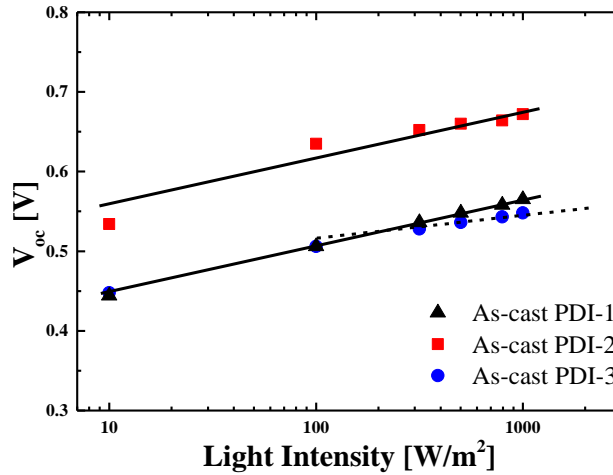


Figure 5.7. The  $V_{oc}$ -light intensity dependence in (1:1) P3HT:PDI-1, P3HT:PDI-2 and P3HT:PDI-3 solar cells. The experimental data are represented by symbols, solid line indicates a slope of  $kT/q$  and the dotted line represents a slope of  $kT/q$ .

## 5.5. Conclusions

The electron transport in blends of P3HT with various PDI derivatives has been studied. The zero field mobilities in as-cast devices of *ortho*-substituted PDIs are found as  $2 \times 10^{-11} \text{ m}^2/\text{Vs}$  and  $1 \times 10^{-11} \text{ m}^2/\text{Vs}$  for P3HT:PDI-2 and P3HT:PDI-3, respectively. The slightly lower electron mobility as compared to the commercial PDI-1 might arise from the small increase of the energetic disorder. As-cast P3HT:PDI-2 electron-only devices exhibit SCLC behavior, however upon annealing the LiF/Al top-contact quality decreases and the electron current becomes injection limited. In P3HT:PDI-3 blends already as-cast devices show an injection-limited current for the LiF/Al top contact, and upon annealing this injection-limited current further decreases. When applied in solar cells, as-cast and annealed devices of P3HT:PDI-2 and P3HT:PDI-3 show a higher photocurrent density than devices of commercial PDI-1 blended with P3HT. Therefore, higher device efficiencies are measured for the *ortho*-substituted PDI derivatives as acceptor in BHJ solar cells. Similar to the commercial PDI-1 based blends the  $V_{oc}$  significantly decreases upon annealing in the P3HT:PDI-2 solar cells. As-cast P3HT:PDI-3 solar cells have already lower  $V_{oc}$  values and show a decreased  $V_{oc}$ -light intensity dependence at high light intensities, indicative for an injection-limited contact. In order to further improve the performance of PDI based

acceptors newly designed derivatives are necessary to reduce the losses in  $V_{oc}$  and increase the charge generation.

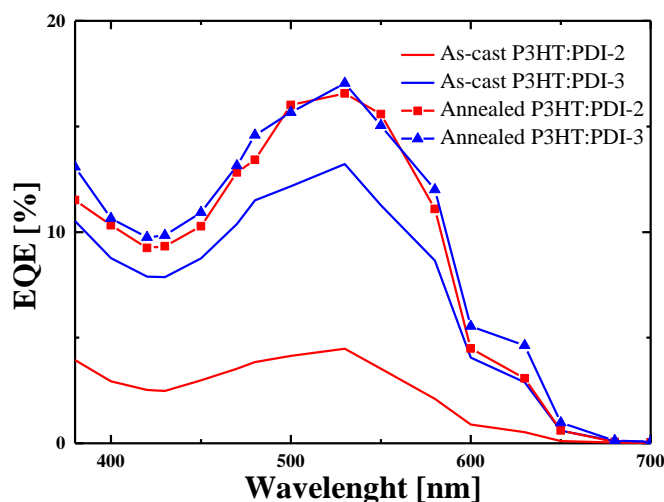


Figure 5.8. EQE (external quantum efficiency) spectrum of P3HT:PDI-2 and P3HT:PDI-3 based as-cast and annealed solar cells at 120°C 10 min.

## 5.6. Experimental

Perylene diimide derivatives with N- and ortho substitution are synthesized in the group of Prof. Klaus Müllen at the Max Planck Institute Polymer Research. In this work, ortho substituted PDI-2 and PDI-3 (PDI-3 material has a longer alkyl chain in the N-position) are blended with regioregular poly(3-hexylthiophene) rr-P3HT as donor material in a (1:1) ratio and spin casted from chloroform solution at 1000 rpm. The concentration of the solutions amount to 6.6 mg/ml. Devices were fabricated on a glass substrate covered with patterned indium tin oxide (ITO). The ITO substrates were cleaned with a detergent agent and ultrasonicated in acetone and isopropanol, and the cleaning was finished with a UV-ozone treatment. Blends are sandwiched between poly(3,4-ethylenedioxythiophene)/poly(styrenesulfonate) (PEDOT:PSS) as hole-conducting bottom electrode and for the top contact an evaporated lithium fluoride (LiF) (1 nm)/aluminum (Al) (100 nm) contact is used in solar cells. In electron-only devices glass substrates were used and cleaned in the same way as the glass/ITO substrates. The bottom contact is Al (30 nm) and the top contact is evaporated LiF(1nm)/Al (100nm). Devices are measured under a

nitrogen atmosphere with a Keithley 2400 source meter. Solar cell efficiencies are corrected according to light intensity of  $600 \text{ W/m}^2$ .

## 5.7. References

- [1] C. Li and H. Wonneberger, *Adv. Mater.* **24**, 613 (2012).
- [2] S. Rajaram, P. B. Armstrong, B. J. Kim, and J. M. J. Fréchet, *Chem. Mater.* **21**, 1775 (2009).
- [3] Chen, Y.; Zhang, X.; Zhan, C.; Yao, J. *Phys. Status Solidi A*, **212**, 1961 (2015).
- [4] P. E. Hartnett, E. A. Margulies, H. S. S. R. Matte, M. C. Hersam, T. J. Marks, and M. R. Wasielewski, *Chem. Mater.* **28**, 3928 (2016).
- [5] V. Kamm, G. Battagliarin, I. A. Howard, W. Pisula, A. Mavrinskiy, C. Li, K. Müllen, and F. Laquai, *Adv. Energy Mater.* **1**, 297 (2011).
- [6] T. T. Clikeman, E. V. Bukovsky, X.-B. Wang, Y.-S. Chen, G. Rumbles, S. H. Strauss, and O. V. Boltalina, *Eur. J. Org. Chem.*, 6641 (2015).
- [7] G. Sauvé and R. Fernando, *J. Phys. Chem. Lett.* **6**, 3770 (2015).
- [8] N. F. Mott and R. W. Gurney, *Electronic Processes in Ionic Crystals* (Oxford University Press, London, 1940).
- [9] S. R. Puniredd, A. Kiersnowski, G. Battagliarin, W. Zaja, W. Zajaczkowski, W.W. H. Wong, N. Kirby, K. Müllen, and W. Pisula, *J. Mater. Chem. C* **1**, 2433 (2013).



## **6. Electron transport in P(NDI2OD-T2) polymer with varying molecular weights**

The electron-transport in the n-type Poly{[N,N0-bis(2-octyldodecyl)-naphthalene-1,4,5,8-bis(dicarboximide)-2,6-diyl]-alt-5,50-(2,20-bithiophene)} [P(NDI2OD-T2)], known also as Activink N2200 polymers is investigated for various molecular weights. No systematic dependence of the electron transport on molecular weight is observed. Compared to the commercial N2200 all compounds exhibit a lower mobility and higher energetic disorder. A possible cause for the reduced electron transport is the occurrence of electron traps remaining from the synthesis.

## **6.1. Introduction**

In organic semiconductors the hole transport is typically trap free and space-charge limited, while the electron transport is limited by traps [1-3]. Therefore, organic semiconductors with both trap-free electron and hole transport are highly wanted in order to improve the performance of organic electronic devices such as organic solar cells, light emitting diodes and field-effect transistors.

In recent years it was found that organic semiconductors with a LUMO deeper than  $\sim 3.6$  eV exhibit trap-free electron transport [4]. In Chapter 3 a commercial perylene diimide derivative with the LUMO  $\sim 3.8$  eV has been discussed and trap-free electron transport was demonstrated. In the last years, also conducting polymers with trap-free electron transport have been developed, amongst them the well-known N2200 polymer, developed by Polyera Corporation shown in Figure 6.1. The N2200 polymer has the LUMO around  $\sim 4$  eV and the HOMO at  $\sim 5.6$  eV [5]. The N2200 polymer is a promising acceptor material for organic solar cells and an efficiency of 8.27 % has been reported for all-polymer BHJ solar cells [6].

The charge transport in the N2200 polymer has been studied by several groups [6-15]. A high electron mobility of  $1 \times 10^{-7} \text{ m}^2/\text{Vs}$  has been reported from time-of-flight measurements [7]. In 2010, Steyrlleuthner et al. studied the electron transport in N2200 based diodes it was shown that although N2200 has a LUMO at  $\sim 4$  eV the electron current is injection limited for common cathode materials [7]. The measured electron current scaled with the applied electric field, which is a footprint of an injection-limited current [7]. In Chapters 3 and 5 injection limited electron currents also occurred in some of the perylene derivatives, in spite of a deep LUMO at  $\sim 3.8$  eV, either in the as-cast or annealed electron-only devices with the common cathode barium/aluminum as injecting contact. Later in 2012, Wetzelaer et al. studied the electron and hole transport in the N2200 polymer [14]. It was demonstrated that a bulk-limited SCL current was obtained when cesium carbonate ( $\text{Cs}_2\text{CO}_3$ ) is used as cathode material.  $\text{Cs}_2\text{CO}_3$  is known to act as an n-type doping for organic semiconductors upon thermal evaporation with its decomposition to cesium suboxides [16].

In this chapter, the effect of molecular weight on the electron transport is studied in the N2200 polymer with three different molecular weights. The polymers are synthesized in the group of Dr. Michael Sommer at the University of Freiburg. Electron-only devices have been fabricated using a  $\text{Cs}_2\text{CO}_3$ /Aluminum cathode and drift-diffusion simulations have been performed to analyze the measured electron currents. As a reference, also the

commercial N2200 from Polyera was studied. Compared to the commercial N2200, the materials studied here show lower electron mobility as compared to commercial N2200 material. Furthermore, there is no systematic relation between the electron mobility and the molecular weight of the material.

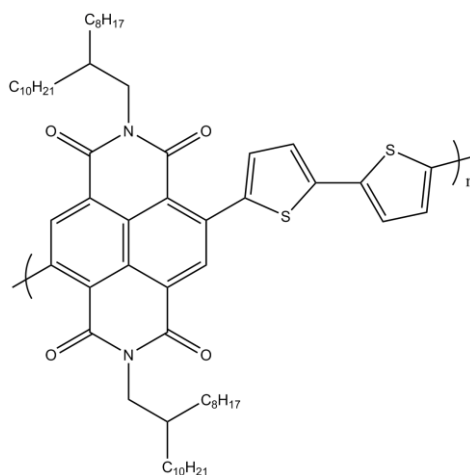


Figure 6.2. Chemical structure of P(NDI2OD-T2), also known as Activink N2200 that has naphthalene diimide core and bithiophene unit.

## 6.2. Electron Transport in commercial N2200 from Polyera

Electron-only devices of the commercial N2200 polymer (Polyera Corporation) are studied using a  $\text{CsCO}_3/\text{Al}$  top electrode as injecting cathode. The thickness of the  $\text{CsCO}_3$  interlayer is varied between 1 nm and 2 nm and followed by 100 nm aluminum (Al) capping layer. The N2200 polymer is spin coated from toluene. The electron currents of 12 devices are shown in Figure 6.2a and 6.2b for a 1nm or 2 nm layer of  $\text{CsCO}_3$ , respectively. The active layer thickness amounts to 215 nm for all devices. We observe that the electron currents are highly reproducible in both cases, i.e. on top of each other and the devices show an asymmetric behavior of the current density. In agreement with earlier literature results, the forward bias where electrons are injected from the  $\text{CsCO}_3/\text{Al}$  top electrode is higher than the reverse bias, meaning electron injection from the bottom Al electrode. In Figure 6.3a and 6.3b a representative current for each case is shown in a double logarithmic scale. In both cases, we observe a linear behavior at low voltages and a quadratic behavior at high voltages, which is a sign of a space charge limited current. The deviation at high voltages stems from the charge carrier density and electric field dependence of the mobility as it is previously demonstrated in the literature for commercial N2200 [14]. The numerical drift-diffusion simulations of the temperature dependence of the electron current are shown in

Figure 6.4a and 6.4b. The temperature dependence in both cases is very well described by the simulations. The zero-field and zero-density electron mobility at room temperature amounts found to be  $3.78 \times 10^{-8} \text{ m}^2/\text{Vs}$ . The density, field and temperature dependence of the electron mobility of commercial N2200 is characterized by an average intersite spacing ( $a$ ) of 3.0 nm and an energetic disorder parameter ( $\sigma$ ) of 0.085 eV.

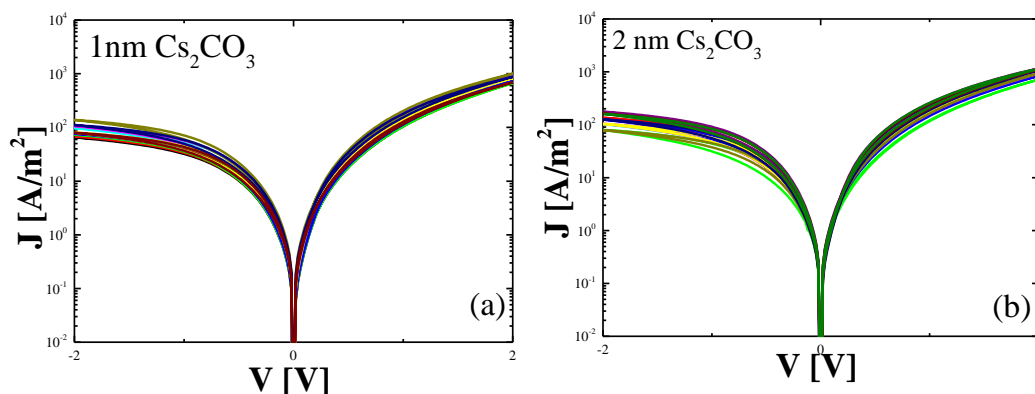


Figure 6.2. Current-voltage characteristics of commercial N2200 electron-only devices with a thickness of 215 nm using a 1 nm (a) and 2 nm (b) cesium carbonate ( $\text{Cs}_2\text{CO}_3$ ) interlayer at the top electrode.

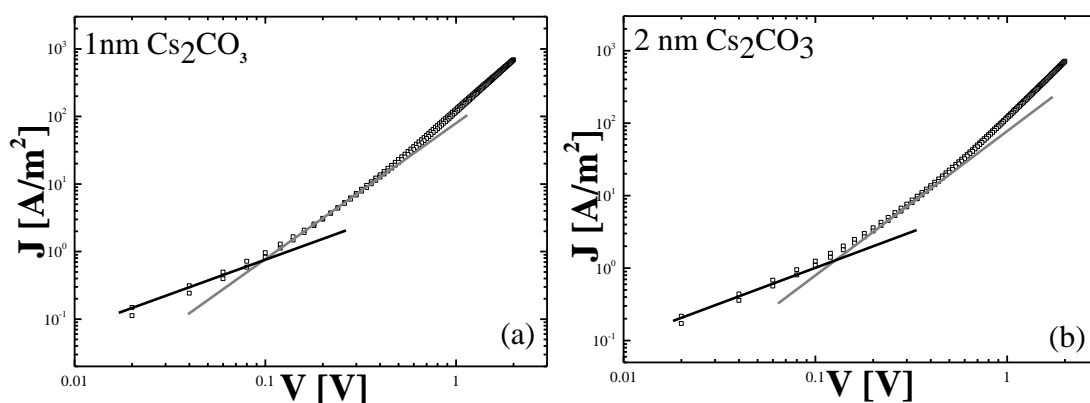


Figure 6.3. Current-voltage characteristics of commercial N2200 electron-only devices with a thickness of 215 nm with 1 nm (a) and 2 nm (b)  $\text{Cs}_2\text{CO}_3$  interlayer on a double logarithmic scale. Solid lines indicate the linear (black) and quadratic (grey) regime.

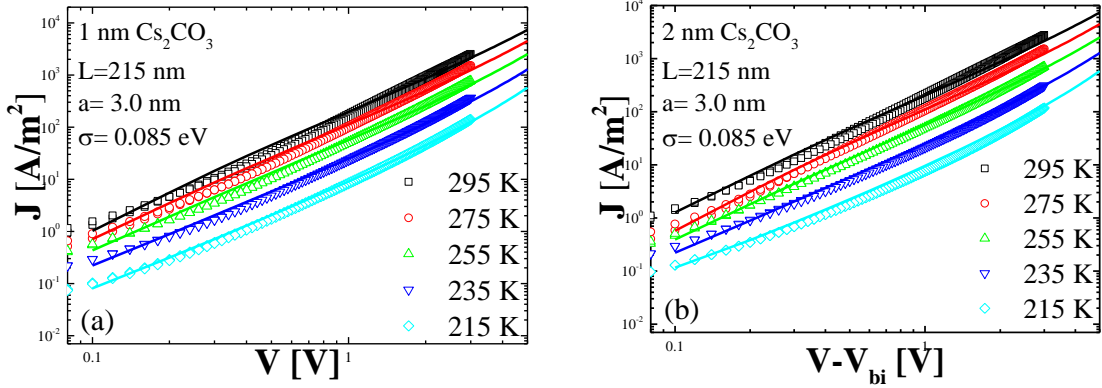


Figure 6.4. Temperature dependence of the electron current of commercial N2200 electron-only devices with a thickness of 215 nm using 1nm (a) or 2 nm  $\text{Cs}_2\text{CO}_3$  top as interlayer for the top electrode. Solid lines are fits by a numerical drift-diffusion model to the experimental data.

### 6.3. Electron Transport in N2200 with varying molecular weight

The electron currents together with the drift-diffusion simulations for RM-167, RM-215 and RM-266 materials (lowest, middle and highest molecular weight N2200, respectively) are shown in Figure 6.5, 6.6 and 6.7, respectively. The molecular weight of the materials amounts to 40,000  $g/mol$ , 91,000  $g/mol$  and 173,000  $g/mol$  for RM-167, RM-215 and RM-266, respectively. The commercial material from Polyera lies in between the RM-215 (middle) and RM-266 (high) in terms of molecular weight. For the commercial material the fit parameters as obtained from the drift-diffusion simulations amount to  $a=3.0$  nm for the average intersite spacing, and  $\sigma=0.085$  eV for the energetic disorder. Compared to earlier reported results ( $a=2.2$  nm) the average intersite spacing is slightly higher, leading to a higher field and density dependence of the mobility [14]. These parameters now serve as a reference for the transport properties of the newly synthesized batches with different molecular weight. The fit parameters from the drift-diffusion simulations of electron currents of the three different molecular weights of N2200 are listed in Table 6.1. It is seen that all three materials exhibit a higher energetic disorder of  $\sigma=0.095$  eV, as compared to the commercial material. Besides, the intersite spacing varies between the different molecular weights, as seen in Table 6.1. For the high- $M_w$  RM-266 we find a similar value as compared to the commercial material, for the low- $M_w$  (RM-167) and middle- $M_w$  (RM-

215) a higher value is obtained. The zero-field and zero-density electron mobility at room temperature amounts to  $1.15 \times 10^{-9} \text{ m}^2/\text{Vs}$ ,  $6.13 \times 10^{-10} \text{ m}^2/\text{Vs}$  and  $1.27 \times 10^{-9} \text{ m}^2/\text{Vs}$  for RM-167, RM-215 and RM-266 respectively. We observe that the electron mobilities in RM-167, RM-215 and RM-266 materials are all lower as compared to the electron mobility in the commercial N2200 material, which amounts to  $3.78 \times 10^{-8} \text{ m}^2/\text{Vs}$ . The electron mobility of the low (RM-166) and high (RM-266) compounds are identical, whereas the mobility of the middle  $M_w$  (RM-215) is two times lower. As a result, the differences in mobility are small and there is not a systematic dependence of mobility on  $M_w$ . The higher disorder and lower electron mobilities in RM-167, RM-215 and RM-266 materials could originate from the presence of electron traps incorporated during the synthesis of the materials. It has been previously shown that typical electron traps are located at around  $\sim -3.6$  eV below vacuum level. Therefore, the trap-limited electron transport in N2200 would be surprising because of its low LUMO of  $\sim -4.0$  eV. However, it has been demonstrated in MEH-PPV that by purification deep traps, meaning deeper than the universal trap at  $\sim -3.6$  eV, could be removed, leading to less hysteresis in the electron current [17]. The trapping effects due to the presence of the universal trap at  $-3.6$  eV however, remained after purification. Such additional deep traps would show up as shallow traps in N2200 due to its deep LUMO. Furthermore, also in P3HT p-type defects could be removed upon a lithium aluminum hydride treatment [18].

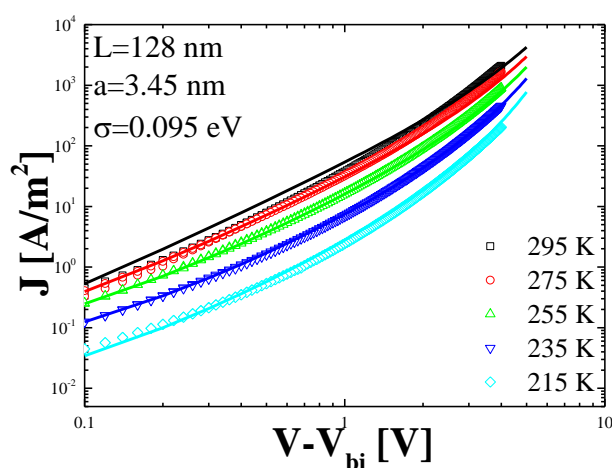


Figure 6.5. Drift-diffusion simulation of lowest molecular weight (RM-167) N2200 material.

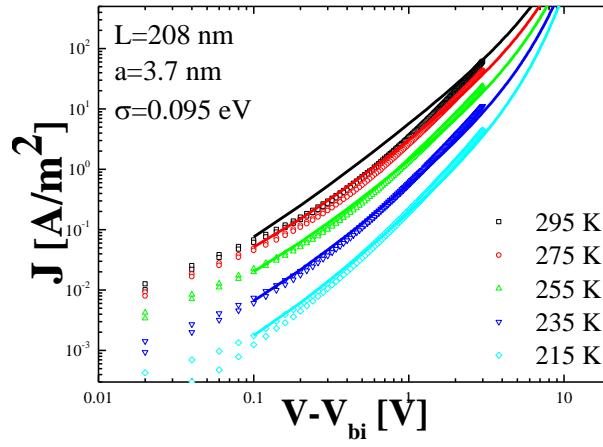


Figure 6.6. Drift-diffusion simulation of medium molecular weight (RM-215) N2200 material.

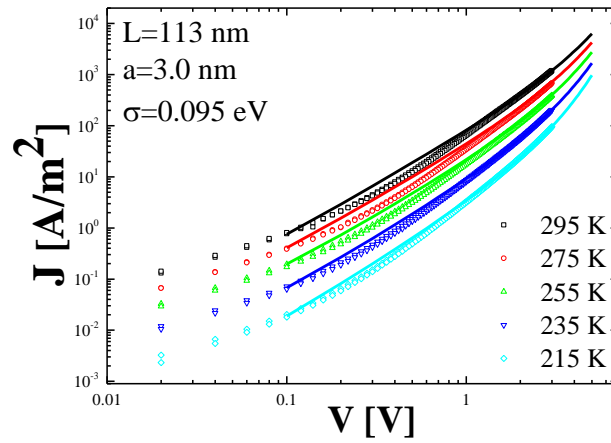


Figure 6.7. Drift-diffusion simulation of highest molecular weight (RM-266) N2200 material.

Table 6.1. The fit parameters to the drift-diffusion simulations in figure 6.1, 6.2 and 6.3.

Material	Intersite spacing ( $a$ ) [nm]	Disorder ( $\sigma$ ) [eV]	Mobility [ $\text{m}^2/\text{Vs}$ ] from E.G.D.M.[19]
RM-167	3.45	0.095	$1.15 \times 10^{-9}$
RM-215	3.70	0.095	$6.13 \times 10^{-10}$
RM-266	3.00	0.095	$1.27 \times 10^{-9}$
Commercial	2.80	0.085	$3.78 \times 10^{-8}$

#### **6.4. Conclusions**

The electron transport in the n-type conducting polymer N2200 has been studied for various molecular weights. The results have been compared to the electron transport in commercial N2200 material. Simulation of the temperature dependence of the space-charge limited electron currents show that the polymers studied here have a lower electron mobility and higher energetic disorder as compared to the commercial N2200. Furthermore, there is no systematic dependence of the mobility on molecular weight. A possible reason for the lower electron mobility and higher disorder could be the presence of shallow trapping sites that remain from the synthesis. Such traps would mask any effect of molecular weight on electron mobility.

#### **6.5. Experimental**

In this work, the electron transport in three different molecular weight N2200 polymers are studied, together with commercial N2200 as a reference. The molecular weight of the polymers amounts to 40,000 *g/mol* for the lowest  $M_w$  (RM-167), 91,000 *g/mol* for the middle  $M_w$  (RM-215) and 173,000 *g/mol* for the highest  $M_w$  (RM-266). Glass substrates covered with ITO were used and cleaned with detergent agent and ultrasonicated in acetone and isopropanol. The cleaning was finished with an UV-ozone treatment. The electron-only devices used in this study have the structure aluminum (10 nm)/N2200/cesium carbonate (1nm or 2nm)/aluminum (100 nm). The concentration of the solutions is 20 mg/ml and only for the case of the highest molecular weight material 10mg/ml concentration is used. The solutions are spin coated at 1000 rpm from toluene solution. The polydispersity of the polymers are as follows; 3.6 for the commercial N2200, 2.35 for the lowest molecular weight, 3.03 for the middle molecular weight and 4.02 for the highest molecular weight. Devices are measured under nitrogen atmosphere with a Keithley 2400 source meter.



## 6.6. References

- [1] M. M. Mandoc, F. B. Kooistra, J. C. Hummelen, B. de Boer, and P. W. M. Blom, *Appl. Phys. Lett* **91**, 263505 (2007).
- [2] C. Tanase, E. J. Meijer, P.W. M. Blom, and D. M. de Leeuw, *Phys. Rev. Lett.* **91**, 216601-1 (2003).
- [3] P. W. M. Blom, M. J. M. de Jong, and J. J. M. Vleggaar, *Appl. Phys. Lett* **68**, 3308 (1996).
- [4] H. T. Nicolai, M. Kuik, G. A. H. Wetzelaer, B. de Boer, C. Campbell, C. Risko, J. L. Brédas, and P. W. M. Blom, *Nat. Mater.* **11**, 882 (2012).
- [5] H. Yan, Z. Chen, Y. Zheng, C. Newman, J. R. Quinn, F. Dötz, M. Kastler, and A. Facchetti, *Nature* **457**, 679 (2009).
- [6] L. Gao, Z.-G. Zhang, L. Xue, J. Min, J. Zhang, Z. Wei, and Y. Li *Adv. Mater.* **28**, 1884 (2015).
- [7] R. Steyrlleuthner, M. Schubert, F. Jaiser, J. C. Blakesley, Z. Chen, A. Facchetti, and D. Neher, *Adv. Mater.* **22**, 2799 (2010).
- [8] G. Shi, J. Yuan, X. Huang, Y. Lu, Z. Liu, J. Peng, G. Ding, S. Shi, J. Sun, K. Lu, H.-Q. Wang, and W. Ma, *J. Phys. Chem. C* **119**, 25298 (2015).
- [9] D. Mori, H. Benten, I. Okada, H. Ohkita, and Shinzaburo Ito, *Energy Environ. Sci.* **7**, 2939 (2014).
- [10] S.-Y. Liu, J. W. Jung, C.-Z. Li, J. Huang, J. Zhang, H. Chen, and A. K.-Y. Jen, *J. Mater. Chem. A* **3**, 22162 (2015).
- [11] E. Pavlopoulou, C. S. Kim, S. S. Lee, Z. Chen, A. Facchetti, M. F. Toney, and Y.-L. Loo, *Chem. Mater.* **26** 5020 (2014).
- [12] N. Zhou, A. S. Dudnik, T. I. N. G. Li, E. F. Manley, T. J. Aldrich, P. Guo, H.-C. Liao, Z. Chen, L. X. Chen, R. P. H. Chang, A. Facchetti, M. O. de la Cruz, and T. J. Marks, *J. Am. Chem. Soc.* **138**, 1240 (2016).
- [13] C. Mu, P. Liu, W. Ma, K. Jiang, J. Zhao, K. Zhang, Z. Chen, Z. Wei, Y. Yi, J. Wang, S. Yang, F. Huang, A. Facchetti, H. Ade, and H. Yan, *Adv. Mater.* **26**, 7224 (2014).
- [14] G.-J. A. H. Wetzelaer, M. Kuik, Y. Olivier, V. Lemaury, J. Cornil, S. Fabiano, M. A. Loi, and P. W. M. Blom, *Phys. Rev. B* **86**, 165203-1 (2012).
- [15] Y. Tang and C. R. McNeill, *J. Polym. Sci. Part B: Polym. Phys.* **51**, 402 (2013).

*Chapter 6: Electron transport in P(NDI2OD-T2) polymer with varying molecular weights*

- [16] J. Huang, Z. Xu, and Y. Yang, *Adv. Funct. Mater.* **17**, 1966 (2007).
- [17] N. I. Craciun, Y. Zhang, A. Palmaerts, H. T. Nicolai, M. Kuik, R. J. P. Kist, G. A. H. Wetzelaer, J. Wildeman, J. Vandenberg, L. Lutsen, D. Vanderzande, and P. W. M. Blom, *J. Appl. Phys.* **107**, 124504 (2010).
- [18] Z. Liang, A. Nardes, D. Wang, J. J. Berry, and B. A. Gregg, *Chem. Mater.* **21**, 4914 (2009).
- [19] W. F. Pasveer, J. Cottaar, C. Tanase, R. Coehoorn, P. A. Bobbert, P. W. M. Blom, D. M. de Leeuw, and M. A. J. Michels, *Phys. Rev. Lett.* **94**, 206601 (2005).

## List of Publications

1. **S. Solak**, P. W. M. Blom, and G. A. H. Wetzelaer, Effect of non-ohmic contacts on the light-intensity dependence of the open-circuit voltage in organic solar cells, *Appl. Phys. Lett.* 109, 053302 (2016).
2. **S. Solak**, P. W. M. Blom, and G. A. H. Wetzelaer, Photocurrent generation in P3HT:perylene bulk heterojunction solar cells, Submitted.
3. **S. Solak**, P. W. M. Blom, and G. A. H. Wetzelaer, Loss of open-circuit voltage in annealed P3HT:perylene bulk heterojunction solar cells, Submitted.



## Curriculum Vitae

Selen Solak Sevinc

1987, Turkey

**09/2013 –10/2016**

**Ph.D.**

Max Planck Institute for Polymer Research, Mainz, Germany

**Research** : Charge Transport in Bulk Heterojunctions with Perylene Diimide based Acceptors

**08/2010 –06/2013**

**M.A.**

Bogazici University, Department of Chemical Engineering, Istanbul, Turkey

**Research** : Characterization of organic solar cells

**09/2005 –06/2009**

**B.A.**

Yildiz Technical University, Department of Chemical Engineering, Istanbul, Turkey

**09/2007 –06/2012**

**B.A. Double Major**

Yildiz Technical University, Department of Combined Arts, Art and Design Faculty, Istanbul, Turkey



## **Acknowledgments**

